

**Surface Plasmon Emission and
Dynamics in Active Planar Media**

Adam Freddie Page

Condensed Matter Theory Group
Department of Physics
Imperial College London

January 2016

Thesis submitted for the degree of
Doctor of Philosophy of Imperial College London



Declaration of Originality

The material presented in this thesis is my own work, except where otherwise referenced or acknowledged.

—A. Freddie Page, January 2016.

Copyright Declaration

The copyright of this thesis rests with the author and is made available under a Creative Commons Attribution Non-Commercial No Derivatives licence. Researchers are free to copy, distribute or transmit the thesis on the condition that they attribute it, that they do not use it for commercial purposes and that they do not alter, transform or build upon it. For any reuse or redistribution, researchers must make clear to others the licence terms of this work.

Abstract

By reducing the number of dimensions that light can propagate in from three to two, control over the properties of propagation can be achieved. The plasmonic modes of planar metal-dielectric heterostructures will confine light in one dimension, enhancing the electromagnetic fields within the structure. This thesis focuses on two particular aspects of active nanoplasmonics in planar systems, stopped light lasing and plasmons with gain in nonequilibrium graphene.

For stopped-light lasing, a plasmonic waveguide mode is designed to have two points of zero group velocity in a narrow frequency range, in order to increase the local density of optical states that a gain medium can emit into. The two stopped light points form a band of slow light that supports a wide range of wavevectors, allowing localisation over a sub-wavelength gain medium and providing the feedback required for lasing. This results in a new type of laser that does not rely on predefined cavity modes, in fact is cavity-free in 2D, dynamically forming its lasing mode about a locally pumped region of carrier inversion.

Graphene, a single-atom thick semimetal, provides the ultimate miniaturisation as a truly 2D material. It is shown that graphene can support plasmons with gain, under realistic conditions of collision loss, temperature, doping, and carrier relaxation via amplified spontaneous emission. This is made possible by developing a scheme to evaluate polarisabilities for nonequilibrium carrier distributions, allowing the calculation of the exact RPA complex-frequency plasmon dispersion solutions. The rates of spontaneous emission are calculated and are critically dependant on the exact dispersion relation. The instantaneous rates are found to be 5 times faster than previously reported and, when coupled with phonons, lead to carrier relaxations on 100 fs timescales. The polarisability and relaxation rates must form the basis of any active graphene device, where electromagnetic energy is coupled to an evolving electronic system.

Acknowledgements

I'd like to give thanks to the following people who have all, either directly or indirectly, supported me during my PhD:

Firstly, Prof. Ortwin Hess for supervising the project and giving me the opportunity to study in the group at Imperial College London; My collaborators at Imperial: Andreas Pusch, Fouad Ballout, Kosmas Tsakmakidis, Sebastian Wüstner, and Tim Pickering. Though I would like to particularly thank Joachim Hamm for mentoring me, providing endless advice and guidance, and generally being great fun to work with; Friends in and around the group not mentioned above: Anne-Julie, Doris, Fabian, James, John, Ollie, Peter, Peter, Stephanie, Seungbum, Tristan, Zara, and Zeph; House mates, first at Mayton Street: Claire, Liz, Sarah, and Karla who definitely followed *me* to Imperial. Then at Beit Hall: Andreas, Anne, Alex, Deborah, Elly, Ling, Lucia, Nathalie, Sam, Sarahs, and Savvas; Band mates in *Filthy Strings*: Amanda, Edwin, Michael, Michael, Norbert, and Sam; And to my family: Julie, Ian, Sammy, June and John, Lucinda, and Russell and Tom, for bearing with me. Finally, a special thanks goes to everyone who proof-read sections of the thesis: Andreas, Doris, Joachim, and Nathalie.

Epigraph

This little inquiry has fused.

It is now growing faster than the speed of bloody light.

It's not going to be something that we can see from space,

It's going to *be* space!

—Stewart Pearson, *The Thick of It*

Preface to the *Doctor's Edition*

Since passing my viva voce defense and submitting the “final” copy of my thesis, I have used the document as a work of reference as a research associate. As such, I’ve found cause to update certain sections, either to add short related results, in some cases to change convention uses, and indeed to correct minor mistakes spotted since submission.

The larger edits have concerned the transfer matrix method in the *Theory and Methods* section. Specifically making the eigenvalue equation more succinct, and putting transverse electric and magnetic solutions on the same footing by placing focus on in-plane electric fields.

The result is this document, which I refer to, with tongue-in-cheek, as the *Doctor's Edition*. It has not undergone further examination, and the original edition remains available online¹.

For this edition I would like to thank Nuttawut and Illya who spotted a number of the mistakes. And to give particular thanks to Prof. Anatoly Zayats and Prof. Stefan Maier for taking the time to read my thesis and conduct my viva.

¹At <https://spiral.imperial.ac.uk:8443/handle/10044/1/30760>

Contents

Front Matter	2
Declaration of Originality	2
Copyright Declaration	2
Abstract	3
Acknowledgements	4
Epigraph	4
Preface to the <i>Doctor's Edition</i>	5
Contents	6
List of Figures	10
List of Tables	11
Abbreviations, Acronyms, and Initialisms	12
List of Symbols	14
Publications	17
1. Introduction	19
2. Theory and Methods	24
2.1. Maxwell's Equations	24
2.1.1. The Macroscopic Equations	24
2.1.2. Constitutive Relations	26

Contents

2.1.3. Plane Waves	27
2.2. Material Properties	28
2.2.1. Kramers-Kronig Relations	28
2.2.2. Drude-Lorentz Model	31
2.3. Transfer Matrix Method	33
2.3.1. Transverse Electric and Transverse Magnetic Solutions	33
2.3.2. Planar Boundaries	34
2.3.3. Stratified Media	39
2.3.4. Surface Plasmon Polariton	41
2.4. Finite Difference Time Domain	43
2.5. Evolutionary Algorithm	47
3. Plasmonic Stopped Light Lasing	51
3.1. Introduction	51
3.1.1. Organisation of chapter	54
3.2. Phase Velocity, Group Velocity, and Dispersion	55
3.3. Complex Wavevector and Complex Frequency	59
3.4. Plasmonic Stopped Light Structures	61
3.4.1. Mode Hybridisation	62
3.4.2. Evolutionary Optimisation	66
3.4.3. Excitation of Stopped Light Modes	70
3.5. Frequency Domain Gain in the Small Signal Gain Regime	72
3.6. Time Domain Simulations	75
3.6.1. Four-Level System	75
3.6.2. Lasing Dynamics	78
3.6.3. Lasing Mode	81
3.7. Conclusions	90

Contents

4. Active Plasmons in Nonequilibrium Graphene	95
4.1. Introduction	95
4.1.1. Organisation of chapter	99
4.2. Plasmon Modes of Equilibrium Graphene	100
4.2.1. Complex Frequency Plasmon Dispersion	103
4.3. Nonequilibrium Polarisability	108
4.3.1. Scale-free Representation	110
4.4. Quasiequilibrium	112
4.4.1. Intrinsic Graphene	117
4.4.2. Extrinsic Graphene	118
4.5. Collision Loss and Temperature	121
4.5.1. Collision Loss	121
4.5.2. Low Temperatures	123
4.6. Hot Carriers	125
4.6.1. Fermi Distribution	127
4.6.2. Non-Fermi Distribution	130
4.7. Spontaneous Emission Spectrum	134
4.7.1. Recombination Rates at Finite Temperature and Collision Loss	140
4.8. Carrier Relaxation Dynamics	142
4.8.1. Relaxation Via the Plasmon Channel	146
4.8.2. Optical Phonons	147
4.9. Conclusions	150
5. Conclusion	153
A. Appendices	157
A.1. Plots of Functions of a Complex Variable	157

Contents

A.2. Branches of the Polarisability Function	159
References	163

List of Figures

2.1.	Kramers-Kronig contour integral	30
2.2.	Schematic of the transfer matrix method	38
2.3.	Schematic of FDTD Yee cell	44
2.4.	Evolutionary algorithm flowchart	47
3.1.	Effect of moments of the dispersion relation	56
3.2.	Hybridisation of modes	63
3.3.	Evolutionary optimisation of stopped light structures	65
3.4.	Dispersion relation of a stopped light structure	69
3.5.	Perturbation of dispersion relation and loss with Lorentzian gain . .	74
3.6.	Schematic of the four-level system	76
3.7.	Schematic of the FDTD setup	78
3.8.	Lasing onset with increasing gain density	80
3.9.	Energy density and flux of lasing mode	82
3.10.	Field evolution in steady state	84
3.11.	Complex wavevector plasmons	86
3.12.	Power spectrum of lasing modes	88
4.1.	Graphene structure and tight binding model	96
4.2.	Complex frequency plasmon dispersion of equilibrium graphene . .	106
4.3.	Nonequilibrium polarisability	109
4.4.	Carrier imbalance parameter	114
4.5.	Complex frequency plasmon dispersion of photoinverted graphene .	116
4.6.	Complex frequency plasmon dispersion for varying carrier imbalance	119
4.7.	Impact of collision loss on plasmon decay rate	122
4.8.	Impact of temperature on plasmon decay rate	123

Contents

4.9.	Limitation of low-temperature polarisability approach	126
4.10.	Polarisability as a complex contour integration	129
4.11.	High temperature plasmon dispersion curves	130
4.12.	Padé approximant for a Gaussian	131
4.13.	Polarisability of a hot electron distribution	133
4.14.	Spontaneous plasmon emission and electron recombination	138
4.15.	Impact of temperature and collisions on spontaneous emission . . .	140
4.16.	Relaxation dynamics of coupled plasmon and carrier system	145
4.17.	Relaxation dynamics of carriers coupled plasmons and phonons . .	148
A.1.	Riemann sphere and complex plots	158

List of Tables

3.1.	Simulation parameters	92
3.2.	Properties of optimised SL structure	93

Abbreviations, Acronyms, and Initialisms

Abbr.	Abbreviation	First use
2D	Two dimensional	Sec. 1
III-V	Groups three and five (semiconductor)	Sec. 3.4
AR	Auger recombination	Sec. 4.1
ASE	Amplified spontaneous emission	Sec. 3.6.1
CFPD	Complex frequency plasmon dispersion	Sec. 3.6.1
CF	Complex frequency	Sec. 3.3
CPLM	Convolutional perfectly matched layer	Sec. 3.6.2
CWV	Complex wavevector	Sec. 3.3
EA	Evolutionary algorithm	Sec. 2.5
FDTD	Finite difference time domain	Sec. 2.4
FFT	Fast Fourier transform	Sec. 3.6.3
FGR	Fermi's golden rule	Sec. 4.7
ro	Γ optical (phonon)	Sec. 4.8.2
ITO	Indium Tin Oxide	Sec. 3.4
KA	K acoustic (phonon)	Sec. 4.8.2
KO	K optical (phonon)	Sec. 4.8.2
LO	Longitudinal optical (phonon)	Sec. 4.8.2
MDF	Massless Dirac fermion	Sec. 4.1
MA	Metal-air	Sec. 3.4.1
MIM	Metal-insulator-metal	Sec. 3.4.1
MIMA	Metal-insulator-metal-air	Sec. 3.4.1
NPE	Non-equilibrium plasmon emission	Sec. 4.8
RPA	Random phase approximation	Sec. 4.1
SL	Stopped light	Sec. 3.1

Abbreviations, Acronyms, and Initialisms

SPP	Surface plasmon polariton	Sec. 1
TE	Transverse electric	Sec. 2.3.1
TM	Transverse magnetic	Sec. 2.3.1
TMD	Transition metal dichalcogenide	Sec. 1
TMM	Transfer matrix method	Sec. 2.3
TO	Transverse optical (phonon)	Sec. 4.8.2
TR-ARPES	time resolved, angle resolved photo-emission spectroscopy	Sec. 4.1
ZGV	Zero group velocity	Sec. 3.4

List of Symbols

A^\pm	Forward/backward amplitude	\dot{N}	Fermion net generation rate
a	Absorption	\dot{N}^{pump}	Number density pump rate
B	Magnetic field	\dot{N}^{rel}	Number density relaxation rate
\mathcal{C}_n	Complex contour	n	Refractive index
c	Vacuum speed of light	n_β	Boson number
D	Electric displacement field	\dot{n}_β	Boson net generation rate
D_{pl}	Plasmon density of states	$\dot{n}_\beta^{\text{rel}}$	Boson relaxation rate
E	Electric field	n_β^{eq}	Boson number
e	Electron	P	Polarisation field
e	Emission	pl	Plasmon
$\hat{\mathbf{e}}_x$	Unit vector in x direction	ph	Phonon
f	Fermi function	Q	3D boson wavevector
G	Polarisability aux. function	q	2D boson wavevector
G'	Pol. derivative aux. function	q_c	High wavevector cutoff
G_{pl}	Recombination rate density	$R_{\text{pl}}^{\text{spon}}$	Plasmon emission rate
H	Magnetic H field	R_β	Carrier relaxation rate
h	Hole	r_p^0	Electrical pump rate
\hbar	Dirac's constant	$r_{\beta,\lambda}(\mathbf{q})$	Boson spectral emission rate
J	Current density	S	Poynting vector
J_s	Surface current density	$S_{\beta,\lambda}$	Energy relaxation rate
k	Fermion wavevector	T	Temperature
k_B	Boltzmann's constant	T_0	Ambient temperature
M	Magnetisation field	T_c	Carrier temperature
\mathcal{M}	Transfer matrix	t	Time
m	Carrier inversion parameter	U_e	Fermion energy density
m_c	Critical branching parameter	\dot{U}	Energy density net rate
N	Emitter density		
N_e	Fermion number density		

List of Symbols

\dot{U}_{pump}	Energy density pump rate	Δ_ω	SL frequency bandwidth
\dot{U}^{rel}	Energy density relaxation rate	ε	Permittivity
u_d	Dispersion loss	$\bar{\varepsilon}$	Average permittivity
u_g	Group loss	ε_{bg}	Background permittivity
Z^{TE}	Transfer matrix layer parameter	ε_0	Vacuum permittivity
v_b	Band velocity	ε_∞	High frequency permittivity
v_d	Dispersion velocity	ε_L	Drude-Lorentz permittivity
v_F	Fermi velocity	$\varepsilon_{\text{RPA}}(\mathbf{q}, \omega)$	RPA dielectric function
v_g	Group velocity	$\underline{\varepsilon}$	Permittivity tensor
v_p	Phase velocity	ϵ	Fermion energy
\mathbf{x}	Position vector	$\tilde{\epsilon}^M$	Fermion Matsubara frequency
Z_0	Vacuum impedance	μ	Permeability
Z	Wave impedance	μ	Chemical potential
α_0	Vacuum fine structure constant	$\bar{\mu}$	Scale energy
α_g	Graphene fine structure const.	μ_e, μ_h	Electron fermi level
$\gamma_{\beta, \lambda}^{\text{abs}}$	Plasmon absorption rate	μ_0	Vacuum permeability
γ_L	Drude-Lorentz width	$\underline{\mu}$	Permittivity tensor
$\gamma_{\beta, \lambda}^{\text{emit}}$	Plasmon stim. emit. rate	Π	Polarisability
γ_p	Drude loss	Π^e	Electron partial polarisability
γ_{pl}	Plasmon frequency imag. part	ρ	Charge density
$\gamma_{\text{pl}}^{\text{abs}}$	Plasmon absorption rate	ρ_s	Sheet charge density
$\gamma_{\text{pl}}^{\text{emit}}$	Plasmon stim emission rate	Σ^{abs}	Plasmon absorption polarisability
γ_p	Pump width	Σ^{emit}	Plasmon stim. emit. polarisability
Γ_{pl}^e	Fermion recombination rate	σ_e	Emission cross-section
Δ_N	Inversion density	σ_s	Sheet conductivity
Δ_q	Stopped light spatial bandwidth	σ_s^{inter}	Interband sheet conductivity
Δ_t	FDTD timestep	τ_{pl}	Plasmon lifetime
Δ_x	FDTD cell size	χ_e	Electric susceptibility

List of Symbols

χ_L	Drude-Lorentz susceptibility	ω_p	Drude-Lorentz plasma frequency
χ_m	Magnetic susceptibility	ω_{pl}	Plasmon frequency solution
ω	Boson frequency	ω_p	Pump frequency
ω_L	Drude-Lorentz frequency	ω_{sp}	Surface plasmon frequency

Many quantities in this list can apply to multiple species, i.e. n_β is the number of bosons. Similar quantities, n_{pl} , n_{ph} apply more specifically to plasmons and phonons. For brevity these have been omitted. The same applies to fermions, electrons, and holes, etc. Also for brevity, variants of variables such as Fourier transforms, vector norms, and scaled versions of quantities (discussed in Sec. 4.3.1), are omitted.

Publications

This thesis contains work drawn from the following publications:

- *Completely Stopped and Dispersionless Light in Plasmonic Waveguides*,
K. L. Tsakmakidis, T. W. Pickering, J. M. Hamm, **A. F. Page**, and O. Hess,
Phys. Rev. Lett., vol. 112, p. 167401, Apr. 2014.
- *Cavity-free plasmonic nanolasing enabled by dispersionless stopped light*,
T. W. Pickering, J. M. Hamm, **A. F. Page**, S. Wuestner, and O. Hess,
Nat. Commun., vol. 5, p. 4972, Sept. 2014.
- *Ultrafast dynamics of nanoplasmonic stopped-light lasing*,
S. Wuestner, T. W. Pickering, J. M. Hamm, **A. F. Page**, A. Pusch, and O. Hess,
Faraday Discuss., vol. 178, pp. 307–324, 2015.
- *Nonequilibrium plasmons with gain in graphene*,
A. F. Page, F. Ballout, O. Hess, and J. M. Hamm,
Phys. Rev. B, vol. 91, p. 75404, Feb. 2015.
- *Nonequilibrium plasmon emission drives ultrafast carrier relaxation dynamics in photoexcited graphene*,
J. M. Hamm, **A. F. Page**, J. Bravo-Abad, F. J. Garcia-Vidal, and O. Hess,
Phys. Rev. B, vol. 93, p. 41408(R), Jan. 2016.

Chapter 1.

Introduction

Control over the propagation and interactions of light at the smallest lengthscales is the subject of the field of nano-optics. Whereas semiconductor based electronics has enjoyed a miniaturisation, driven by industry, down to nanometre scales; interactions with light on this scale are weak [1]. This is because photons can not be confined to small volumes due to the diffraction limit, which sets the minimum wavelength of light to be inversely proportional to its frequency. Semiconductor bandgaps are typically in the infrared frequency range, limiting photons of this frequency to wavelengths in the high hundreds of nanometres.

Plasmonics offers a solution to this size mismatch [2, 3]. Light couples to the oscillations of surface charges on a metal-insulator interface as a *surface plasmon polariton* (SPP) mode. There are two primary features of SPPs which make them useful in nano-optics applications; SPPs break the diffraction limit, i.e. they have wavevectors larger than what is allowed for a photon of their given frequency; secondly they have large field enhancements at the material interface. The combination of shorter wavelengths and higher field densities allows for the interaction with the electronic systems of active media [4, 5], that is usually weak with photons. This allows for

applications including biosensing [6], plasmonic modulators [7], photodetectors [8], Nonlinear effects [9], and quantum optics [10, 11].

The simplest geometry in which to study SPPs is the planar stack, that is slabs of material stacked in one dimension, leaving the other two dimensions uniform, and therefore permitting planewave solutions. In this way, the dynamics of waves in 2D are determined by the composition of the structure in the perpendicular direction. Planar structures have the advantage of ease of fabrication and mechanical stability. Nanoplasmonic layered structures have been shown to have applications as perfect lenses [12, 13], behave with hyperbolic dispersion [14], and offer more exotic setups such as “analogue computing” [15].

Planar structures provide a starting point for more complicated geometries, these may be accessed by transforming the solutions using transformation optics [16, 17], or composing together multiple layered structures into nanopatterned arrays [18, 19], or devices [20].

Layers in planar structures can be taken to the limiting case of *two-dimensional* (2D) materials [21]. These are molecularly thin layers, with heights of only a few atoms. Materials in this class include graphene [22], *transition metal dichalcogenides* (TMDS) [23], and hexagonal boron nitride [24], which are the 2D equivalent of a metal, semiconductor, and insulator respectively [25]. These materials are significant as they allow structures to be built where, not only is the light itself confined on a subwavelength scale, but the materials themselves are too.

Two questions on the subject of active nanoplasmonics are considered in this thesis. The first concerns *stopped light*. By controlling the dispersion relation of light in a plasmonic waveguide such that energy is brought to rest at zero group velocity within a gain medium, can a regime of lasing be entered without a cavity storing the light in a resonant mode?

Secondly; If graphene is optically pumped such that its carriers enter a state of inversion, are plasmon modes supported and can the inversion compensate for any material losses and lead to amplification of the plasmons?

Though seemingly disjoint, these questions are related by the approach one takes to answer them. In both systems plasmons are coupled to an inverted electronic system in order to induce the stimulated amplification that is to compensate for material losses. Analysis of the amplification requires the exact calculation of the plasmon dispersion relation in a complex frequency picture, which describes the losses and gains in time.

The problems differ in key areas too. For stopped light gain is provided by a single transition of a III-V semiconductor modelled as a four-level system, whereas gain in graphene is provided by a continuum of electron states within the graphene sheet itself. This means graphene is host to broadband spontaneous emission, whereas all emission in stopped light is monochromatic around the lasing frequency. Finally, Stopped light structures host surface plasmon polaritons, that retain a degree of photonic character and with the potential of outcoupling. Graphene on the other hand hosts plasmons, which are the short wavelength limit. Their character is more Coulombic than photonic, and the material response must be considered to include nonlocal effects.

The stopped light lasing question is approached by designing a structure which supports a single-frequency low-dispersion stopped light band. The band is optimised to support a broad range of wavevectors, allowing energy to be confined to narrow widths. Then by examining the frequency domain characteristics of an optimised structure, the parameters for a gain medium are selected. Time domain simulations are then conducted to examine the transition from amplified spontaneous emission to lasing, and to explain the lasing dynamics.

In order to get a handle on the dynamics of plasmons in graphene, the complex frequency plasmon dispersion relation must be solved for exactly within the random phase approximation framework. A formalism is developed for determining polarisabilities of graphene with nonequilibrium electron distributions. Plasmon dispersion relations are calculated for graphene in a state of photoinverted quasiequilibrium. The formalism is to include the effects of Drude collision loss, finite temperature and doping by impurities as each of these effects will seek to reduce the gain available. Finally a dynamic study of the carrier system relaxation, coupled to spontaneous and stimulated plasmon and phonon emission is conducted.

The thesis is in five chapters: The first, this overarching introduction, sets the scope of the two main questions in a context of active planar nanoplasmatics. Chapter 2 contains theory of classical electromagnetism in homogeneous media leading to a frequency domain analysis of waveguides. The finite difference time domain method is introduced to complement and go beyond the frequency domain analysis. Finally the evolutionary algorithm method of optimisation is introduced in the context of plasmonic waveguides. Chapters 3 and 4 are the main content chapters, each with their own introduction, literature, and conclusion, on the topics of *stopped light lasing* and *plasmons in nonequilibrium graphene* respectively. Chapter 5 concludes the thesis in a unifying context and offers an outlook.

Chapter 1. Introduction

Chapter 2.

Theory and Methods

2.1. Maxwell's Equations

At the fundamental level, all of classical electromagnetism and optics is governed by the microscopic Maxwell's equations, which relate the electric and magnetic fields, \mathbf{E} and \mathbf{B} , to charge and current density source terms, ρ and \mathbf{J} ,

$$\nabla \cdot \mathbf{E} = \rho/\varepsilon_0 \quad (2.1.a)$$

$$\nabla \cdot \mathbf{B} = 0 \quad (2.1.b)$$

$$\nabla \times \mathbf{E} = -\frac{\partial \mathbf{B}}{\partial t} \quad (2.1.c)$$

$$\nabla \times \mathbf{B} = \mu_0 \mathbf{J} + \varepsilon_0 \mu_0 \frac{\partial \mathbf{E}}{\partial t}, \quad (2.1.d)$$

where the constants ε_0 and μ_0 are the permittivity and permeability of free space respectively.

Light's interaction with matter can be brought under this description by considering a material which responds to electromagnetic fields by the redistribution of its

internal charge and current sources. These internal sources can be split off from applied external charges and currents which drive the system as [26],

$$\rho = \rho_{\text{int}} + \rho_{\text{ext}} \quad (2.2.\text{a})$$

$$\mathbf{J} = \mathbf{J}_{\text{int}} + \mathbf{J}_{\text{ext}} . \quad (2.2.\text{b})$$

The internal terms may be expressed in relation to the medium's polarisation and magnetisation responses, \mathbf{P} and \mathbf{M} , by the differential definition:

$$\rho_{\text{int}} = -\nabla \cdot \mathbf{P} \quad (2.3.\text{a})$$

$$\mathbf{J}_{\text{int}} = \nabla \times \mathbf{M} + \frac{\partial \mathbf{P}}{\partial t} . \quad (2.3.\text{b})$$

If one defines the following *auxiliary fields*, the *electric displacement field*, \mathbf{D} and *magnetic H-field*, \mathbf{H} as,

$$\mathbf{D} = \varepsilon_0 \mathbf{E} + \mathbf{P} \quad (2.4.\text{a})$$

$$\mathbf{H} = \frac{1}{\mu_0} \mathbf{B} - \mathbf{M} , \quad (2.4.\text{b})$$

then one may restate the Maxwell's Equations in *macroscopic* form,

$$\nabla \cdot \mathbf{D} = \rho_{\text{ext}} \quad (2.5.\text{a})$$

$$\nabla \cdot \mathbf{B} = 0 \quad (2.5.\text{b})$$

$$\nabla \times \mathbf{E} = -\frac{\partial \mathbf{B}}{\partial t} \quad (2.5.\text{c})$$

$$\nabla \times \mathbf{H} = \mathbf{J}_{\text{ext}} + \frac{\partial \mathbf{D}}{\partial t} . \quad (2.5.\text{d})$$

These equations become a complete description of the system only when accompanied by the corresponding *constitutive relations* for polarisation and magnetisation, which encode the system's response to external fields. In general these are non-linear functionals with the only restriction, due to causality, that they can only depend on the

fields at past times,

$$\mathbf{P}(\mathbf{x}, t) = \mathbf{P}[\mathbf{E}(\mathbf{x}', t' \leq t), \mathbf{B}(\mathbf{x}', t' \leq t)] \quad (2.6.a)$$

$$\mathbf{M}(\mathbf{x}, t) = \mathbf{M}[\mathbf{E}(\mathbf{x}', t' \leq t), \mathbf{B}(\mathbf{x}', t' \leq t)] . \quad (2.6.b)$$

2.1.2. Constitutive Relations

For the moment, let us restrict our attention to homogeneous media which can be approximated in the linear response regime and where the polarisation is only a functional of the electric field, and magnetisation of the magnetic field. It is usual to express the constitutive relations as \mathbf{D} and \mathbf{B} as functionals of \mathbf{E} and \mathbf{H} ¹,

$$\mathbf{D}(\mathbf{x}, t) = \mathbf{D}[\mathbf{E}(\mathbf{x}', t')] \quad (2.7.a)$$

$$\mathbf{B}(\mathbf{x}, t) = \mathbf{B}[\mathbf{H}(\mathbf{x}', t')] . \quad (2.7.b)$$

Then if the fields are taken into the Fourier domain, both in space and time; for the displacement field this reads,

$$\mathbf{D}(\mathbf{x}, t) = \mathbf{D} \left[\int d^3\mathbf{Q} d\omega \tilde{\mathbf{E}}(\mathbf{Q}, \omega) e^{i(\mathbf{Q} \cdot \mathbf{x}' - \omega t')} \right] \quad (2.8.a)$$

$$= \int d^3\mathbf{Q} d\omega \mathbf{D} \left[\frac{\tilde{\mathbf{E}}}{\tilde{E}}(\mathbf{Q}, \omega) e^{i(\mathbf{Q} \cdot \mathbf{x}' - \omega t')} \right] \tilde{E}(\mathbf{Q}, \omega) , \quad (2.8.b)$$

Where \mathbf{Q} is the wavevector and ω the frequency. Fourier transformed quantities are denoted here by tildes. Given the further condition that there is no scattering between terms of different frequency or wavevector, one can write,

$$\mathbf{D}(\mathbf{x}, t) = \int d^3\mathbf{Q} d\omega \underbrace{\underline{\varepsilon}(\mathbf{Q}, \omega) \varepsilon_0}_{\tilde{\mathbf{D}}(\mathbf{Q}, \omega)} \tilde{\mathbf{E}}(\mathbf{Q}, \omega) e^{i(\mathbf{Q} \cdot \mathbf{x} - \omega t)} \quad (2.9.a)$$

$$\tilde{\mathbf{D}}(\mathbf{Q}, \omega) = \underline{\varepsilon}(\mathbf{Q}, \omega) \varepsilon_0 \tilde{\mathbf{E}}(\mathbf{Q}, \omega) , \quad (2.9.b)$$

¹ Although \mathbf{B} is the fundamental gauge field, \mathbf{H} is usually what is actually measured, which is why it is the convention to express \mathbf{B} in terms of \mathbf{H} rather than the other way around [27].

where $\underline{\varepsilon}$ is the (dimensionless) permittivity tensor, which is non-local (wavevector dependent), dispersive (frequency dependent), and, in general, anisotropic (tensorial). An equivalent expression exists for the permeability for the magnetic fields,

$$\tilde{\mathbf{B}}(\mathbf{Q}, \omega) = \underline{\mu}(\mathbf{Q}, \omega)\mu_0 \tilde{\mathbf{H}}(\mathbf{Q}, \omega) . \quad (2.9.c)$$

2.1.3. Plane Waves

Having assumed planewaves as the eigenmodes of such a system, which is equivalent to accepting the arguments leading to Eq. 2.9.b, one may seek to work out the propagation characteristics of such waves. For this one writes the Fourier Transforms of Eqs. 2.5.c and 2.5.d assuming no external sources and incorporates the constitutive relations,

$$\mathbf{Q} \times \tilde{\mathbf{E}} = \omega \underline{\mu} \mu_0 \tilde{\mathbf{H}} \quad (2.10.a)$$

$$\mathbf{Q} \times \tilde{\mathbf{H}} = -\omega \underline{\varepsilon} \varepsilon_0 \tilde{\mathbf{E}} , \quad (2.10.b)$$

where for clarity, frequency and wavevector arguments are suppressed. Considering first the isotropic case, where the permittivity becomes scalar ($\underline{\varepsilon}\mathbf{E} = \varepsilon\mathbf{E}$ and $\underline{\mu}\mathbf{H} = \mu\mathbf{H}$), one can make the rearrangement,

$$\mathbf{Q}(\mathbf{Q} \cdot \tilde{\mathbf{E}}) - Q^2 \tilde{\mathbf{E}} = -\omega^2 \varepsilon \mu \varepsilon_0 \mu_0 \tilde{\mathbf{E}} \quad (2.11.a)$$

$$\mathbf{Q}(\mathbf{Q} \cdot \tilde{\mathbf{H}}) - Q^2 \tilde{\mathbf{H}} = -\omega^2 \varepsilon \mu \varepsilon_0 \mu_0 \tilde{\mathbf{H}} . \quad (2.11.b)$$

Two distinct types of solution are permitted, the longitudinal modes, which exist for either $\varepsilon = 0$ or $\mu = 0$, where $\mathbf{Q} \times \tilde{\mathbf{E}} = \mathbf{Q} \times \tilde{\mathbf{H}} = 0$. Or by inserting the Fourier Transform of the divergence Maxwell equations Eqs. 2.5.a and 2.5.b,

$$\mathbf{Q} \cdot \underline{\varepsilon} \tilde{\mathbf{E}} = 0 \quad (2.12.a)$$

$$\mathbf{Q} \cdot \underline{\mu} \tilde{\mathbf{H}} = 0 , \quad (2.12.b)$$

the transverse mode, where $\mathbf{Q} \cdot \tilde{\mathbf{E}} = \mathbf{Q} \cdot \tilde{\mathbf{H}} = 0$,

$$\varepsilon\mu \frac{\omega^2}{c^2} - Q^2 = 0 \quad (2.13.a)$$

$$\tilde{E} = \sqrt{\frac{\mu}{\varepsilon}} Z_0 \tilde{H}, \quad (2.13.b)$$

where the wave parameters $c = (\varepsilon_0\mu_0)^{-1/2}$ and $Z_0 = (\mu_0/\varepsilon_0)^{1/2}$ are the vacuum speed of light and vacuum impedance respectively. For completeness, the dimensionless terms $n = (\varepsilon\mu)^{1/2}$ and $Z = (\mu/\varepsilon)^{1/2}$ are referred to as the refractive index and wave impedance. Eq. 2.13.a is referred to as the dispersion relation, and describes transverse plane waves that travel with a phase velocity $v_p = n(\mathbf{Q}, \omega)c$.

2.2. Material Properties

2.2.1. Kramers-Kronig Relations

Causality dictates that the material response fields \mathbf{P} and \mathbf{M} can only depend on values of the driving fields \mathbf{E} and \mathbf{H} , at previous times. This can be encoded in the frequency domain description discussed in Sec. 2.1.2, and gives a strict relationship between the refractive and dissipative part of the material response.

To start one introduces the susceptibilities χ_e and χ_m ,

$$\tilde{\mathbf{P}}(\omega) = \varepsilon_0 \chi_e(\omega) \tilde{\mathbf{E}}(\omega) \quad (2.14.a)$$

$$\tilde{\mathbf{M}}(\omega) = \mu_0 \chi_m(\omega) \tilde{\mathbf{H}}(\omega), \quad (2.14.b)$$

which relates to the auxiliary field definitions of Eqs. 2.4 and 2.9 as,

$$\underline{\varepsilon} = 1 + \chi_e \quad (2.15.a)$$

$$\underline{\mu} = 1 + \chi_m, \quad (2.15.b)$$

where again, in general, the susceptibilities are tensors. In time domain, the response field is given as the convolution of the driving field with the susceptibility kernel,

$$\mathbf{P}(t) = \frac{\varepsilon_0}{2\pi} [\chi_e(t) \otimes \mathbf{E}(t)] = \frac{\varepsilon_0}{2\pi} \int_{-\infty}^{\infty} dt' \chi_e(t-t') \mathbf{E}(t') . \quad (2.16)$$

By inspection, one may infer that for $\mathbf{P}(t)$ to be independent of values of $\mathbf{E}(t')$ for times $t' > t$ then $\chi_e(t-t')$ must be zero for $t-t' < 0$. This is equivalent to the condition,

$$\chi_e(t) = \chi_e(t)\theta(t) , \quad (2.17)$$

where $\theta(t)$ is the Heaviside step function. In frequency domain this is represented as a convolution,

$$\chi_e(\omega) = \chi_e(\omega) \otimes \mathcal{F}[\theta(t)] \quad (2.18.a)$$

$$= \chi_e(\omega) \otimes \left[\mathcal{P} \frac{i}{2\pi\omega} + \frac{\delta(\omega)}{2} \right] . \quad (2.18.b)$$

This means that causal susceptibilities are eigenfunctions of the *Hilbert Transform* with eigenvalue i :

$$i\chi_e(\omega) = \frac{1}{\pi} \mathcal{P} \int_{-\infty}^{\infty} d\omega' \frac{\chi_e(\omega')}{\omega' - \omega} . \quad (2.19)$$

By taking real and imaginary parts, the *Kramers-Kronig Relations* are derived,

$$\text{Re } \chi_e(\omega) = \frac{1}{\pi} \mathcal{P} \int_{-\infty}^{\infty} d\omega' \frac{\text{Im } \chi_e(\omega')}{\omega' - \omega} \quad (2.20.a)$$

$$\text{Im } \chi_e(\omega) = \frac{1}{\pi} \mathcal{P} \int_{-\infty}^{\infty} d\omega' \frac{-\text{Re } \chi_e(\omega')}{\omega' - \omega} . \quad (2.20.b)$$

Knowing one part, either the real or imaginary, of the susceptibility (and hence permittivity) will uniquely define the other. The real part determines the wave dispersion, whereas the imaginary part is the loss, i.e. by how much the system oscillates out of phase with the driving term leading to energy dissipation. This result proves that for a material with any dispersion, there is necessarily loss (or gain) accompanying it.

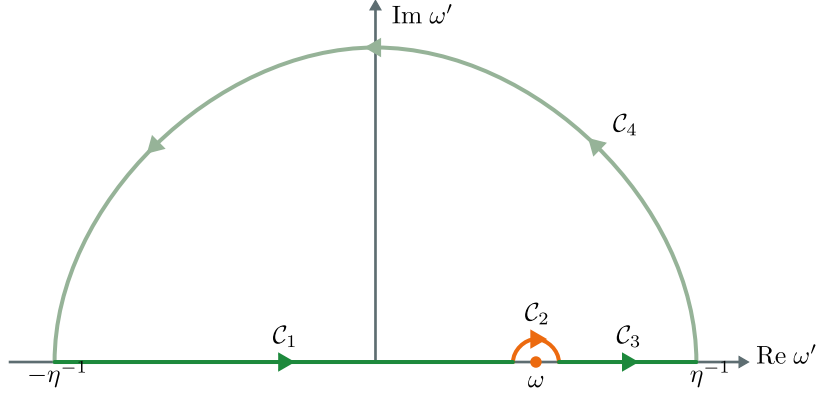


Figure 2.1: Kramers-Kronig contour integral.

The contour integral of Eq. 2.21 can be split into three parts, $\mathcal{C}_1 \cup \mathcal{C}_3$ (deep green) is the principal value of the integral along the real line; \mathcal{C}_2 (orange) is half the integral around a pole at ω ; and \mathcal{C}_4 (pale green) is a contribution that vanishes as the contour limits to infinity.

A more subtle result that can be derived from the Kramers-Kronig relations is, that as a function of a complex ω , $\chi_e(\omega)$ is analytic in the upper half-plane. Take the following contour integral,

$$\oint_{\mathcal{C}} d\omega' \frac{\chi_e(\omega')}{\omega' - \omega} , \quad (2.21)$$

over the closed contour \mathcal{C} , where \mathcal{C} is the infinite semicircle that encloses the upper half-plane, with a infinitesimal semicircular dent taken out to avoid the pole at $\omega' = \omega$, as shown in Fig. 2.1, i.e. $\mathcal{C} = \bigcup_{i=1}^4 \mathcal{C}_i$ with,

$$\mathcal{C}_1 = [-\eta^{-1}, \omega - \eta] \quad (2.22.a)$$

$$\mathcal{C}_2 = \{\omega - \eta e^{-i\theta} \mid \theta \in [0, \pi]\} \quad (2.22.b)$$

$$\mathcal{C}_3 = [\omega + \eta, \eta^{-1}] \quad (2.22.c)$$

$$\mathcal{C}_4 = \{\eta^{-1} e^{i\theta} \mid \theta \in [0, \pi]\} , \quad (2.22.d)$$

in the limit as $\eta \rightarrow 0$.

So long as $\chi_e(\omega)$ is analytic in the upper half-plane, that is to say there are no

singularities in that region, then Eq. 2.21 will evaluate to zero. That is to say,

$$\int_{C_1} + \int_{C_2} + \int_{C_3} + \int_{C_4} d\omega' \frac{\chi_e(\omega')}{\omega' - \omega} = 0 . \quad (2.23)$$

Contributions from contours 1 and 3 combine to form the principal value of the integral. Contour 2 is equal to minus half the residue about the pole Contour 4 vanishes to zero, which can be understood physically as the response of a material is unable to match an arbitrarily fast driving term. This allows the rearrangement of Eq. 2.23 as,

$$\mathcal{P} \int_{-\infty}^{\infty} d\omega' \frac{\chi_e(\omega')}{\omega' - \omega} = \frac{1}{2} 2\pi i \operatorname{Res} \left(\frac{\chi_e(\omega')}{\omega' - \omega}, \omega \right) . \quad (2.24)$$

which then exactly reproduces Eq. 2.19.

This guarantees that the upper half-plane of a causal response function is analytic, and therefore free of singularities.

2.2.2. Drude-Lorentz Model

One of the most important material models that one can consider is the Drude-Lorentz model. It is a causal [28] response that captures the behaviour of most resonance phenomena. In its most general terms, it relates the time evolution of \mathbf{P} to a driving \mathbf{E} field by a second order differential equation:

$$\frac{\partial^2 \mathbf{P}}{\partial t^2} + \gamma_L \frac{\partial \mathbf{P}}{\partial t} + \omega_L^2 \mathbf{P} = \omega_p^2 \varepsilon_0 \mathbf{E} , \quad (2.25)$$

where γ_L is a damping term, ω_L is the restoring force frequency, and ω_p is the plasma frequency - the coupling strength to the driving \mathbf{E} field. In frequency domain, one gets,

$$\tilde{\mathbf{P}} = \varepsilon_0 \frac{\omega_p^2}{\omega_L^2 - \omega(\omega + i\gamma_L)} \tilde{\mathbf{E}} , \quad (2.26)$$

where the Drude-Lorentz susceptibility can be extracted,

$$\chi_L(\omega) = \frac{\omega_p^2}{\omega_L^2 - \omega(\omega + i\gamma_L)} . \quad (2.27)$$

This is analytic in the upper halfplane for $\gamma_L > 0$, and as such obeys the Kramers-Kronig relations of the previous section.

The origins of a Drude-Lorentz model may vary, and indeed as will be shown later, a material may host multiple resonances, however, particularly for a metal, one may explain the origins with a simple model for a free electron gas. For each electron, let the displacement from its nucleus be given as $\mathbf{x}(t)$. A Newtonian force equation can be built from this, using the Lorentz force law, i.e.,

$$m^* \frac{\partial^2 \mathbf{x}}{\partial t^2} = -e\mathbf{E}, \quad (2.28)$$

where m^* is the effective mass of an electron and e is its charge. Additional forces can be included, such as a collision term proportional to the velocity and inversely to an average collision time $-\frac{\partial \mathbf{x}}{\partial t}/\tau$. In this free electron picture, there is no restoring force, though it is conceivable to add one for electrons bound to a lattice site. The macroscopic polarisation can be related to these electron displacements, as each displacement induces an electronic dipole moment, and these can be averaged to the polarisation by multiplying by the electron number density, $\mathbf{P} = -en\mathbf{x}$. A comparison of terms allows for the mapping,

$$\omega_p^2 \rightarrow \frac{ne^2}{m^*}, \quad \gamma \rightarrow \tau^{-1}, \quad \omega_L \rightarrow 0. \quad (2.29)$$

This is the Drude model, and with an additional static background permittivity ϵ_{bg} , it well describes metals.

Real materials typically have multiple resonances, which can be incorporated by adding multiple Drude-Lorentz resonances,

$$\chi = \sum_i \frac{\omega_{pi}^2}{\omega_{Li}^2 - \omega(\omega + i\gamma_{Li})}. \quad (2.30)$$

These can have a variety of origins, i.e. in addition to the plasma mode discussed, rotational modes, electronic transitions, etc.; and indeed the magnetic response, χ_m , can also be described as a sum of Drude-Lorentz resonances.

2.3. Transfer Matrix Method

2.3.1. Transverse Electric and Transverse Magnetic Solutions

The transverse solutions of Sec. 2.1.3 can be generalised to anisotropic media. Equations 2.10 can be re-written as matrix equations,

$$\tilde{\mathbf{E}} = \underline{\mathbf{Z}} Z_0 \tilde{\mathbf{H}} \quad (2.31)$$

$$Z_0 \tilde{\mathbf{H}} = \underline{\mathbf{Y}} \tilde{\mathbf{E}}, \quad (2.32)$$

where $\underline{\mathbf{Z}}$ and $\underline{\mathbf{Y}}$ are the impedance and admittance tensors, respectively, defined as,

$$\underline{\mathbf{Z}} = -\frac{c}{\omega} \underline{\boldsymbol{\varepsilon}}^{-1} [\mathbf{Q} \times] \quad (2.33)$$

$$\underline{\mathbf{Y}} = \frac{c}{\omega} \underline{\boldsymbol{\mu}}^{-1} [\mathbf{Q} \times], \quad (2.34)$$

with $[\mathbf{Q} \times]$ defined as the cross product with \mathbf{Q} expressed as a matrix. This allows the electric and magnetic fields to be written as an eigenvalue equation,

$$\tilde{\mathbf{E}} = \underline{\mathbf{Z}} \underline{\mathbf{Y}} \tilde{\mathbf{E}} \quad (2.35)$$

$$Z_0 \tilde{\mathbf{H}} = \underline{\mathbf{Y}} \underline{\mathbf{Z}} Z_0 \tilde{\mathbf{H}}. \quad (2.36)$$

The matrix $\underline{\mathbf{ZY}}$ (and $\underline{\mathbf{YZ}}$) has one zero eigenvalue, and by solving for the other two to be equal to one will give the dispersion relation for two independent planewave solutions. The eigenvectors will determine the field polarisation for each solution.

Consider a medium with non-singular permittivity and permeability that are simultaneously diagonalisable, i.e., $\underline{\boldsymbol{\varepsilon}} = \text{Diag}(\varepsilon_x, \varepsilon_y, \varepsilon_z)$ and $\underline{\boldsymbol{\mu}} = \text{Diag}(\mu_x, \mu_y, \mu_z)$ in this coordinate system. Further assume that the wave propagates in a plane normal to the y -direction, i.e. $\mathbf{Q} = (q, 0, \kappa)^T$. The resulting two solutions become the basis

for *transverse electric* (TE) modes,

$$\mu_x \mu_z \varepsilon_y \frac{\omega^2}{c^2} - \mu_x q^2 - \mu_z \kappa^2 = 0 \quad (2.37.a)$$

$$\tilde{\mathbf{E}} = \tilde{E} (0, 1, 0)^T \quad (2.37.b)$$

$$Z_0 \tilde{\mathbf{H}} = \tilde{E} \left(-\frac{c\kappa}{\mu_x \omega}, 0, \frac{cq}{\mu_z \omega} \right)^T, \quad (2.37.c)$$

and *transverse magnetic* (TM) modes that will be discussed later in this section,

$$\varepsilon_x \varepsilon_z \mu_y \frac{\omega^2}{c^2} - \varepsilon_x q^2 - \varepsilon_z \kappa^2 = 0 \quad (2.38.a)$$

$$\tilde{\mathbf{E}} = \tilde{E} \left(1, 0, -\frac{\varepsilon_x q}{\varepsilon_z \kappa} \right)^T \quad (2.38.b)$$

$$Z_0 \tilde{\mathbf{H}} = \tilde{E} \left(0, \frac{\varepsilon_x \omega}{c \kappa}, 0 \right)^T, \quad (2.38.c)$$

2.3.2. Planar Boundaries

Until now we have considered electromagnetic fields in a homogeneous space, however there is a lot of interesting physics to be found at the boundaries between different media, and indeed the majority of this thesis considers surface phenomena.

Consider two infinite half-spaces divided by a planar boundary at $z = 0$. Let each half-space be filled with a medium, characterised by permittivity and permeability $\underline{\varepsilon}$ and $\underline{\mu}$ as described above. The solutions in each half-space can be assumed to be the same as those in the homogeneous case for each medium, i.e. planewaves.²

It then becomes a question to derive the *boundary equations* which knit together the solutions at the boundary of the spaces. To start one takes the Macroscopic Maxwell's Equations, Eq. 2.5, and applies Gauss' and Stokes' theorems, to yield their integral

² Strictly, this is only true if the media are local in the direction normal to the interface.

form,

$$\oint_{\partial V} \mathbf{D} \cdot d\mathbf{S} = \iiint_V \rho_{\text{ext}} dV \quad (2.39.a)$$

$$\oint_{\partial V} \mathbf{B} \cdot d\mathbf{S} = 0 \quad (2.39.b)$$

$$\oint_{\partial\sigma} \mathbf{E} \cdot d\mathbf{l} = -\frac{\partial}{\partial t} \iint_{\sigma} \mathbf{B} \cdot d\boldsymbol{\sigma} \quad (2.39.c)$$

$$\oint_{\partial\sigma} \mathbf{H} \cdot d\mathbf{l} = \iint_{\sigma} \mathbf{J}_{\text{ext}} \cdot d\boldsymbol{\sigma} + \frac{\partial}{\partial t} \iint_{\sigma} \mathbf{D} \cdot d\boldsymbol{\sigma}, \quad (2.39.d)$$

Allowing for the possibility of surface charges and currents, $\rho_{\text{ext}} = \rho_s \delta(z)$ and $\mathbf{J}_{\text{ext}} = \mathbf{J}_s \delta(z)$, and taking the volume of integration, V , to be a cube of arbitrary x,y dimension, but infinitesimally thin in z and straddling the boundary plane, then,

$$(\mathbf{D}_2 - \mathbf{D}_1) \cdot \hat{\mathbf{e}}_z = \rho_s \quad (2.40.a)$$

$$(\mathbf{B}_2 - \mathbf{B}_1) \cdot \hat{\mathbf{e}}_z = 0. \quad (2.40.b)$$

The surface of integration, σ , is a plane parallel to z and either x or y , again infinitesimal in z , this gives the further relations,

$$\hat{\mathbf{e}}_z \times (\mathbf{E}_2 - \mathbf{E}_1) = 0 \quad (2.40.c)$$

$$\hat{\mathbf{e}}_z \times (\mathbf{H}_2 - \mathbf{H}_1) = \mathbf{J}_s. \quad (2.40.d)$$

Where subscripts 1 and 2 refer to the values of the fields just below and just above of the interface.

For the planewaves to maintain continuity between each half-space, they must be of the same frequency, and have the same component of wavevector parallel to the surface. Considering the space-time domain solution of a single frequency component, this restricts the value of the perpendicular component of the wavevector to be determined by Eqs. 2.37.a and 2.38.a, for which there are two solutions, since they are

equations in κ^2 . The solution in each space is given as,

$$\mathbf{E} = \begin{cases} \mathbf{E}_1^+ e^{i(qx + \kappa_1 z - \omega t)} + \mathbf{E}_1^- e^{i(qx - \kappa_1 z - \omega t)} + \text{c.c.} & : z < 0 \\ \mathbf{E}_2^+ e^{i(qx + \kappa_2 z - \omega t)} + \mathbf{E}_2^- e^{i(qx - \kappa_2 z - \omega t)} + \text{c.c.} & : z > 0 \end{cases}, \quad (2.41)$$

with equivalent solutions for \mathbf{H} , \mathbf{B} , and \mathbf{D} . The surface charges and currents can be included with the additional constitutive relation, defining the surface conductivity σ_s ,

$$\mathbf{J}_s = \sigma_s(\mathbf{q}, \omega) \mathbf{E}^{\parallel}(z=0) \quad (2.42.a)$$

$$\rho_s = \sigma_s(\mathbf{q}, \omega) \mathbf{q} \cdot \mathbf{E}^{\parallel}(z=0)/\omega, \quad (2.42.b)$$

where the parallel symbol on \mathbf{E}^{\parallel} indicates the z component of that vector is set to zero, and \mathbf{q} is the x, y plane projection of \mathbf{Q} .

To proceed, one needs to consider the TE and TM solutions in turn and apply the boundary value conditions for $z = 0$.

For the TE solution, the non-zero \mathbf{E} and \mathbf{H} field components are E_y , H_x , and H_z . This though is overdetermined, with $Z_0 H_z = qc/(\omega \mu_z) E_y$. The boundary value problem can be expressed as a matrix³,

$$\begin{pmatrix} E_{y2} \\ -Z_0 H_{x2} \end{pmatrix} = \underbrace{\begin{pmatrix} 1 & 0 \\ -Z_0 \sigma_s & 1 \end{pmatrix}}_{\mathbf{S}^{\text{TE}}} \begin{pmatrix} E_{y1} \\ -Z_0 H_{x1} \end{pmatrix}, \quad (2.43.a)$$

where it can be verified that this also continues the auxiliary fields in the correct manner. One may determine the coefficients of the forward and backward propagating waves in Eq. 2.41 by expressing it in matrix form for $\mathbf{x} = 0, t = 0$,

$$\begin{pmatrix} E_{yi} \\ -Z_0 H_{xi} \end{pmatrix} = \underbrace{\begin{pmatrix} 1 & 1 \\ 1/Z_i^{\text{TE}} & -1/Z_i^{\text{TE}} \end{pmatrix}}_{\mathbf{U}^{\text{TE}}} \begin{pmatrix} A_i^+ \\ A_i^- \end{pmatrix}, \quad (2.43.b)$$

³ In order to keep E_y , H_x , and z as a right handed triplet (and for symmetry with the TM matrices) the matrix is expressed for (a negative) $-H_x$.

with $Z_i^{\text{TE}} = \mu_{xi}\omega/(c\kappa_i)$, is the angle dependent⁴ impedance, and $A_i^\pm = \mathbf{E}_i^\pm \cdot \hat{\mathbf{e}}_y$.

The fields can then be calculated at any z coordinate by propagating the forward and backward components,

$$\begin{pmatrix} A_i^+ \\ A_i^- \end{pmatrix} \Bigg|_z = \underbrace{\begin{pmatrix} e^{i\kappa_i(z-z')} & 0 \\ 0 & e^{-i\kappa_i(z-z')} \end{pmatrix}}_{\mathbf{T}} \begin{pmatrix} A_i^+ \\ A_i^- \end{pmatrix} \Bigg|_{z'}, \quad (2.43.c)$$

and of course, at any x and t by multiplication of $e^{i(qx-\omega t)}$.

The equivalent TM transfer matrices are given as,

$$\begin{pmatrix} E_{x2} \\ Z_0 H_{y2} \end{pmatrix} = \underbrace{\begin{pmatrix} 1 & 0 \\ -Z_0 \sigma_s & 1 \end{pmatrix}}_{\mathbf{S}^{\text{TM}}} \begin{pmatrix} E_{x1} \\ Z_0 H_{y1} \end{pmatrix} \quad (2.44.a)$$

$$\begin{pmatrix} E_{xi} \\ Z_0 H_{yi} \end{pmatrix} = \underbrace{\begin{pmatrix} 1 & 1 \\ 1/Z_i^{\text{TM}} & -1/Z_i^{\text{TM}} \end{pmatrix}}_{\mathbf{U}^{\text{TM}}} \begin{pmatrix} A_i^+ \\ A_i^- \end{pmatrix} \quad (2.44.b)$$

$$\begin{pmatrix} A_i^+ \\ A_i^- \end{pmatrix} \Bigg|_z = \underbrace{\begin{pmatrix} e^{i\kappa_i(z-z')} & 0 \\ 0 & e^{-i\kappa_i(z-z')} \end{pmatrix}}_{\mathbf{T}} \begin{pmatrix} A_i^+ \\ A_i^- \end{pmatrix} \Bigg|_{z'}, \quad (2.44.c)$$

with $Z_i^{\text{TM}} = c\kappa_i/(\varepsilon_{xi}\omega)$. These are the matrices of the *transfer matrix method* (TMM). The matrices, \mathbf{S} , \mathbf{U} , and \mathbf{T} , in both the TE and TM case, are assigned respectively such that \mathbf{S} continues electric and magnetic fields from one medium over an interface into another; \mathbf{U} converts from the basis of forward and backward travelling waves to electric and magnetic field components; and \mathbf{T} propagates forward and backward travelling waves from a point z' to a point z .

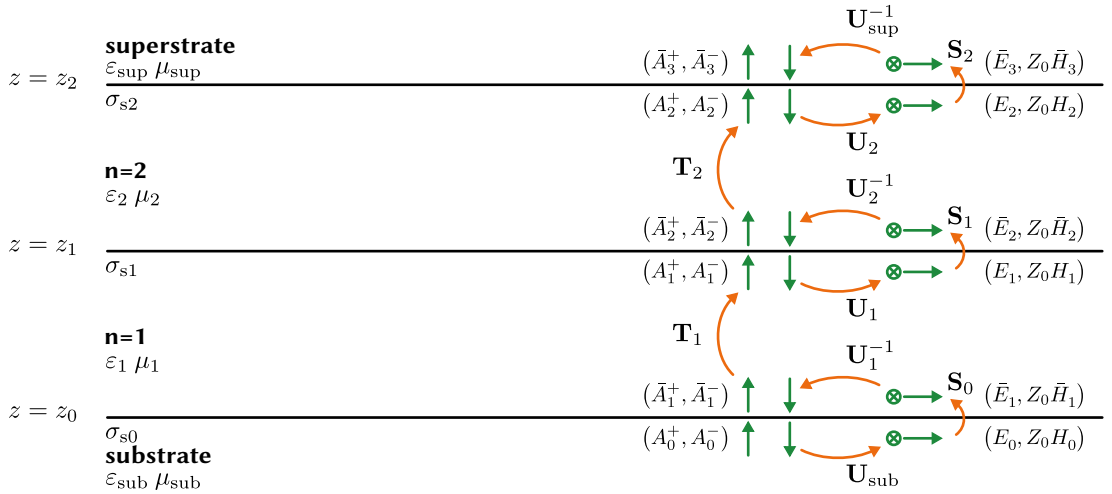


Figure 2.2: Schematic of the transfer matrix method.

Fields (green arrows) are operated on by matrix transformations (orange arrows). The forward and backward components at the top of substrate layer (A_0^+, A_0^-) are transferred through the stack to forward and backward components at the bottom of the superstrate layer (\bar{A}_3^+, \bar{A}_3^-). Fields move between bases of forward and backward waves ($\uparrow \downarrow$) and electric and magnetic components ($\otimes \rightarrow$).

2.3.3. Stratified Media

Up until now, this matrix description can be at best described as book-keeping. Its utility will become clear when generalising to stratified media. Consider a stack of N planar slabs on a substrate as in Fig. 2.2, each with its own material properties. Let the top interface of the i^{th} slab be at z_i , vector components with that label, e.g. A_i^\pm , be measured from there, i.e. just below the top interface in that layer. Starting in the forward and backward basis, one may use the transfer matrices to propagate through the stack from the one layer to the next.

$$\begin{pmatrix} A_{i+1}^+ \\ A_{i+1}^- \end{pmatrix} = \mathbf{T}_{i+1} \mathbf{U}_{i+1}^{-1} \mathbf{S}_i \mathbf{U}_i \begin{pmatrix} A_i^+ \\ A_i^- \end{pmatrix}. \quad (2.45)$$

The exception to this being the superstrate, the $(N + 1)^{\text{th}}$ layer, which by definition does not have a top interface. As such E_{sup}^\pm is defined specially as the forward and backward components just above the top interface of the N^{th} layer, i.e.,

$$\begin{pmatrix} A_{\text{sup}}^+ \\ A_{\text{sup}}^- \end{pmatrix} = \mathbf{U}_{\text{sup}}^{-1} \mathbf{S}_N \mathbf{U}_N \begin{pmatrix} A_N^+ \\ A_N^- \end{pmatrix}. \quad (2.46)$$

The full transfer matrix \mathcal{M} is given as the product of each layer hop,

$$\mathcal{M} = \mathbf{U}_{\text{sup}}^{-1} \mathbf{S}_N \mathbf{U}_N \cdots \mathbf{T}_1 \mathbf{U}_1^{-1} \mathbf{S}_0 \mathbf{U}_{\text{sub}}. \quad (2.47)$$

Terms with similar indices can be grouped to give a matrix for each layer ⁵,

$$\mathbf{M}_i = \mathbf{U}_i \mathbf{T}_i \mathbf{U}_i^{-1}, \quad (2.48)$$

such that the transfer matrix for the whole stack is,

$$\mathcal{M} = \mathbf{U}_{\text{sup}}^{-1} \left(\prod_{i=N}^1 \mathbf{S}_i \mathbf{M}_i \right) \mathbf{S}_0 \mathbf{U}_{\text{sub}}, \quad (2.49)$$

⁴ For normal incidence, $q = 0$, the impedances take the more familiar form, $Z^{\text{TE}} = \sqrt{\mu_x/\varepsilon_y}$ and

$$Z^{\text{TM}} = \sqrt{\mu_y/\varepsilon_x}.$$

⁵ Thin film (non-magnetic) layers with thickness $\delta \rightarrow 0$ can be approximated as $\mathbf{M} \approx \mathbf{S}$, with

$$Z_0 \sigma_s \rightarrow -i\delta(\omega/c)\varepsilon_x \text{ for TM and } Z_0 \sigma_s \rightarrow -i\delta(\omega/c)\varepsilon_y \text{ for TE solutions.}$$

noting the reverse order on the product.

The matrix \mathcal{M} maps forward and backward travelling waves in the substrate to forward and backward waves in the superstrate. This can be used to calculate reflection and transmission spectra. Assume a plane wave incident in the superstrate, this will both reflect at the surface and transmit into the substrate. This can be codified as a matrix equation, with the assumption that there is no incoming wave from the substrate,

$$\begin{pmatrix} r \\ 1 \end{pmatrix} = \mathcal{M} \begin{pmatrix} 0 \\ t \end{pmatrix}, \quad (2.50)$$

where $1, r, t$ are the coefficients of the incoming, reflected, and transmitted components, respectively, of the E field parallel to the stack. This is solved as,

$$t = (\mathcal{M}_{22})^{-1} \quad (2.51.a)$$

$$r = (\mathcal{M}_{12}) / (\mathcal{M}_{22}). \quad (2.51.b)$$

The coefficients r and t can be used to determine the power flows by the introduction of the Poynting vector,

$$\mathbf{S}(\mathbf{x}, t) = \mathbf{E}(\mathbf{x}, t) \times \mathbf{H}(\mathbf{x}, t), \quad (2.52)$$

which is the flux vector of electromagnetic power [27]. Because it is the product of fields, it is strictly speaking defined only in space-time domain, however for quasi-monochromatic fields the time-averaged Poynting vector can be defined as:

$$\langle \mathbf{S} \rangle = \frac{1}{2} \operatorname{Re} (\mathbf{E} \times \mathbf{H}^*). \quad (2.53)$$

The component normal to the stacking is of most interest, and in both the TM and TE case, this can be calculated in each layer as,

$$\langle \mathbf{S} \rangle_z = \operatorname{Re} \frac{1}{2Z_i Z_0} (|A_i^+|^2 - |A_i^-|^2) + \operatorname{Im} \frac{1}{Z_i Z_0} \operatorname{Im} (A_i^{+*} A_i^-). \quad (2.54)$$

The first term is power transferred in propagating fields, while the last term describes power in evanescent fields.

For propagating waves incident in a lossless upper half-plane, the ratio of reflected and transmitted power flows to the incident power is calculated as,

$$R = \operatorname{Re} \frac{1}{2Z_{\text{sup}}Z_0} |A_{\text{sup}}^+|^2 / \operatorname{Re} \frac{1}{2Z_{\text{sup}}Z_0} |A_{\text{sup}}^-|^2 \quad (2.55.\text{a})$$

$$T = \operatorname{Re} \frac{1}{2Z_{\text{sub}}Z_0} |A_{\text{sub}}^-|^2 / \operatorname{Re} \frac{1}{2Z_{\text{sup}}Z_0} |A_{\text{sup}}^-|^2 . \quad (2.55.\text{b})$$

In terms of the coefficients of Eq. 2.51.a, this reads,

$$R = |r|^2 \quad (2.56.\text{a})$$

$$T = \frac{\operatorname{Re} Z_{\text{sub}}^{-1}}{\operatorname{Re} Z_{\text{sup}}^{-1}} |t|^2 . \quad (2.56.\text{b})$$

One point has been so far glossed over: the branch of the square root of κ^2 . Both positive and negative solutions are included, but to identify one or the other as forward or backward travelling waves, one must chose κ such that $\operatorname{Re} \kappa > 0$ in the superstrate. In the substrate the situation is more complicated, since the waves may be either propagating or evanescent here. If κ is real, pick the positive root, but if it is complex or imaginary, it must be picked such that $\operatorname{Im} \kappa > 0$. This will guarantee that fields exponentially decay from the surface rather than diverging.

2.3.4. Surface Plasmon Polariton

With the transfer matrix, one is also able to calculate the bound modes of a system. These are the eigenmodes of the system which have non-zero fields for a zero driving field, i.e.,

$$\begin{pmatrix} A_{\text{sup}}^+ \\ 0 \end{pmatrix} = \mathcal{M} \begin{pmatrix} 0 \\ A_{\text{sub}}^- \end{pmatrix} , \quad (2.57)$$

with the prescription that $\operatorname{Im} \kappa > 0$ in both the super- and substrate, such that fields on both sides decay away to infinity. This yields the condition that $\mathcal{M}_{22} = 0$ for bound

modes. In general this is satisfied for either one of the frequency ω or wavevector q being a complex number, with the other remaining real.

Here the example of the surface plasmon polariton (SPP) is considered, a mode that exists on the interface between a metal and an insulator, where charge carriers on the metal's surface couples to the electric field. SPPs are of interest because, as will be shown, they permit field solutions which extend beyond the diffraction limit, allowing for high confinement of electromagnetic energy and large field enhancement at the interface.

Consider a metal substrate and dielectric superstrate, the metal characterised by a dispersive permittivity $\varepsilon(\omega)$ and the dielectric by a static constant ε_{bg} . Both layers are non-magnetic, $\mu = 1$, and there is no external surface conductivity $\sigma_s = 0$. SPP modes are TM in nature, so we shall only seek these solutions. It can be shown that TE SPP solutions do not exist [26].

In this case the transfer matrix is given as,

$$\mathcal{M} = \mathbf{U}_{\text{sup}}^{-1} \mathbf{U}_{\text{sub}} \quad (2.58.\text{a})$$

$$= \frac{1}{2} \begin{pmatrix} 1 & \frac{c\kappa_{\text{sup}}}{\varepsilon_{\text{bg}}\omega} \\ 1 & -\frac{c\kappa_{\text{sup}}}{\varepsilon_{\text{bg}}\omega} \end{pmatrix} \begin{pmatrix} 1 & 1 \\ \frac{\varepsilon(\omega)\omega}{c\kappa_{\text{sub}}} & -\frac{\varepsilon(\omega)\omega}{c\kappa_{\text{sub}}} \end{pmatrix}, \quad (2.58.\text{b})$$

which gives the SPP condition,

$$\mathcal{M}_{22} = \frac{1}{2} \left(\frac{c\kappa_{\text{sup}}}{\varepsilon_{\text{bg}}\omega} \frac{\varepsilon(\omega)\omega}{c\kappa_{\text{sub}}} + 1 \right) = 0 \quad (2.59)$$

$$\frac{\varepsilon(\omega)}{\varepsilon_{\text{bg}}} + \frac{\kappa_{\text{sub}}}{\kappa_{\text{sup}}} = 0. \quad (2.60)$$

One can see that for this equation to have solutions, given $\varepsilon_{\text{bg}} > 0$ and $\text{Im } \kappa > 0$, then it must hold that $\text{Re } \varepsilon(\omega) < 0$, which is characteristic of metals for frequencies below their plasma frequency.

For a lossless Drude metal, i.e. $\varepsilon(\omega) = \varepsilon_\infty - (\omega_p/\omega)^2$, an analytical solution exists,

$$q^2 = \varepsilon_{\text{bg}} \left(\frac{\omega}{c} \right)^2 \frac{\varepsilon_\infty \omega^2 - (\varepsilon_{\text{bg}} + \varepsilon_\infty) \omega_{\text{sp}}^2}{(\varepsilon_{\text{bg}} + \varepsilon_\infty)(\omega^2 - \omega_{\text{sp}}^2)}, \quad (2.61)$$

where $\omega_{\text{sp}} = \omega_p / \sqrt{\epsilon_{\text{bg}} + \epsilon_\infty}$, is the *surface plasmon frequency*.

For small wavevectors, the dispersion relation becomes $\omega \rightarrow qc/\sqrt{\epsilon_{\text{bg}}}$, where it follows the dielectric medium lightline. As the wavevector increases, the curve shall become shallower than the light line and as $q \rightarrow \infty$, the dispersion relation tends to the limiting value $\omega \rightarrow \omega_{\text{sp}}$. Here the SPP transitions between being photonic in character to becoming like a *surface plasmon*, where the field limits to being entirely confined to the surface. The diffraction limit is surpassed here as an arbitrarily large wavevector range is supported at a small frequency range, in the limit of no loss.

In this thesis, multi-layer structures will be considered that support hybrid SPP modes about one or multiple material interfaces. In general, analytical dispersion relation solutions do not exist, but rather solutions for $\mathcal{M}_{22}(\mathbf{q}, \omega) = 0$ are found implicitly, using a root-finding algorithm.

2.4. Finite Difference Time Domain

The real world exists in time domain; whereas the frequency domain is mathematically complementary, the purpose of calculations done in it must ultimately be to get a handle on the time evolution of a system. As the complexity of a system increases, analytic methods begin to get less and less tractable. In order to complement such techniques, numerical simulations may be employed. In this thesis, the *finite difference time domain* (FDTD) method [29, 30] will be used.

In FDTD, the goal is to solve Maxwell's equations for successive instants in time over a discretised lattice. This is approached by taking the curl equations, and making the time derivatives of the fields the subject. Making the assumption that there are no

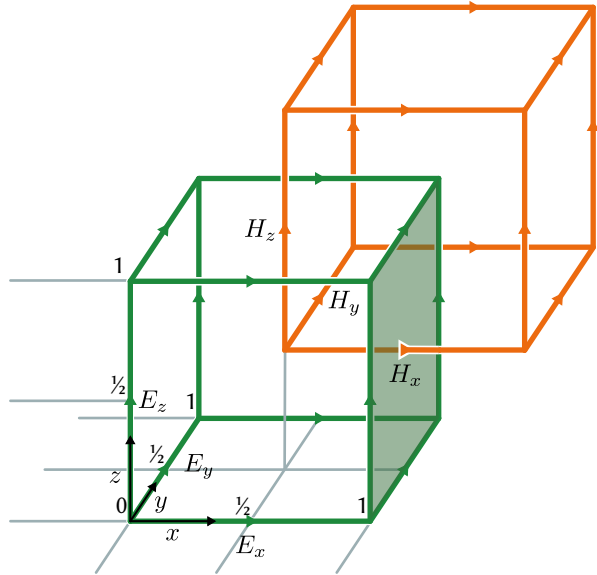


Figure 2.3: **Schematic of FDTD Yee cell.** Electric (green) and magnetic (orange) field grids. They are shifted half a step from each other, forming an interlocking link. Each field line passes through the centre of a square formed from lines of the other field, e.g. H_x here passes through the centre of the highlighted E -field face, where the finite difference $\nabla \times \mathbf{E}$ is defined.

external sources,

$$\frac{\partial \mathbf{E}}{\partial t} = \frac{1}{\varepsilon_0} \left(\nabla \times \mathbf{H} - \frac{\partial \mathbf{P}}{\partial t} \right) \quad (2.62.a)$$

$$\frac{\partial \mathbf{H}}{\partial t} = -\frac{1}{\mu_0} \left(\nabla \times \mathbf{E} - \frac{\partial \mathbf{M}}{\partial t} \right). \quad (2.62.b)$$

Now, space and time are discretised as $(t, x, y, z) \rightarrow (n\Delta_t, i\Delta_x, j\Delta_x, k\Delta_x)$ and derivatives are turned into finite differences, i.e.,

$$\frac{\partial \mathbf{E}}{\partial t}(\mathbf{x}, t) \rightarrow \frac{\mathbf{E}_{i,j,k}^{n+1} - \mathbf{E}_{i,j,k}^n}{\Delta_t}. \quad (2.63)$$

Strictly, the above is a central difference and approximates the time derivative at a time $(n + 1/2)\Delta_t$. Therefore the corresponding right-hand-side terms must be evaluated at this time. The curl operator is handled similarly,

$$\nabla \times \mathbf{E}(\mathbf{x}, t)|_x \rightarrow \frac{E_z|_{i,j+1,k}^n - E_z|_{i,j,k}^n}{\Delta_x} - \frac{E_y|_{i,j,k+1}^n - E_y|_{i,j,k}^n}{\Delta_x}. \quad (2.64)$$

In order to make best of this central difference, the lattice is arranged as a Yee grid [29], where fields are stored separately by component and \mathbf{E} and \mathbf{P} fields are specified on integer time coordinates, whereas \mathbf{H} and \mathbf{M} are specified on half integer time coordinates. The lattice coordinates are more complicated, for \mathbf{E} , components are stored at half-integer coordinates in their own direction and at integer coordinates otherwise. This is the opposite for the \mathbf{H} field, as illustrated in Fig. 2.3. From here, one can write the *update equations*,

$$\begin{aligned} E_x|_{i+\frac{1}{2},j,k}^{n+1} &= E_x|_{i+\frac{1}{2},j,k}^n - \varepsilon_0^{-1} P_x|_{i+\frac{1}{2},j,k}^{n+1} + \varepsilon_0^{-1} P_x|_{i+\frac{1}{2},j,k}^n \\ &\quad + \frac{c\Delta_t}{\Delta_x} \left(Z_0 H_z|_{i+\frac{1}{2},j+\frac{1}{2},k}^{n+\frac{1}{2}} - Z_0 H_z|_{i+\frac{1}{2},j-\frac{1}{2},k}^{n+\frac{1}{2}} \right) \\ &\quad - \frac{c\Delta_t}{\Delta_x} \left(Z_0 H_y|_{i+\frac{1}{2},j,k+\frac{1}{2}}^{n+\frac{1}{2}} - Z_0 H_y|_{i+\frac{1}{2},j,k-\frac{1}{2}}^{n+\frac{1}{2}} \right) \end{aligned} \quad (2.65.a)$$

$$\begin{aligned} Z_0 H_x|_{i,j+\frac{1}{2},k+\frac{1}{2}}^{n+\frac{1}{2}} &= Z_0 H_x|_{i,j+\frac{1}{2},k+\frac{1}{2}}^{n-\frac{1}{2}} + c M_x|_{i,j+\frac{1}{2},k+\frac{1}{2}}^{n+\frac{1}{2}} - c M_x|_{i,j+\frac{1}{2},k+\frac{1}{2}}^{n-\frac{1}{2}} \\ &\quad + \frac{c\Delta_t}{\Delta_x} \left(E_z|_{i,j+1,k+\frac{1}{2}}^n - E_z|_{i,j,k+\frac{1}{2}}^n \right) \\ &\quad - \frac{c\Delta_t}{\Delta_x} \left(E_y|_{i,j+\frac{1}{2},k+1}^n - E_y|_{i,j+\frac{1}{2},k}^n \right), \end{aligned} \quad (2.65.b)$$

with corresponding equations for the omitted components.

With the update equations of the primary fields determined, it remains to describe how the auxiliary fields update. In general, the constitutive equations are functionals of all past values of all fields, as described in Sec. 2.1.2 and Sec. 2.2.1, though this would prove tricky to directly implement. In practice, material responses can be cast in terms of a finite difference if they can be expressed in terms of a temporal differential equation. This lends the Drude-Lorentz model of Sec. 2.2.2 well to inclusion within FDTD, though its update equations and how to incorporate them are beyond the scope of this thesis.

The FDTD algorithm therefore proceeds by iterating over updating in order the **E** field, **M** field, **H** field, and **P** field over all space for each timestep.

There are limitations to FDTD. Its staggered grid structure means that material interfaces are not sharply defined, and any curvature on an interface will also experience a staircasing effect that can lead to spurious hot-spots especially in plasmonic structures where geometric effects play a key role. The grid is also regular, which is to say it can not be adaptively refined in areas of interest, rather all points must be simulated to the same resolution. This adds to the numerical load, as the smallest wavelength component of the fields, as well as the smallest geometrical features must be provided with sufficient resolution. This is again especially relevant in plasmonics, where field confinement is a feature.

Because of its nature as a full wave time domain solver, FDTD can often be the final say on a theoretical investigation. Short of doing a real-world experiment, FDTD numerical simulations find their utility as a heavy-duty tool. That is, the Maxwell's equations are solved at every discretised point in space, so it is often slower and more cumbersome, but can as a result of the inherent thoroughness produce results for questions that other techniques are unable to.

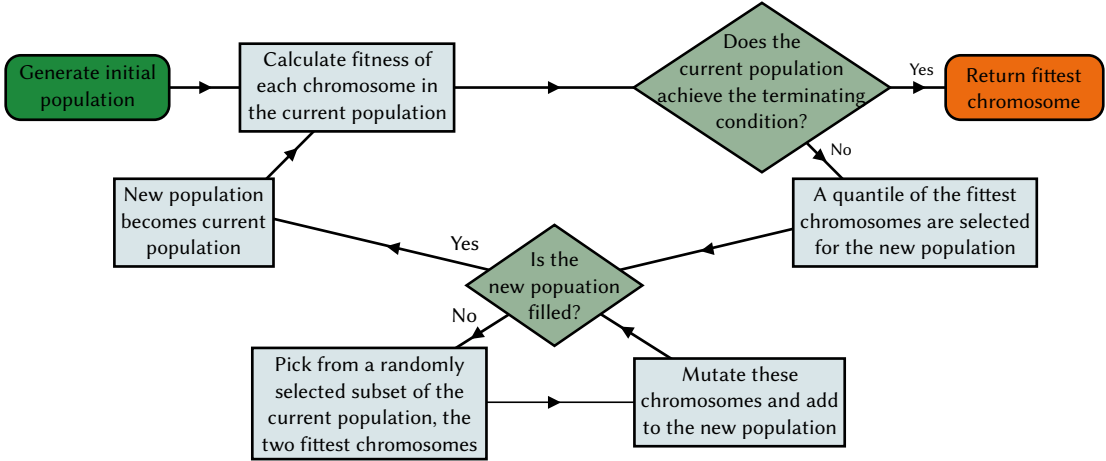


Figure 2.4: Evolutionary algorithm flowchart.

2.5. Evolutionary Algorithm

For a planar stratified structure whose properties can be determined by a transfer matrix method, one may wish to optimise some aspect of its response to electromagnetic radiation. This may be in the dispersion relation of bound modes or in the transmission and reflection spectra. For example, to prescribe the frequency of a bound mode, or a reflection peak; or set whether there is only a single mode or many modes within a frequency range; or control the amplitude and phase response to an incoming wavepacket. These properties are entirely determined by the composition of the structure, however it often not obvious how changes in the structure lead to changes in the response.

The structures to be considered can be described by a finite number of numeric or discrete parameters, i.e. for each layer: the thickness of the layer, the material model to use, and the parameters of that model. This is well suited to optimisation using an *evolutionary algorithm* (EA) [31].

In brief, an EA operates by storing multiple copies of these parameter sets, perturbing the values of the parameters randomly, ordering the sets by how the system they

describe performs against a fitness metric, and keeping only the best variants to the next round.

More fully, in the language of an EA, this would be to say that a *population* of *chromosomes* is kept, and on each iteration of the algorithm, new chromosomes are generated from *mutations* of the current ones, the next generation population is filled by *selection* of these chromosomes by a *fitness function*. The goal of the EA is to find a chromosome which extremises the fitness function globally, and as such an EA is most suitable when the evaluation of the fitness function can be performed relatively quickly as a large number of members of the state space must be evaluated and compared.

A chromosome is simply the set of parameters which describes a system, i.e. a list of numbers or discrete option values. They are atomic entities, independent of other chromosomes. Each chromosome may have its fitness function evaluated to determine how suitable its corresponding physical system is to a problem.

Each iteration of the EA holds a set of chromosomes, ordered by their fitness function, known as a *population*. The first generation is seeded population either with randomly generated structures, or structures that have been tuned by hand, perhaps by approximative theoretical methods. Populations of subsequent generations are constructed by firstly taking a small quantile of the fittest chromosomes from the previous iteration, with the remaining places filled with *mutations* of chromosomes selected from the previous set. The progress of the algorithm can be tracked by examining the fittest chromosome at the end of each iteration. At the end of each iteration, a *terminating condition* is evaluated, which determines if the algorithm should stop, returning the fittest chromosome, e.g. if the best structure in the population is within a defined tolerance of the target output, or if a set number of iterations have elapsed. If the terminating condition is not met, then the algorithm continues for another it-

eration. The operation of the EA is described as a flowchart in Fig. 2.4.

The mutation process generates a new chromosome by randomly perturbing the values of parameters of a parent chromosome. It is by mutation that the state space of chromosomes is mapped.

For the layered structures considered here, the mutation process will perturb both the properties of the layers themselves, and the relationship between layers. Numeric parameters, such as layer thicknesses and those used in material models are perturbed by a Gaussian random variable, and the discrete parameters, such as the layer model, can be randomly selected from a list. Typically only one or few parameters will be changed in each mutation. The parameters of the layers themselves don't sit in isolation. The number of layers in these structures is variable and mutation allows for adding or removing of layers or indeed swapping the order of layers and shifting the boundary between adjacent layers.

Whereas the EA is widely applicable to problems in nano-optics, the fitness function is not general and has to be constructed for each problem based on what characteristics are to be selected for. In Sec. 3.4.2 a fitness function will be defined for structures that hold light in a bound mode at zero group velocity, seeking to reduce the dispersion of a wavepacket propagating in the structure.

Chapter 3.

Plasmonic Stopped Light Lasing

3.1. Introduction

The speed at which light travels in vacuum is a fundamental property of the universe and is the upper limit on the speed at which energy can be transferred. This speed is outside the scale of normal human experience, and in the context of nano-optics is considerable at $299.792458 \mu\text{m}/\text{ps}$. This high speed does present a problem when storing light-energy, however; light does not readily slow down. In the presence of polarising or magnetising media, light will be slowed by a factor defined as the *refractive index*, which typically is no larger than about 5, with the largest bulk refractive index known being that of a metamaterial with an index of 33 [32].

The reduction in speed can be improved on by considering the wave nature of light, and in a chosen frequency interval, modifying the *dispersion relation* of a wavepacket through resonant phenomena. This is the field of inquiry of *slow* or *stopped light* (sl), and is studied within a broad range of research areas from where the resonant phenomena can be derived [33]. These range from *electromagnetically induced transparency* in cold atom gases [34, 35, 36, 37] and in solid state devices [38, 39, 40, 41, 42],

to *periodic backreflectance* in photonic crystal structures [43, 44, 45] semiconductor quantum wells [46], and *Goos-Hänchen shift* [47] in negative refractive index metamaterial structures [48, 49]. These approaches are not without issues to overcome. Applications in optical information processing would require integrated structures operating under ambient conditions, which limits the utility of cold atom gases in this context. Photonic crystals rely on periodic structuring, where stopped light resonances are vulnerable to imperfections and disorder, reducing the speeds to hundredths of the vacuum velocity but falling short of complete stopping [50, 51]. Metamaterials, on the other hand, require operation to be on lengthscales where the meta-atoms are effectively homogenised [52], and require intricate patterning within these scales [53, 54], though the chief problem with metal based metamaterials is Drude loss [55, 56].

In this thesis, stopped light is considered in the context of planar nanoplasmonic structures [57]. Plasmonic stopped light is also robust against disorder, as shown in Ref. [58], but will not be discussed in detail here. Whereas plasmonic structures are still susceptible to Drude loss faced in the metamaterial case, this can be compensated for by the inclusion of a gain material. Finally, the composition of such plasmonic structures is simple and lends itself well to experimental realisation.

Stopped light brings about an enhanced density of states [59] and allows for the localisation of light coherently over long timescales, which can enhance nonlinear effects [60] and interaction with active components [61, 62], making stopped light relevant for applications in the light harvesting of solar cells [63, 64, 65], quantum information processing [35], and optical memories [66] as well as applications in optical communications [67].

One of the implications of stopped light, that is perhaps its most interesting, is *stopped light lasing*. When designing a laser there are, broadly, two components that

must be considered - gain and feedback. Gain is the mechanism by which photons (or indeed plasmons) are generated by stimulated emission. Here a photon will induce the relaxation of an electron from one state to another of lower energy, and crucially, emit a second photon that is coherent with the first. This process can be repeated, and while the electron population is inverted (that is there are more electrons in the upper rather state, rather than the lower), will grow the number of photons in a coherent state exponentially. The gain media that are available include semiconductors in bulk [68], quantum dots [69] and wells [70], as well as organic laser dye molecules [71].

Feedback, on the other hand, is the means by which the photons emitted are coupled back to interact with the same gain medium, such that they may stimulate further emission. Most lasers will use a resonant cavity for this purpose, where the cavity modes localise electromagnetic energy over a gain medium. In the field of nanolasing there have been many such examples including photonic crystal defect modes [72, 73], microcavity resonators [74, 75, 76], and even the multiple scattering of a “random laser” [77, 78].

Stopped light offers an alternative mechanism for feedback than with a cavity. SL modes are only confined in one spatial dimension, and not in the other two. This permits a continuum of planewave solutions, i.e. SL modes are propagating waves, rather than standing waves, albeit at zero group velocity. The lasing mode of a stopped light laser forms dynamically, based on the gain support for the continuum of modes instead of being predetermined by the geometry of a cavity. Here the feedback is provided by a balance of adjacent forward and backward power flows that form a closed-loop optical vortex which gives rise to the zero group velocity.

In this chapter, we seek *stopped light structures*, these are heterogeneous media, whose dispersion relations have at least one zero group velocity point, i.e. $\text{Re} \frac{d\omega}{dq} = 0$ for some finite values of the wavevector q . In such structures, wavepackets of light

are pinned and do not drift away albeit still propagating with a finite phase velocity. Though to spatially confine light over long timescales, it is not enough just to have a zero group velocity, one needs to also minimise the dispersion and material losses.

The energy confinement of stopped light provides the basis for the feedback mechanism required for lasing to occur. Nanoplasmonic stopped light lasing is shown to provide a robust mechanism for the ultrafast excitation of coherent surface plasmon polaritons from simple, experimentally realisable, subwavelength structures.

3.1.1. Organisation of chapter

This chapter is structured as follows: In Sec. 3.2 the dispersion relation of light is explained, introducing phase, group, and dispersion velocities. This is followed by a discussion of the differences between a complex frequency and complex wavevector picture of dispersion in Sec. 3.3.

The features that make a good stopped light structure, how to find and optimise structures that possess these, and finally how to excite stopped light modes are presented in Sec. 3.4. An optimised structure is then analysed in frequency domain, including how plasmon modes can become undamped with the inclusion of a gain medium in Sec. 3.5.

Time domain simulations are performed in Sec. 3.6. These are based on a four level system model for the gain (Sec. 3.6.1). Section 3.6.2 investigates how the lasing mode is onset as gain density is increased, for a stopped light structure and a non-stopped control structure. Then in Sec. 3.6.3 the spatial and temporal characteristics of the lasing mode is examined as the width of the gain medium is reduced, exploring the confinement and output of the lasing mode.

The results are summarised and the chapter is concluded in Sec. 3.7.

3.2. Phase Velocity, Group Velocity, and Dispersion

Before entering into a study of particular plasmonic stopped light structures, we first explore how a wavepacket propagates under a dispersion relation $\omega(q)$, and how its shape evolves as it does. This will have implications, as will be shown, for the lateral confinement of such a wavepacket within a finite area.

Consider a wave propagating in one dimension x , with a well defined wavevector, q_0 , and a narrow spatial bandwidth, σ_0^{-1} , which gives it a slowly varying spatial envelope with a width $\sim \sigma_0$. Then the dispersion relation is well described by its Taylor expansion to second order about $q = q_0$,

$$\omega(q) = v_p q_0 + v_g(q - q_0) + v_d \frac{\sigma_0}{2} (q - q_0)^2 + \dots , \quad (3.1)$$

where the following velocities are introduced¹ in place of the usual derivative Taylor coefficients: *phase velocity*, $v_p = \omega(q_0)/q_0$, *group velocity*, $v_g = \omega'(q_0)$, and *dispersion velocity* $v_d = \omega''(q_0)/\sigma_0$.

A Gaussian wavepacket following this prescription has the functional form,

$$\varphi(x) = \exp \left(-\frac{x^2}{2\sigma_0^2} + iq_0 x \right) + \text{c.c.} \quad (3.2)$$

at a single instant in time, $t = 0$. In order to calculate the time evolution of the wave packet, the function needs to be expressed in the Fourier domain, where the dispersion relation applies,

$$\tilde{\varphi}(q) = \frac{1}{2\pi} \int_{-\infty}^{\infty} dx \varphi(x) e^{-iqx} \quad (3.3)$$

$$= \frac{\sigma_0}{\sqrt{2\pi}} \exp \left(-\frac{\sigma_0^2(q - q_0)^2}{2} \right) . \quad (3.4)$$

¹ If three separate velocities seems a lot, in 1977, S. C. Bloch reviews seven previously identified velocities of light in dispersive media and introduces his own eighth [79].

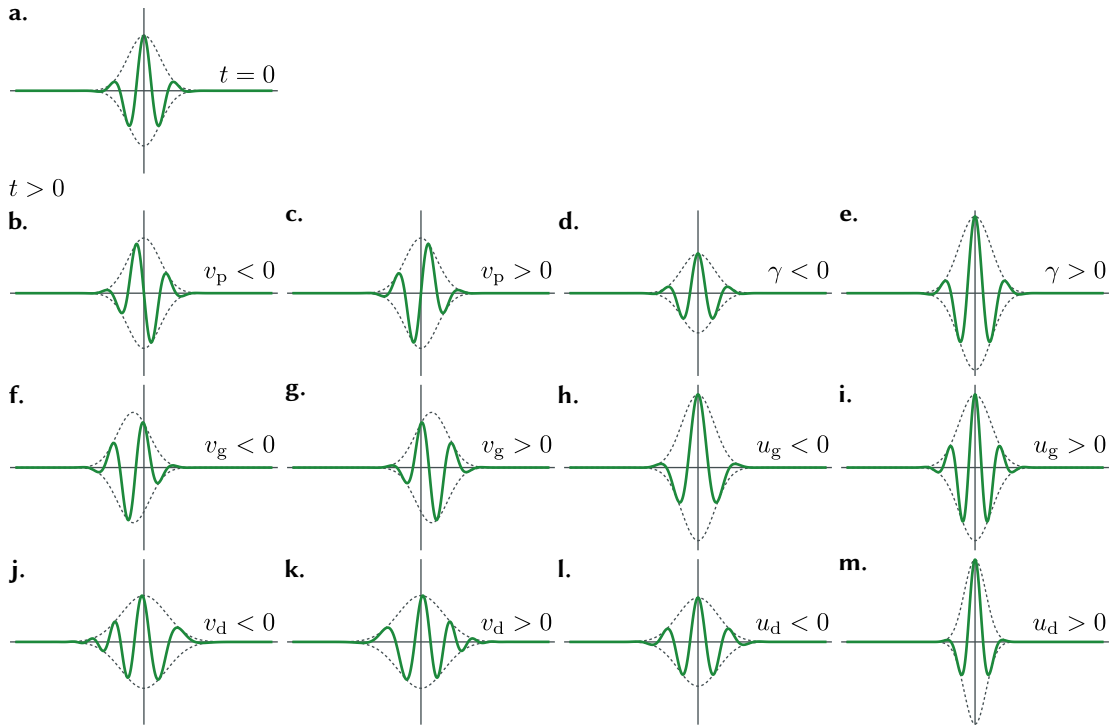


Figure 3.1: Effect of moments of the dispersion relation.

A Gaussian enveloped planewave at $t = 0$, a, is shown individually under the effects of the moments of the dispersion relation for $t > 0$. Subfigures are paired to have a negative then positive value of an individual moment, with all others set to zero.

b, c. phase velocity v_p - envelope remains constant as phase advances.

d, e. loss γ - amplitude of the envelope decreases/increases.

f, g. group velocity v_g - envelope shifts as phase remains constant.

h, i. group loss u_g - amplitude of envelope increases as phase wavelength increases/decreases.

j, k. dispersion velocity v_d - envelope widens and a negative/positive chirp is induced.

l, m. dispersion loss u_d - envelope widens/narrows with no chirp.

In this basis, the time evolution is simply given by multiplication by the propagator $e^{-i\omega(q)t}$,

$$\tilde{\varphi}(q, t) = \tilde{\varphi}(q) e^{-i\omega(q)t}. \quad (3.5)$$

The wavepacket then becomes,

$$\tilde{\varphi}(q, t) = \frac{\sigma_0}{\sqrt{2\pi}} \exp\left(-\frac{(\sigma_0^2 + iv_d\sigma_0 t)(q - q_0)^2}{2} - iv_g(q - q_0)t - iv_p q_0 t\right), \quad (3.6)$$

which when transformed back, yields the form,

$$\varphi(x, t) = \sqrt{\frac{1}{1 + iv_d t / \sigma_0}} \exp\left(-\frac{(x - v_g t)^2}{2(\sigma_0^2 + iv_d\sigma_0 t)} + iq_0 x - i\omega_0 t\right) + \text{c.c.} \quad (3.7)$$

or,

$$\begin{aligned} \varphi(x, t) &= \varphi_0(t) \exp\left(-\frac{(x - v_g t)^2}{2\sigma(t)^2}\right) \exp(iq_0(x - v_p t)) \\ &\times \exp\left(i\frac{(x - v_g t)^2}{2\sigma(t)^2} \frac{v_d t}{\sigma_0}\right) \\ &+ \text{c.c.} \end{aligned} \quad (3.8)$$

with the following definitions made: $\sigma(t)^2 = \sigma_0^2 + (v_d t)^2$, and $\varphi_0(t) = \sqrt{\frac{\sigma_0^2 - i\sigma_0 v_d t}{\sigma(t)^2}}$.

Examining Eq. 3.8 term by term; the first two exponential terms determine that this is a Gaussian function that is modulated with a planewave of wavevector q_0 , as in Eq. 3.2. The modulation now has a *phase velocity* v_p , and the envelope is centred on $v_g t$, a point that moves in time with the *group velocity* v_g . The width of the Gaussian increases over time, as determined by $\sigma(t)$, which increases over time proportionally to the *dispersion velocity* v_d and decreases the peak amplitude of the pulse as it spreads, as determined by $\varphi_0(t)$. The final term is a complex phase factor that determines the *chirp* of the wave, which at any instant in time, gives a spatial factor $\exp(iq_c^2 x'^2)$ (for $x' = x - v_g t$, and q_c is a time-dependant constant), which is a complex phasor with a wavelength that decreases away from a central point. Another way to envisage this is, when the dispersion relation has a positive curvature, the local group velocity $\frac{d\omega}{dq}(q)$

is higher for larger wavevectors than for small ones, as such higher wavevector components make their way to the front of the wavepacket, leaving the low wavevector components at the back.

The previous analysis has presented the time evolution as though the dispersion relation were real valued, whereas in general, each of the moments has an imaginary part, which will be denoted as,

$$\omega(q) = \text{Re } \omega(q) + i\gamma + iu_g(q - q_0) + iu_d \frac{\sigma_0}{2} (q - q_0)^2 + \dots . \quad (3.9)$$

For even order moments γ and u_d , the loss and dispersion loss, positive values represent gain whilst negative represent loss. The odd moment u_g , the group loss, is alternatingly gainy or lossy either side of the central wavevector, with the effect of shifting the central wavevector over time. The effect of all the moments of the dispersion relation is plotted in Fig. 3.1.

The resulting expansion of a Gaussian pulse evolution is lengthy, therefore its explicit expression will be omitted here. The group loss and dispersion loss terms each contribute to the complex phase of the wavepacket, though this will not be explored further. The effect on the amplitude however is to multiply by an exponential factor and to apply a spatial convolution by an additional broadening term²,

$$\varphi(x, t) \rightarrow \exp \left(\gamma t - \frac{u_g^2}{2u_d\sigma_0} t \right) \times \frac{\exp \left(\frac{x^2}{2\sigma_0 u_d t} \right)}{|\sigma_0 u_d t|} \otimes_x \varphi(x, t) . \quad (3.10)$$

These additional terms are present because the imaginary part of the dispersion relation will change the profile of the wavevector spectral density over time,

$$|\varphi(q, t)|^2 \propto e^{2[\text{Im } \omega(q)]t} . \quad (3.11)$$

This is in contrast to the real moments of the dispersion relation, which do not alter the spectral density.

² For this second order Taylor expansion model to remain valid, the loss dispersion, u_d should satisfy,

$u_d \leq 0$ and $|u_d| \gtrsim |u_g|$.

This section has explained how the dispersion relation affects the space-time propagation of band-limited electromagnetic radiation. By engineering the dispersion relation, via choice of materials and structuring, one may seek to control the pulse propagation itself. This is to include control over the shape of a pulse, and how it drifts and disperses, but also the phase relations and chirping.

3.3. Complex Wavevector and Complex Frequency

The dispersion relation of the modes of a planar heterostructure, as discussed in Sec. 2.3.3, is determined as the condition required to maintain a nonzero electromagnetic field within a structure in the absence of an external driving field. The solutions are planewaves in a direction of propagation perpendicular to the stacking of the heterostructure, i.e. $\exp(iqx - i\omega t)$, and the dispersion relation is the range of allowed q and ω value pairs. The dispersion can, of course, be expressed in functional form as either $q_i(\omega)$ or $\omega_i(q)$, where i is the mode index. The functions are called the *complex wavevector* (cwv) and *complex frequency* (cf) representations, respectively. In general both quantities are complex, but expressing them in functional form allows for the function argument to be given as a real eigenvalue parameter. Both descriptions are equivalent, and describe the same space time dynamics.

Consider a structure with a single mode, with a monotonic dispersion relation. Its spacetime profile can be expressed in the complex wavevector picture as,

$$\varphi(x, t) = \int_{-\infty}^{\infty} d\omega \tilde{\varphi}(\omega) e^{iq(\omega)x - i\omega t}, \quad (3.12)$$

which could be interpreted at face value as in integral along the real axis, or alternatively as a complex contour integral along the path $\omega(s)$,

$$\varphi(x, t) = \int_{-\infty}^{\infty} ds \frac{d\omega}{ds} \tilde{\varphi}(\omega(s)) e^{iq(\omega(s))x - i\omega(s)t}. \quad (3.13)$$

If the path is chosen such that $q(\omega(s)) = s$ for all $s \in \mathbb{R}$, then the integral becomes,

$$\varphi(x, t) = \int_{-\infty}^{\infty} ds \tilde{\varphi}(s) e^{isx - i\omega(s)t}, \quad (3.14)$$

with $\tilde{\varphi}(s) = \tilde{\varphi}(\omega(s)) \frac{d\omega}{ds}$, and this is exactly the complex frequency representation, as parameterised by a real wavevector s . The mode's spectral content $\tilde{\varphi}(\omega)$ is analytically continued from the real axis to the curve $\omega(s)$.

Given the equivalence of the two pictures, the utility of each must be discussed. The complex frequency picture is parameterised with a real wavevector eigenvalue; this means that it is a description suited to having a wavepacket with a known spatial distribution at one instant in time, and calculating the time evolution, i.e. having energy stored in a structure and calculating how it dissipates.

The complex wavevector picture on the other hand, is suited to knowing the time evolution of a wavepacket at a single point in space, and then calculating the propagation of the wave through space. e.g. calculating propagation in a fibre-optic cable with a known signal input at one end.

For stopped light, it is the complex frequency representation that is the most useful. This can be justified both intuitively and mathematically. Intuitively, we will want to determine the propagation of a wavepacket with losses at the zero group velocity point. It makes little sense to consider the complex wavevector (losses in space) picture as, by construction, we are considering wavepackets that do not propagate in space. Conversely losses in time are indeed a meaningful quantity for a stationary wavepacket.

Mathematically speaking, for a structure with at least one stopped light point, i.e. where $\text{Re } \frac{d\omega}{dq} = 0$ for a finite q , this is just a turning point in an $\omega(q)$ description, whereas in a $q(\omega)$ picture, this is a singular point, and multiple branches of the function must be considered to capture the behaviour about the point.

In practice, stopped light points don't even manifest themselves in the complex

wavevector solutions [80, 59], therefore from here on, the complex-frequency picture is used to analyse the SL modes of structures under consideration.

Though the complex-wavevector picture can not describe stopped light itself, it will be shown that it is well suited to describing the plasmons that are emitted as an output channel from stopped light lasing.

3.4. Plasmonic Stopped Light Structures

In order to confine light longitudinally in a waveguide, a wide range of wavevectors must be supported within a narrow frequency range. A way of achieving this would be to use a structure that supports two *zero group velocity* (zgv) points on the same mode. A zgv point defines a turning point in the real part of the dispersion relation, i.e. $\text{Re} \frac{d\omega}{dq}(q_0) = 0$. By definition, having two adjacent zgv points implies that the dispersion relation in-between is necessarily monotonic, since no further turning points can exist within the interval. It is also guaranteed that a point of zero dispersion, $\text{Re} \frac{d^2\omega}{dq^2} = 0$, (see Sec. 3.2) exists in the range.

The range of wavevectors between the two zgv points is referred to as a *stopped light band*. The quality of such a band will be determined by two factors, how narrow the frequency bandwidth is, and how broad the wavevector bandwidth is. For a pair of stopped light points zgv 1 and zgv 2, the frequency and wavevector bandwidths are given as $\Delta_\omega = \omega_2 - \omega_1$ and $\Delta_q = q_2 - q_1$ respectively. This allows for the definition of the *band velocity* v_b , which is the average group velocity between the zgv endpoints,

$$v_b = \frac{\omega_2 - \omega_1}{q_2 - q_1} = \frac{\Delta_\omega}{\Delta_q} . \quad (3.15)$$

The wavevector bandwidth determines the minimum width that a light pulse can be confined to, i.e. $\sim 2\pi/\Delta_q$, whereas the frequency bandwidth will set the overall flatness of the band, and additionally ensures the operation of the stopped light device to

remain quasi-monochromatic, which becomes important as the stopped light mode is coupled to inverted emitters in a narrow frequency band (see Sec. 3.5).

For this study, we consider structures with materials characteristic of a III-V semiconductor, i.e. InGaAsP for dielectric layers, and a transparent conducting oxide [81], such as Indium Tin Oxide (ITO) for metallic layers. The dielectric is modelled with a constant permittivity $\epsilon = 11.68$. ITO, which has a plasma resonance in the visible which can be tuned by doping, allowing for operation in the near infrared (i.e. at telecoms wavelength [$\lambda \approx 1550$ nm]). It is modelled by a Drude model with parameters as given in Tab. 3.1 provided by experimental data [82], with the loss reduced by a factor of 10, which can be achieved through high fabrication quality and at low temperatures [83].

3.4.1. Mode Hybridisation

The dispersion of plasmonic structures is ultimately determined by how its layers are composed, i.e. their thickness, material, and relative ordering. It is possible to predict, and even control, how the dispersion relation will look before explicitly calculating it. Having such a model becomes useful in reducing the search space of optimisation methods discussed in the next section, since calculating the dispersion relation consists of solving a transcendental equation, which requires numerical methods.

The predictive power stems from the spatial profile of the plasmonic mode having peaks on metal/dielectric interfaces with exponential tails,

$$\varphi(z) \propto \begin{cases} \exp(-\text{Im } \kappa_+(q)(z - z_0)) & z > z_0 \\ \exp(\text{Im } \kappa_-(q)(z - z_0)) & z < z_0 \end{cases}, \quad (3.16)$$

where $\text{Im } \kappa(q) > 0$, and broadly increases with q . For small values of q , the tails are broad and the mode overlaps with the rest of the structure, whereas for large q the mode only sees the interface which it sits at. Each metal/dielectric interface hosts a

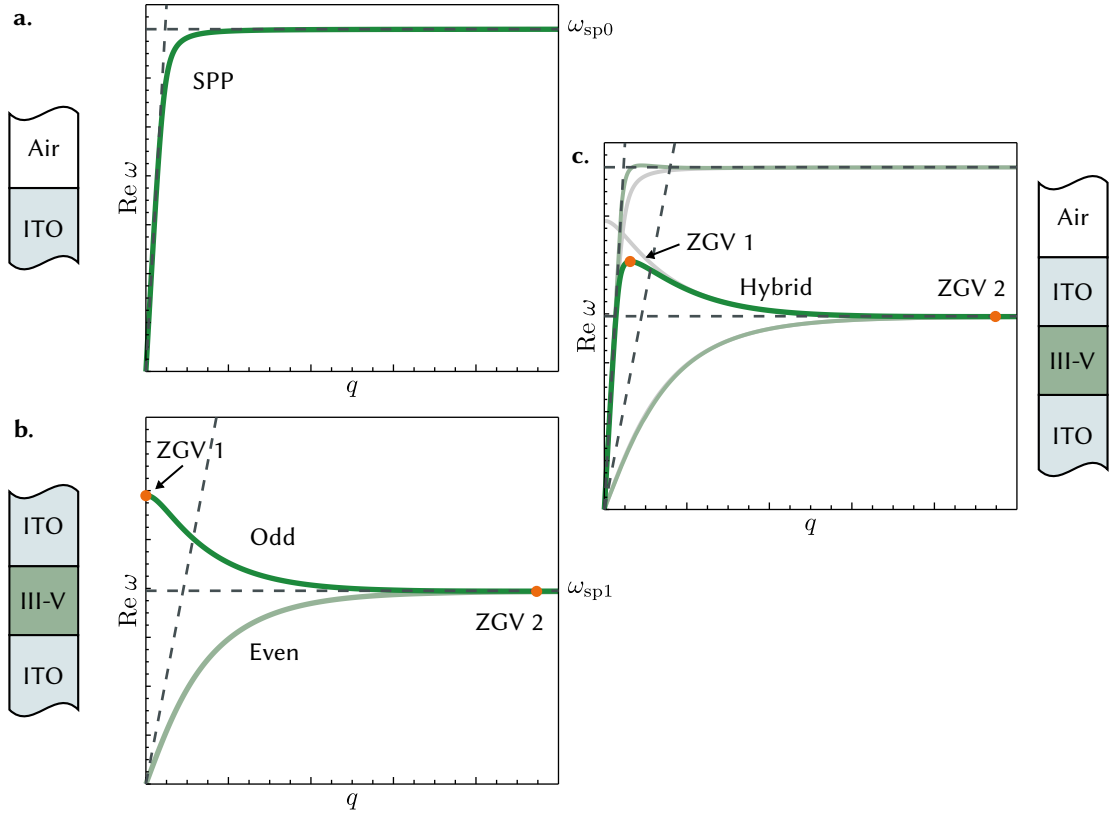


Figure 3.2: Hybridisation of modes.

Dispersion relations, $\text{Re } \omega(q)$, are plotted, with the asymptotic light lines in vacuum $\omega = cq$, and in dielectric $\omega = cq/\varepsilon_{\text{bg}}^2$, and surface plasmon frequencies, $\omega_{\text{sp}0} = \omega_p/\sqrt{\varepsilon_\infty + 1}$ and $\omega_{\text{sp}1} = \omega_p/\sqrt{\varepsilon_\infty + \varepsilon_{\text{bg}}}$. Modes of interest are highlighted in deep green, and zgv points marked in orange. a. The SPP mode of a metal-air interface, is hybridised with b. the odd mode of a metal-insulator-metal structure, c. forming a metal-insulator-metal-air structure in order to produce a mode with two zero group velocity points at finite wavevector. The modes of the “base structures” are included in the background of c. to show the hybridisation.

surface plasmon, and at low wavevectors they will overlap and hybridise, while for high q they will decouple.

This was shown in Ref. [57] with a metal substrate underneath two dielectric layers, a high index beneath a low index dielectric. The dispersion relation initially followed the steeper plasmon dispersion of the metal/low-index overshooting the lower frequency of the asymptotic metal/high-index surface plasmon frequency which it would tend to for high wavevectors. This produced a ZGV point between the two regimes, that was somewhat tunable by the thickness of the middle layer.

A similar approach can be used for introducing *two* stopped light points. The two modes to hybridise are that of a *metal-insulator-metal* (MIM) system [84], and a *metal-air* (MA) plasmon. The structures and dispersion relations are plotted in Fig. 3.2. The MIM system has two modes, even and odd; the odd mode (in the z component of the E-field) contains two ZGV points itself, the first one is at zero wavevector and is not useful being inside the light cone, the second one is at a high wavevector near where the even and odd modes become degenerate, and is preserved.

In the combination structure, that is a *metal-insulator-metal-air* (MIMA) system, the odd mode of the MIM system hybridises with the MA plasmon, removing the zero-wavevector ZGV point but introducing a new point in the overlap. The second ZGV point can also be perturbed and gets pulled in to a lower wavevector value, depending of the precise structural configuration.

The positions of the ZGV points can be tuned by adjusting the thicknesses of each layer, while further fine control can be attained by introducing additional dielectric layers [85].

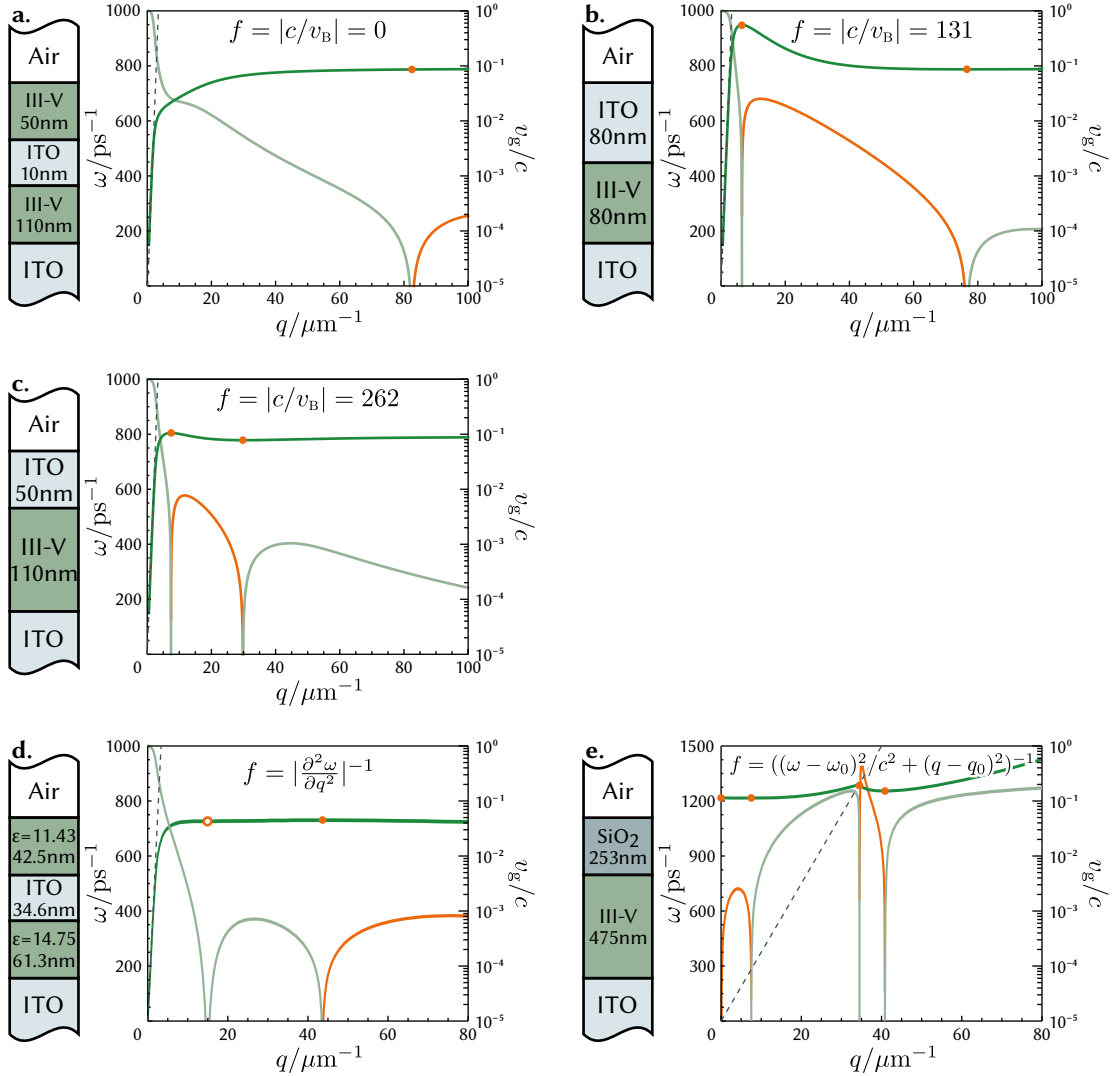


Figure 3.3: Evolutionary optimisation of stopped light structures.

The dispersion relation, group velocity, and fitness metric of a number of SL structures. a, b, and c. are tested against the band velocity metric. d. and e. are examples of structures tested under alternate metrics and with relaxed conditions on materials and layer thicknesses, i.e. (d) Minimising the second derivative (dispersion) at a ZGV point, (e) Placing the ZGV point at $q = 1 \text{ nm}^{-1}$, $\omega = 2\pi c/1550 \text{ nm}$ for a *leaky mode*.

3.4.2. Evolutionary Optimisation

Any given stopped light structure can be optimised using an evolutionary algorithm, as detailed in Sec. 2.5. The algorithm is seeded with a structure that already has two stopped light points in one band, as prescribed in the previous section. The algorithm then generates a number of similar structures, and for each, the dispersion relation of the corresponding band is calculated. The structures are assigned and ordered by a fitness metric, where structures without two ZGV points are flauchnauchnihilipilified and immediately discarded. The remaining structures are then passed through the EA routine for mutation, recombination and selection. For the purpose of identifying ZGV points, only the real part of the group velocity is required to be zero, this is despite the dispersion relation itself being complex (see Sec. 3.2) as it is the real part that determines the shift of the mode over time.

In order to quantify the quality of a stopped light structure, a fitness metric must be defined and calculated. In general this is a functional of the dispersion relation, $f[\omega(q)]$, (either over the whole curve, or just between the ZGV points). In practice though, this can be reduced in complexity, and it suffices to just consider a function of the bandwidths $f(\Delta_q, \Delta_\omega)$. The landscape of their possible values needs to be considered and how changes in both variables makes a more or less desirable structure.

The band velocity on face value would seem to be a suitable parameter, as,

$$f(\Delta_q, \Delta_\omega) = 1/|v_b| . \quad (3.17)$$

A subtlety does however arise, in that the second ZGV point can tend towards an infinite value of q_2 for finite ω_2 . This will send the band velocity to zero, but allows for an arbitrarily large frequency bandwidth. To counteract this, a high wavevector cutoff is introduced at around $q_c \approx 2\pi/10$ nm, which modifies the wavevector bandwidth to $\Delta'_q = \max(q_2, q_c) - q_1$ which then enters the metric.

Three candidate SL structures are contrasted in Fig. 3.3. Each of them representing a III-V / ITO heterostructure, but with varying layer configurations, each layer optimised to the nearest 10 nm. The first is an example of a structure with a single stopped light point, which would be rejected by this particular configuration of the EA as it fails to possess two ZGV points, and hence cannot be assigned a fitness metric. The second structure possesses two ZGV points and covers a wide range of wavevectors, hence represents a good candidate with a fitness metric of $f = 131/c$. The third structure is an optimised version of the previous one with a lower band velocity, giving a fitness of $f = 262/c$. Albeit its ZGV points are closer together in q , there is a smaller frequency gap, which results in a band velocity around half of its predecessor. The gradient of the bands can be seen from the dispersion diagram, the dispersion in Fig. 3.3.c exhibits a much flatter band than in b.

Two further structures are presented, these have been optimised by the EA but with less strict constraints and with different fitness metrics. The first seeks to minimise the dispersion, $\frac{\partial^2 \omega}{\partial q^2}$ at a ZGV point, rather than the band velocity. This effectively brings two ZGV points to coalescence rather than spreading them out, which doesn't guarantee a wide band. Here a third ZGV point appears in the vicinity of the first two, this does not contribute directly to the metric, but does make an overall stronger SL structure. The disadvantage to this approach, is that a *second order* ZGV point is fragile; Akin to the repeated root of a quadratic equation, a perturbation of parameters could lead to either two separate ZGV points, or indeed none at all. Structures can only be tuned to a degree before fabrication tolerances and disorder will smear their properties.

The second additional structure is one which considers *leaky modes*, where the fields in the air layer are exponentially growing, rather than decaying, and the bound modes appear within the light cone. Leaky modes optimised by this method were

analysed for the *photonic* structure presented in Ref. [86]. For the structure in Figure 3.3.e, the target was to place a ZGV point at telecoms frequency $\omega = 2\pi c/1550$ nm at a wavevector of $q = 1 \mu\text{m}^{-1}$. i.e. $f = ((\omega - \omega_0)^2/c^2 + (q - q_0)^2)^{-1}$. This structure used the material properties of Silicon and Silicon Dioxide in two dielectric layers, with arbitrarily precise thicknesses. Whereas this structure will not be considered here, as its modes are photonic in character, a case which has been treated separately [86], it serves to illustrate the versatility of the EA for designing structures.

The optimised SL structure that is used within the rest of the chapter is presented in more detail in Fig. 3.4 with properties in Tab. 3.2. It is composed of an ITO substrate on the bottom, and a semiconductor layer sandwiched between an ITO strip on top with layers optimised to the nearest 10 nm. The modes of this structure are shown alongside in Fig. 3.4.b, and indeed the bound TM 1 mode hosts two ZGV points. As a result it exhibits a very flat band with a band velocity of $v_b = -c/262$. The mode profile of the energy density of a planewave in the mode is also shown in dependence of the wavevector q . Being plasmonic in nature, the field is peaked on the interface between the metallic and dielectric layers, and for low q values, where the dispersion follows the light cone, it is primarily located in the air layer, entering the structure for higher q values. The field has significant value throughout the profile of the dielectric layer for wavevectors between around $q \in [0.002, 0.025] \text{ nm}^{-1}$, i.e. while the plasmons that sit on either side of the dielectric are coupled. This enhancement of fields is important for stopped light lasing, as it provides a large overlap between the field profile and an embedded gain medium.

For completeness, the CWW modes are also presented in Fig. 3.4. To avoid confusion with the ZGV points of the CF modes, the complex wavevector is labelled β rather than q as previously. There are an infinite range of CWW modes, each with increasing imaginary component; the first four are listed here. The modes map to the CF set in

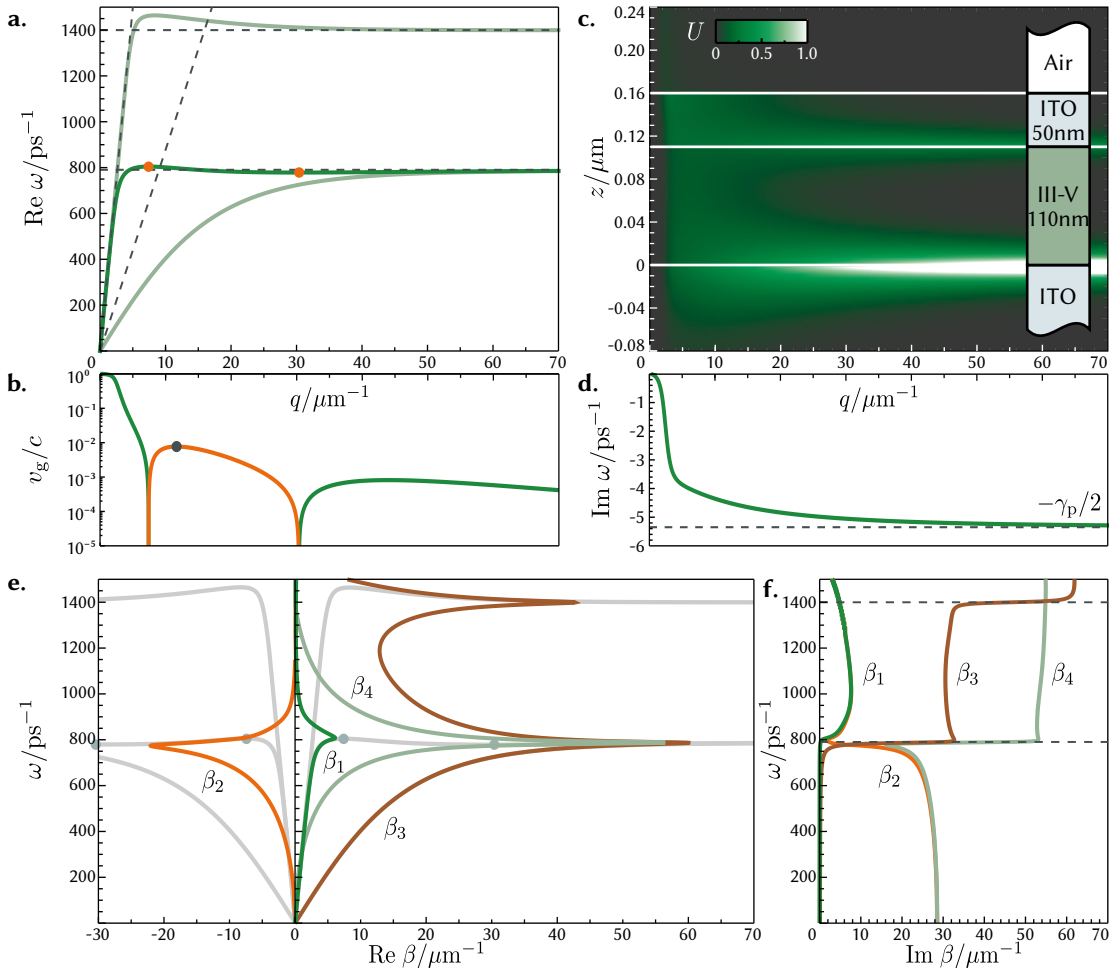


Figure 3.4: Dispersion relation of a stopped light structure.

- Complex frequency mode dispersion relations - The mode of interest is highlighted in deep green and its zgv points marked as orange dots. Also marked are the light line and surface plasmon frequency, both for the vacuum and dielectric.
- Group velocity log plot of the mode of interest - Positive group velocities in green, negative in orange. The point of zero dispersion is marked in grey.
- Description of the structure and energy density throughout the structure of a planewave of wavevector q in the bound mode.
- Modal loss, $\text{Im } \omega(q)$, up-to the limiting value of $-\gamma_p/2$.
- Complex wavevector modes $\text{Re } \beta(\omega)$ - The first four modes are plotted, the second mode (orange) is of negative phase velocity. The complex frequency modes are plotted in the background to show the correspondence.
- Modal loss, $\text{Im } \beta(\omega)$, of corresponding complex wavevector modes.

particular places on the dispersion curve, but pick up large loss where they diverge.

Having, to a large degree, removed the effects of drift and dispersion from our system, by choosing one with a wide flat band, we are left with loss as the mechanism that will hinder energy confinement. For all wavevectors where the dispersion relation departs from the light line, the system experiences a loss of around $-2 \operatorname{Im} \omega \approx \gamma_p \approx 11 \text{ ps}^{-1}$. This will dissipate any energy within the system on such a timescale. Naturally, the question arises, whether the loss be compensated for, such as by replacing the dielectric layer with a semiconductor medium, or by explicitly adding emitters such as quantum dots or gain molecules.

3.4.3. Excitation of Stopped Light Modes

Once a suitable stopped light structure has been selected, the next step is to excite the stopped light mode. The usual methods for coupling to a plasmonic waveguide become unsuitable in the stopped light case. Bound modes by definition are not coupled to external radiation modes, which is to say that light energy cannot be transferred to a bound mode by a beam of light incident on the surface. This is also linked to the secondary reason, that there is a mismatch between the wavevector of incident light and the bound modes of a plasmonic structure, along the direction of propagation³. Incident light is located exactly on the light cone in energy-momentum space and has a projection in the propagation direction within it, whereas plasmonic modes are on a line that sits outside the light cone, and indeed need not be bounded at all in momentum.

In plasmonic structures, one method of coupling is achieved by adding a local spatial inhomogeneity, such as a prism, or a grating. In the case of the prism, light is sent

³ The wavevector component normal to the stack is not conserved, so it suffices to consider the projection in the propagation direction

down the prism, within the prism's shallower light cone ($q \leq n\omega/c$), this allows for points where the energy and momentum of both the incoming beam, and the plasmon mode match [87]. In addition to this condition, the prism must be finite in extent, as the incoming light is part of the radiation spectrum of the “waveguide with prism” system that will ultimately be transmitted, reflected, or absorbed. This mode will mix with both the radiation modes and bound modes of the “waveguide without prism” system, and will decouple from the prism further down the waveguide.

A grating, which is a periodic patterning of the waveguide along the propagation direction, acts in a similar way [88]. The regular patterning allows for scattering between wavevector modes that are integer multiples of the grating wavevector, $2/d$, where d is the period. This gives a *momentum kick* to the incident light field, allowing it to match with the dispersion relation of the bound mode. Again, the radiation mode of the “waveguide with grating” system then mixes with the bound and radiation modes of the “waveguide without grating”.

These methods are ineffective with stopped light structures because the bound mode has a low group velocity such that the incident light is unable to get sufficiently far away from the grating or prism and instead is outcoupled back through the radiation modes of the combined structures, instead of travelling far enough for the system to be described by modes without a grating or prism.

Another scheme for incoupling light to a waveguide is end-fire coupling [89]. Here the waveguide is assumed to terminate in a plane perpendicular to the direction of propagation. If a light pulse is incident on this terminal plane, its profile can be decomposed into a mixture of bound modes and radiation modes of the waveguide; the radiation modes propagate away, leaving the bound modes in the system. This too is unsuitable for exciting stopped light modes, as zero group velocity modes will not propagate down the structure, they will not enter and instead be reflected back. This

method of excitation is equivalent to using the complex wavevector picture, where the temporal profile of excitation at one point along the axis (the terminal) is known, but as explained in Sec. 3.3, zGV points are not well described in the complex wavevector picture.

A final way to excite the bound modes of a plasmonic waveguide, that is compatible with stopped light, is to have them emitted directly from within the structure. Here, an emitter would be placed within the SL structure and these would be pumped to an excited state, such that when they relax, by spontaneous or stimulated emission, they are able to emit directly into the bound stopped light mode.

3.5. Frequency Domain Gain in the Small Signal Gain Regime

Adding gain to a structure will alter the bound modes that are supported. A material that can spontaneously emit photons will also be available to emit via stimulated processes, thereby adding gain to the system. This gain will be dispersive in two senses, firstly different frequencies experience different amounts of gain, and secondly any change to the imaginary part of the refractive index (i.e. the material gain) will in turn induce a change in the real part of the refractive index due to causality and the Kramers-Kronig relations (Sec. 2.2.1). Designing an active SL structure requires particular care that the introduction of a gain medium does not damage the stopped light character of the waveguide.

The induced change in mode structure can be analysed using the same transfer matrix methods of the previous section with the inclusion of a Lorentz resonance (Sec. 2.2.2) at a defined emission frequency, ω_e , to one of the dielectric layers. The Lorentz resonance represents the transitions between the levels of a two-level system

with an energy difference $\hbar\omega_e$. In this picture, there is an occupation density of upper and lower levels, averaged over space, of single two level emitters. The strength of the resonance is proportional to the *inversion density* of the two levels, i.e. how much more the higher level is occupied than the lower one, $\Delta_N = N_2 - N_1$, such that a layer with emitters embedded may be represented by :

$$\varepsilon = \varepsilon_{bg} + \frac{\omega_{pe}^2}{\omega_e^2 - \omega(\omega + i\gamma_e)} \quad (3.18.a)$$

$$\omega_{pe}^2 = -\Delta_N \sqrt{\varepsilon_{bg}} \gamma_e \sigma_e c, \quad (3.18.b)$$

where ε_{bg} is the permittivity of the layer hosting the resonance, σ_e is the emission cross-section, and γ_e is the width of the resonance [90]. Note that for negative inversion, the emitter becomes an absorber as there is a higher density of emitters in the lower state.

The SL structure as presented in the previous section is modified by replacing the dielectric layer with a Drude-Lorentz emitter (with a 10 nm buffer on both ends of zero inversion density to simulate quenching by the metal layer). The emission frequency is set to match either one of the zgv points, and the other parameters are set as in Tab. 3.1 representing the inclusion of realistic laser dye molecules [71]. The resulting dispersion and loss relations are shown in Fig. 3.5 for inversion densities Δ_N varying between 0 and N , with a fixed emitter density, and excitation about zgv 1 and zgv 2. The first point of note is that, even on full inversion, the addition of gain does not significantly change the dispersion, with the maximum shift in frequency being around 0.6%. The presence of zgv points is preserved, though they may drift slightly, i.e. zgv 2 moves slightly right with emission about zgv 1. There is no change at the frequency that is being excited, this is because the permittivity change of a Lorentzian is zero at the resonant frequency. Adding gain has the side effect of making the structure a slightly better SL structure as the band velocity is marginally reduced.

The key change though is in the loss. As the inversion density increases, the loss

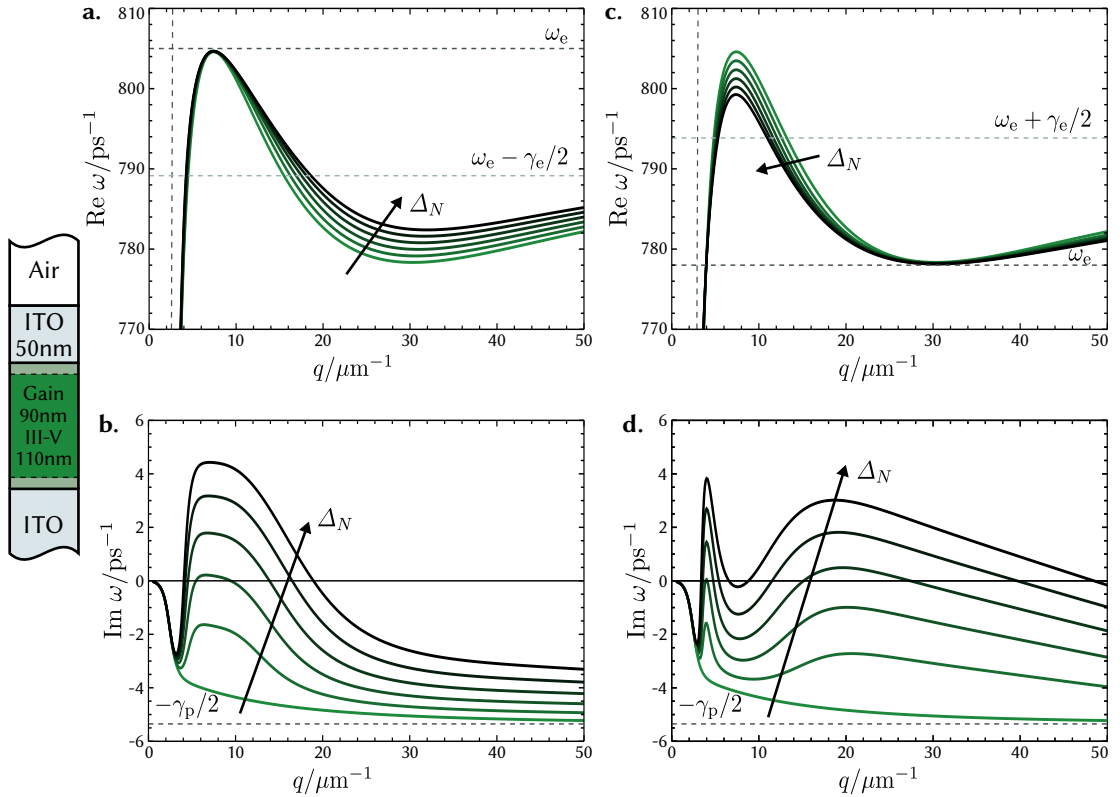


Figure 3.5: Perturbation of dispersion relation and loss with Lorentzian gain.

The change of mode shape is plotted as Lorentzian gain is introduced to the system. For subfigures on the left, emission is about zgv 1, and on the right about zgv 2. a. and b. shows a zoom in of how the dispersion relation changes with increasing inversion density, while c. and d. show the corresponding loss/gain of the mode.

decreases for wavevectors where the dispersion is within the gain width. Initially the plasmons loss is reduced as the inversion increases, then for an inversion of around $\Delta_N/N \approx 0.4$ some wavevectors become undamped, and even eventually experience gain. Plasmons sitting in these modes will grow exponentially in amplitude whilst small enough to remain in the small signal gain regime. As zgv 2 is flatter than zgv 1, when the emission is about this point, a wider range of frequencies fall within the gain width, leading to a larger range of q values that can become undamped.

3.6. Time Domain Simulations

A frequency domain analysis can only bring insight so far when describing processes such as gain, as it is unable to describe nonlinearities. When plasmons are emitted, electrons are demoted from higher energetic states to lower ones. This depletes the population inversion, reducing the available gain over time, leading to nonlinear dependence in the field strength. In addition there are spatial effects to consider, such as spatial hole burning; the TMM has assumed uniformity in the direction of propagation, whereas the level of inversion can vary both in this direction and perpendicular to the stacking. Depending on the mode formed, some regions may host higher field densities which can deplete the local gain. Thus a dynamic, spatially resolved, time domain simulation is required to capture all the aspects of emission into a stopped light mode, and as such, in this section results from FDTD simulations are presented.

3.6.1. Four-Level System

The two level system, presented in the previous section, is good for modelling a single electronic transition, however its inversion density had been set “by hand”. There is no way in which a two level system can reach a state of inversion by relying solely on

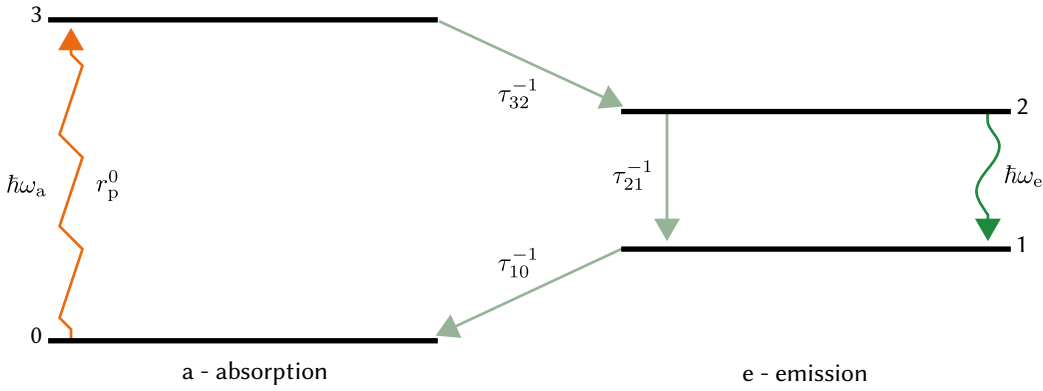


Figure 3.6: Schematic of the four-level system.

A four-level system is composed of two two-level systems, a and e, with active transitions ($0 \leftrightarrow 3$) and ($1 \leftrightarrow 2$) respectively, which are coupled by nonradiative transition rates τ_{32}^{-1} and τ_{10}^{-1} . In this scheme, the emission subsystem permits radiative transitions at an energy of $\hbar\omega_e$ and has a slow nonradiative recombination rate τ_{21}^{-1} , while the absorption subsystem is electrically pumped at a constant rate r_p^0 .

the processes of spontaneous emission and absorption (the best that can be achieved is equal occupation of the levels). A *four-level system* on the other hand can be constructed such that there can be a dynamically maintained population inversion between two of its levels, from where stimulated emission can occur. The construction contains two two-level systems, labelled e and a for emission and absorption; e is a system with energy levels 1 and 2 and energy gap $\hbar\omega_e$, in-between a, a system with energy levels 0 and 3 and greater energy gap $\hbar\omega_a$, as depicted in Fig. 3.6. The two upper levels, 2 and 3 are coupled by a fast nonradiative relaxation channel, with rate τ_{32}^{-1} , as are the two lower levels, 0 and 1 (τ_{10}^{-1}). This has the effect of rapidly depleting the 1st and 3rd level shortly after they become occupied. Between the levels of the emission two-level subsystem, there is additionally a slow nonradiative channel (τ_{21}^{-1}).

The key point of a four-level system is that electrons that are pumped from levels

0 and 3, will quickly decay to level 2, leading to an inversion density of level 2 over level 1, which is available for stimulated emission. In general this would allow the optical pumping between levels 0 and 3 to generate inversion between levels 1 and 2. However in this study, rather than optically pumping, a constant electrical pump rate r_p^0 is used. This is done so that the emitted fields, which are tuned to the stopped light point take the main focus.

Four-level systems are incorporated into FDTD using the time-domain differential equation for the polarisation given in Eq. 2.25,

$$\frac{\partial^2 \mathbf{P}_e}{\partial t^2} + \gamma_e \frac{\partial \mathbf{P}_e}{\partial t} + \omega_e^2 \mathbf{P}_e = \omega_{pe}^2 \varepsilon_0 \mathbf{E}, \quad (3.19)$$

Here the polarisation has been split off into a part \mathbf{P}_e that is connected with the radiative resonances, it is added to the total polarisation when entering into the electric field update equations as discussed in Sec. 2.4. The corresponding level occupation densities update with the auxiliary equations [90],

$$\frac{\partial N_3}{\partial t} = r_p^0 N_0 - \frac{N_3}{\tau_{32}} \quad (3.20.a)$$

$$\frac{\partial N_2}{\partial t} = \frac{N_3}{\tau_{32}} + \frac{1}{\hbar \omega_e} \left(\frac{\partial \mathbf{P}_e}{\partial t} + \frac{\gamma_e}{2} \mathbf{P}_e \right) \cdot \mathbf{E} - \frac{N_2}{\tau_{21}} \quad (3.20.b)$$

$$\frac{\partial N_1}{\partial t} = \frac{N_2}{\tau_{21}} - \frac{1}{\hbar \omega_e} \left(\frac{\partial \mathbf{P}_e}{\partial t} + \frac{\gamma_e}{2} \mathbf{P}_e \right) \cdot \mathbf{E} - \frac{N_1}{\tau_{10}} \quad (3.20.c)$$

$$\frac{\partial N_0}{\partial t} = \frac{N_1}{\tau_{10}} - r_p^0 N_0. \quad (3.20.d)$$

Amplified spontaneous emission (ASE) can be added to this semiclassical description by including spatially resolved Langevin noise to the system, which accounts for the dissipative reservoirs feeding back stochastically on the system. The noise couples to the four-level system and induces incoherent transitions, which then become amplified, allowing for the triggering of the lasing regime [91].

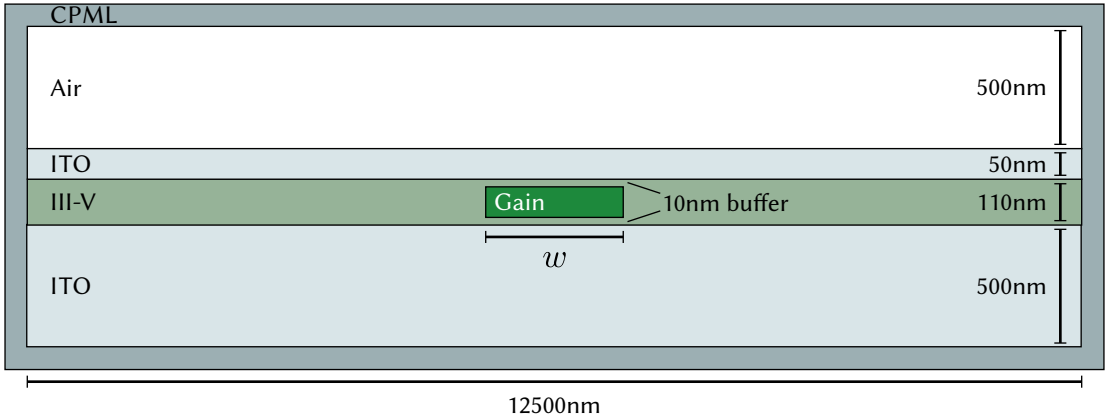


Figure 3.7: Schematic of the FDTD setup.

The layered structure described in the frequency domain analysis is truncated to fit in a simulation domain surrounded by CPML layers. The pumped gain region is placed in the horizontal centre of the simulation, and extends a width w ; vertically it takes up the height of the III-V layer that it is embedded in up-to a 10 nm buffer on either side.

3.6.2. Lasing Dynamics

In this section, the results of and discussions on FDTD simulations are presented. For computational tractability, the simulations presented here are 2D with uniformity in the y direction. The layered geometry of Fig. 3.4 is recreated in these simulations, with the top and bottom layers (that were unbounded in the analytic study) having a height of 500 nm, and the entire structure having a width of 12500 nm. The simulation domain is surrounded with *convolutional perfectly matched layers* (CPML) layers, which quickly attenuate incident fields without introducing reflection such that they do not interact with the simulation boundary [92]. The dielectric layer has a four-level system embedded in it within a region of width w that varies per simulation in the range $w \in [200, 1500]$ nm, and a height that is the same height as the host layer with a 10 nm buffer on either side to simulate quenching by the metal layer. This is depicted in Fig. 3.7 with further simulation parameters that match the frequency

domain analysis as given in Tab. 3.1.

The first set of simulations examines the general dynamics of emitting into a stopped light structure. For a gain region width of 1500 nm, two sets of simulations are run; the first with the stopped light structure as described, and the second with a control structure where the top metal layer has been reduced in thickness to 20 nm with the effect of removing the stopped light points whilst keeping a TM_1 mode that is in the same frequency range. In both cases the gain density is varied in a range of $N \in [0.0005, 0.004] \text{ nm}^{-3}$.

Of the simulations, the the SL structure with gain densities above $N = 0.0015 \text{ nm}^{-3}$ enters a steady state lasing regime after times that vary between 0.3 ps and 0.6 ps. Simulations below this density range did not enter into a lasing regime, whereas there were bursts of ASE, fields never grew strong enough to lead to sustained lasing. The control structure also can also enter the lasing regime, albeit requiring more than double the gain density at $N = 0.0035 \text{ nm}^{-3}$

Figure 3.8.a-c plots the mean inversion and energy density of a point in the centre of the emitter region. For the cases in the SL structure that did enter a lasing regime, characteristic relaxation oscillations can be seen where inversion initially builds up and spontaneous emission events are induced. The fields then are amplified as they stimulate further emission, growing the field in the mode coherently. From here the emitted fields start to grow exponentially, and when they are of sufficient strength will deplete the inversion density. This reduction of inversion feeds back by decreasing the available gain, leading to a decrease in field energy as the energy in the field is lost to dissipative processes in the metal layers. The decrease in energy density allows for the inversion to rebuild. This continues in an oscillatory manner with the energy density lagging behind the inversion by 90° . The amplitude of the inversion and energy oscillations decrease with each cycle until a stable steady value for both

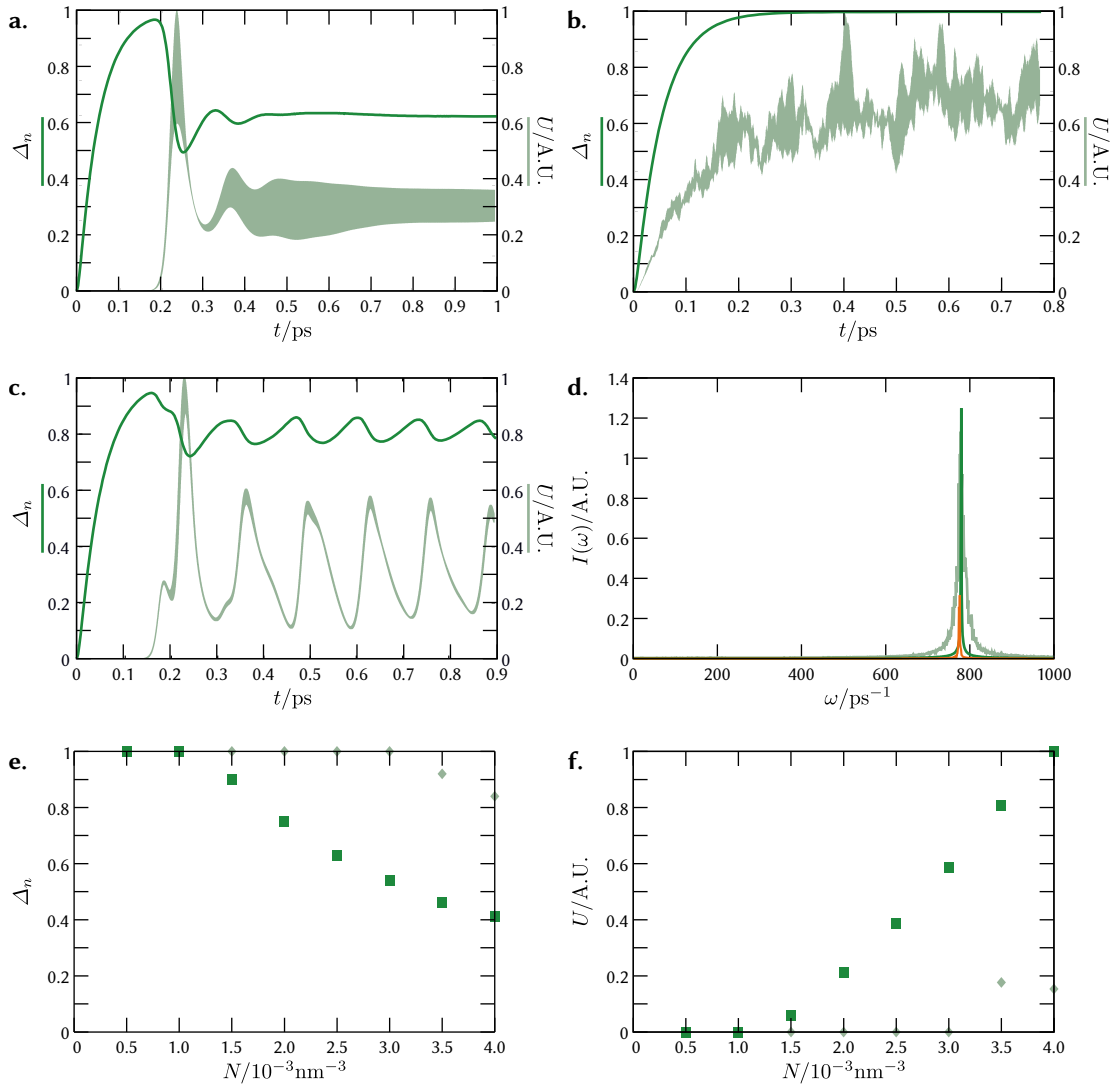


Figure 3.8: Lasing onset with increasing gain density.

- a, b, c. Energy density and mean inversion for a. the stopped light structure with a gain density $N = 0.002 \text{ nm}^{-3}$, b. the stopped light structure with a gain density $N = 0.001 \text{ nm}^{-3}$, c. the control structure with a gain density $N = 0.004 \text{ nm}^{-3}$.
- d. Power spectra for sl structure at $N = 0.002 \text{ nm}^{-3}$ (deep green), sl structure at $N = 0.001 \text{ nm}^{-3}$ ($\times 5000$ pale green), and control structure at $N = 0.004 \text{ nm}^{-3}$ (orange).
- e. Steady state inversion of sl (deep green) and control (pale green) structures with varying gain density.
- f. Steady state cycle averaged energy density with varying gain density.

is reached. In contrast, the control structure, albeit entering a regime of relaxation oscillations, is more erratic and the oscillations do not settle to a steady state. Instead the oscillations continue with a factor of 4 between the peak energy density and the trough.

Relaxation oscillations are accompanied by a characteristic decrease of the width of the power spectrum, from a wide peak in ASE, to a sharp one in the lasing regime. This observation, which is usually taken as crucial evidence for lasing in experimental setups, is displayed in Fig. 3.8.d.

For the SL structure, the inversion density ($N_2 - N_1$) needed for lasing is 0.00148 nm^{-3} . If the total density of gain molecules is less than this, then the system cannot enter a lasing regime, only able to support occasional bursts of ASE. Once the lasing threshold has been passed, the energy density in the mode increases linearly with the gain density.

3.6.3. Lasing Mode

In this section, the lasing modes are investigated for SL structures where the width of the gain region varies in the range $w \in [200, 1500] \text{ nm}$, using a fixed gain density of $N = 0.002 \text{ nm}^{-3}$.

The spatially resolved, cycle averaged Poynting vector, energy density, and inversion are plotted in Fig. 3.9 for a structure with width 1000 nm. The energy is concentrated on metal-dielectric interfaces, strongest on the lower interface, and is localised around the gain medium despite there being no cavity along the horizontal direction.

The Poynting vector shows how energy circulates in the structure. There are four energy flux vortices, one in each corner of the structure, as described in the figure caption, these have energy move out of the gain region into the metal layers and into it in dielectric layers. Considering the x component of the Poynting flux, (Fig. 3.9.a), the

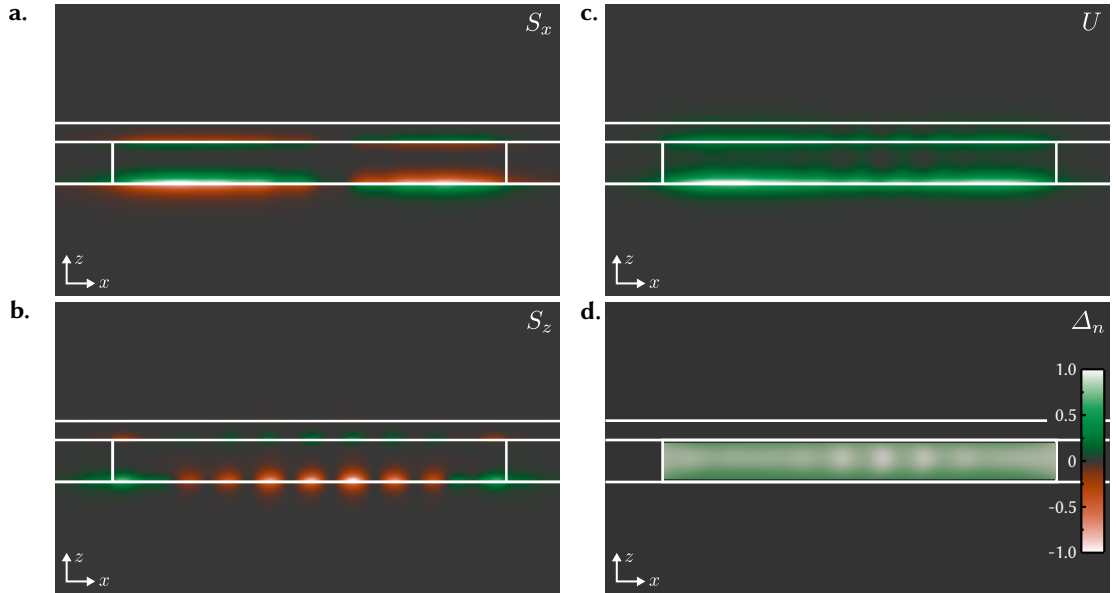


Figure 3.9: Energy flux and density of lasing mode.

The lasing mode of a SL structure with a width 1000 nm. a. and b. show the x and z component of the cycle-averaged Poynting vector respectively, with positive values in green, and negative in orange. Focusing on the bottom right lobe of the flux in a, energy flows into the gain region in the dielectric layers and out of it in the metal layer. For the same lobe in b, energy moves downwards out of the gain region towards the centre, and upwards into the region at the edge. The counter-clockwise energy vortex in this corner is mirrored in the other corners.

The cycle-averaged energy density is plotted in c. and inversion in d. The inversion is the complement of the energy density, being highest in areas with low energy density, and depleted where the mode sits.

forward and backward flows are in exact balance. The balanced counter-propagation of energy in the negative-permittivity (metal) layers against the dielectric layer. This is the basis of feedback in the system.

The inversion is shown in Fig. 3.9.d, there are areas of spatial hole burning where the energy density is highest. The spatial modulation seen is explained when considering the field profile and its formation.

It is important to note that the modes that are formed when the structure enters the lasing regime are a dynamic synthesis of the spectrum of planewave modes available rather than that of a predefined cavity mode. The modes that form are propagating waves, with an advancing phase, rather than purely standing waves, as shown in Fig. 3.10. It will be shown that this results from modes being centred independently on finite positive and negative q points, the relative excitation of each competing with each other, rather than having symmetric excitation at $q = 0$. This is in contrast even to the stopped light lasing structure considered in Ref. [86], which was photonic in nature rather than plasmonic, and emitted symmetrically about $q = 0$ as a standing wave.

In all cases, the modes are inwardly propagating, that is the leftmost half propagates right and vice versa. These two halves form a standing wave where they meet, and this node need not be in the centre of the structure, instead being randomly chosen by the spontaneous symmetry breaking at the transition from ASE to lasing. The asymmetry of the mode profile will be discussed later in the chapter.

Lasing is shown to be possible for structures with a gain region width down to 200 nm, at which point the steady state inversion rises to around 0.9. For this case one observes a standing wave in the gain interior, i.e. a symmetric excitation of positive and negative q modes. The confinement of such a structure is at its limit here, with significant field profile outside the gain region. For widths smaller than this, there

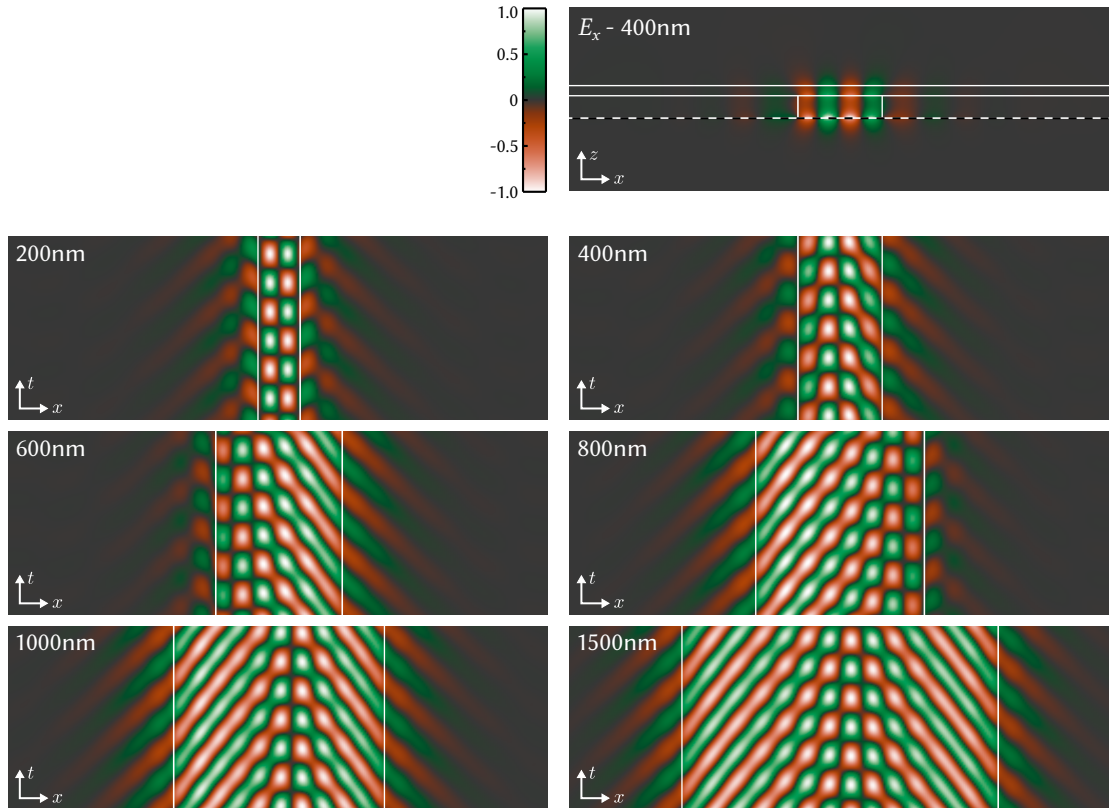


Figure 3.10: Field evolution in steady state.

The E_x field along a line slice at the bottom metal interface is plotted against time on the vertical axis. For the 200 nm structure, the field inside the gain region is a standing wave. The other structures have two inward propagating waves which meet at a standing node. This node can appear towards the edges, i.e. for 600 and 800 nm, or positioned towards the centre for 1000 and 1500 nm. A stream of plasmons is emitted at either side of the gain region, with a predominantly negative phase velocity.

will not be enough gain to pass the lasing threshold. This thinnest confinement at 200 nm is $12\times$ the free-space wavelength, and indeed $3.5\times$ the bulk wavelength in the semiconductor layer.

Outside of the gain region, a stream of plasmons is emitted to either side with a negative phase velocity. For these plasmons, it makes sense to use a complex-wavevector picture to describe them, as we have a steady state oscillating source, for which the field is known at a fixed point in space (the edges of the gain region), for which we wish to consider the spatial evolution away from this point.

One can analyse the spectral content of the fields, once the system has entered into a steady state. Using *discrete Fourier transform* (FFT) methods, the peak frequency component, ω_{peak} , of the electric field is identified and isolated. This returns a spatially resolved, complex valued function $\tilde{\mathbf{E}}(\mathbf{x}, \omega_{\text{peak}})$. Taking a spatial Fourier transform along the waveguide (x) axis, allows the extraction of the spatial power spectrum, which is averaged over z positions within the gain layer, $I(q) = |\tilde{\mathbf{E}}(q, \omega_{\text{peak}})|^2$.

The wavevector of the emitted plasmon can be extracted by taking the FFT over positions outside of the emitting gain region. Figure 3.11 shows the spectrum of fields emitted from the right terminal, i.e. integrating from the edge of the gain region up to but excluding the CPML layer. These data are fit to the first four analytically determined complex-wavevector modes (see Fig. 3.4) at the lasing frequency. The wavefunction of such modes is the Fourier transform of a complex decaying exponential,

$$\varphi(x) = \theta(x) \exp(i \operatorname{Re} \beta_i x) \exp(-\operatorname{Im} \beta_i x) \quad (3.21.a)$$

$$\tilde{\varphi}(q) \propto \frac{1}{q - \beta_i}, \quad (3.21.b)$$

where β_i is the complex wavevector of the bound mode SPP. This is summed over each of the first four plasmons, each with a complex amplitude, then the absolute square

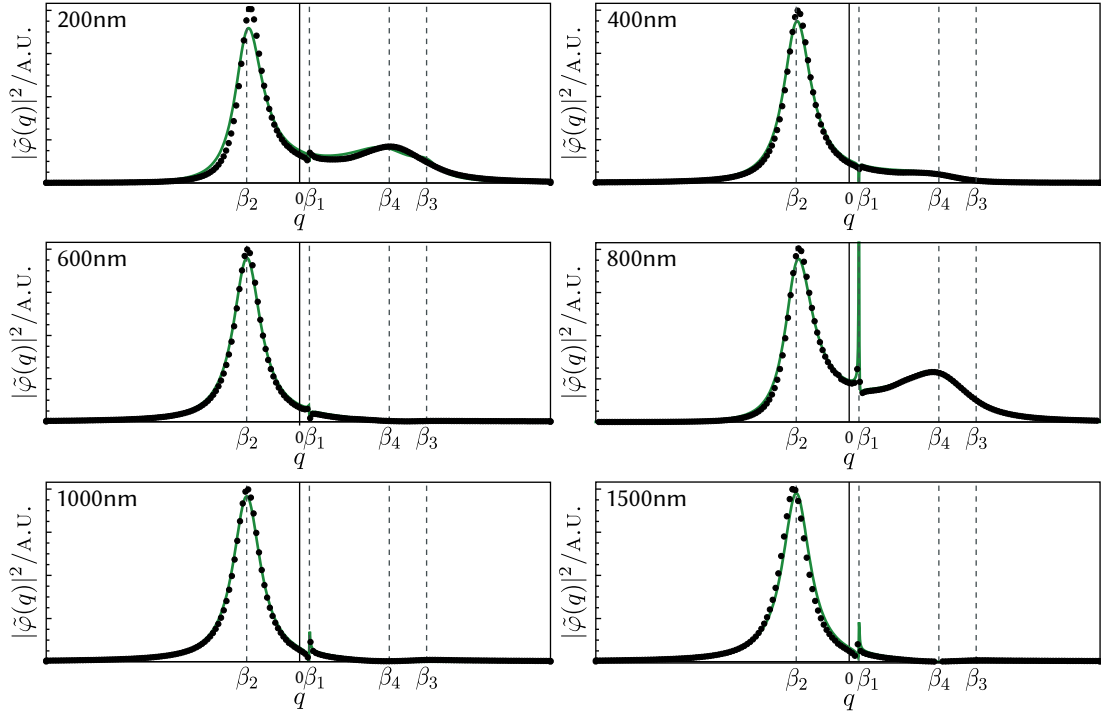


Figure 3.11: Complex wavevector plasmons.

Power spectra of fields emitted from the right terminal of the gain region (black dots). This is fit to the lineshape of the first four cwv plasmons (green line), i.e. a Lorentzian function, $|\tilde{\varphi}(q)|^2 = |\sum_i^4 \varphi_i/(q - \beta_i)|^2$. The amplitudes are varied to fit, but the wavevectors are fixed from the cwv plasmon dispersion at the lasing frequency (See Tab. 3.2). The imaginary part becoming the width in the spectral density. In each, the negative phase velocity β_2 plasmon is strongest, with β_4 having a large amplitude for 200 nm and 800 nm which can be also seen in the field profiles of Fig. 3.10.

of this is compared with the data, i.e.

$$|\varphi(q)|^2 = \left| \sum_{i=1}^4 \frac{\varphi_i}{q - \beta_i} \right|^2. \quad (3.22)$$

The fit allows the amplitude of each resonance to change, but keeps the wavevectors constant. Excellent agreement is found, confirming the presence and applicability of the description of complex-wavevector plasmons.

The negative group velocity plasmon β_2 , has the strongest amplitude in all cases, though the narrow width β_1 plasmon is present too. In cases where the standing wave node is close to the terminal, i.e. for $w = 200, 400, 800$ nm there is significant excitation of the short propagation length β_4 plasmon.

Thus, stopped light lasing can be utilised as a source of coherent plasmons at a single frequency and discrete wavevector. Alternatively by adding a grating to the structure away from the gain region, the plasmons may be outcoupled, converting this into a photonic SL laser.

The spatial power spectrum, $I(q)$, can also be taken over the entire domain, rather than in the interval to the right of the gain region, in order to capture the profile of the lasing mode. This function is not symmetric about $q = 0$ since it was transformed from a complex valued function. Hence it does not follow the usual evenness properties of the Fourier transform of a real function. This allows for inspection of how the positive and negative wavevector (and hence phase velocity) modes are independently excited. Figure 3.12c plots the power spectra of lasing modes in the range of gain widths considered. It can be seen that in each case, the power spectrum is a bimodal distribution with peaks about $q \approx \pm 30.7 \mu\text{m}^{-1}$, which is exactly the wavevector of the second stopped light point. As one would expect, the width of each peak is inversely proportional to the gain width chosen, e.g. the smallest gain section at 200 nm, the width is around $5 \mu\text{m}^{-1}$. There is no preferential excitation of the peaks, and seemingly no correlation between their relative amplitude. This is because they

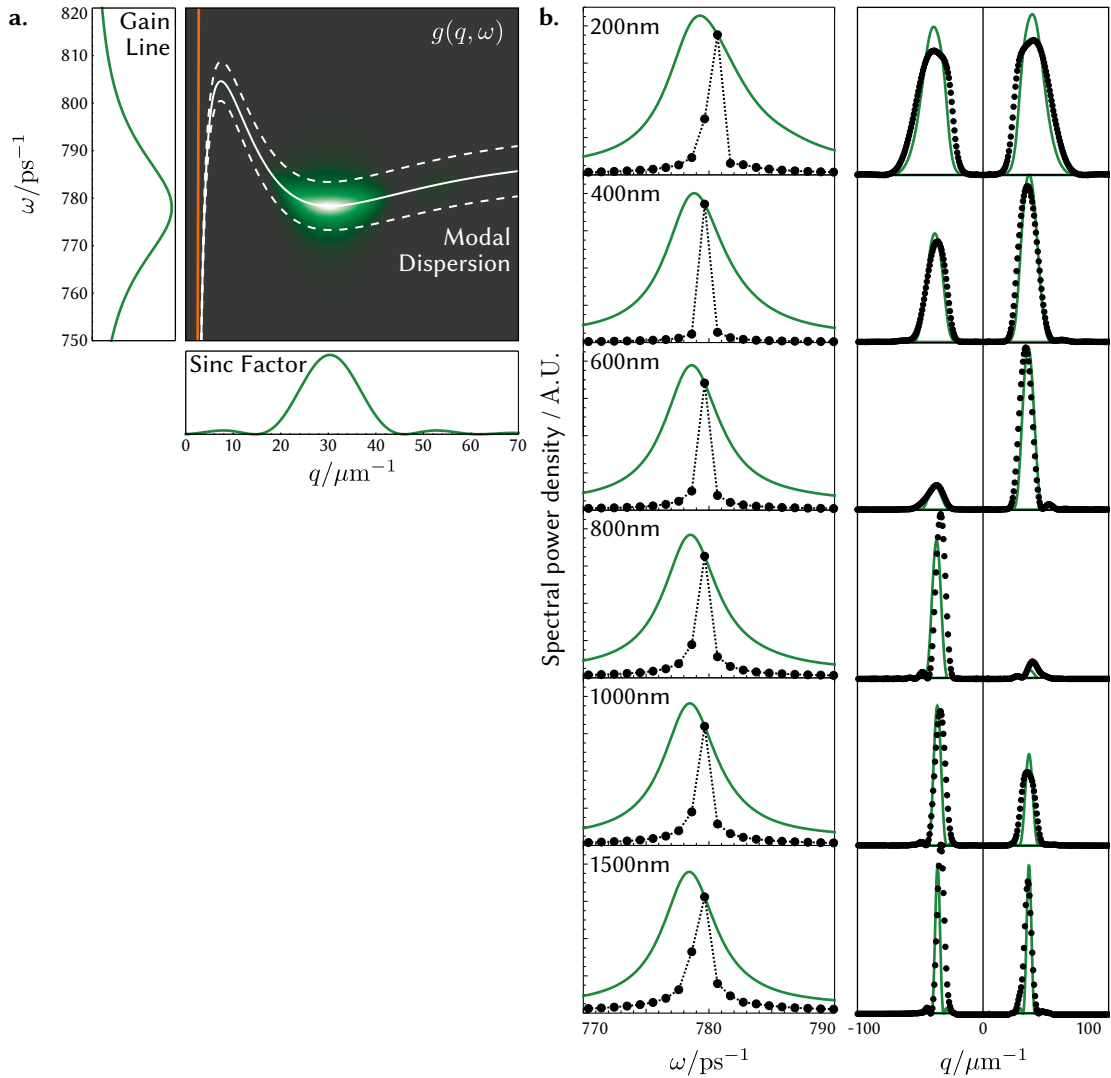


Figure 3.12: Power spectrum of lasing modes.

- a. Coupling strength $g(q, \omega)$, which is composed of the emission lineshape (left), the *sinc* function of the gain region (bottom), and the mode support (overlaid). The frequency which maximises the the integral of g over wavevector is *picked* by the system to lase at.
- b. temporal and spatial power spectrum of the lasing mode for model (green lines) and FDTD data (black points). The spatial mode profile is modelled by a modified form of the coupling strength at the lasing frequency, as given by Eq. 3.24. Results are in excellent agreement with the FDTD results.

are two competing modes, one of which will initially take the lead in growth due to the spontaneous symmetry breaking of amplified spontaneous emission. The first mode will dominate the gain, being able to exponentially grow in field strength. The second mode may still be allowed to grow but spatially separated from the first, harvesting areas where the field and gain are less strongly coupled. This picture is corroborated when viewing the time evolution of the steady state fields, which show two lobes, inward propagating, with a finite overlap width where the wave becomes standing, this is depicted in Fig. 3.10. This is developed further in Ref. [93], where it is shown how the location of the nodes move on longer time scales.

It is possible to predict the spectral content of the lasing mode. Plasmons are emitted into the frequency which maximises the effective gain,

$$G(\omega) = \int_{-\infty}^{\infty} dq g(q, \omega) \quad (3.23.a)$$

$$g(q, \omega) = \frac{\gamma_L/\pi}{(\omega - \omega_L)^2 + \gamma_L^2} \frac{\gamma_{pl}(q)/\pi}{(\omega - \omega_{pl}(q))^2 + \gamma_{pl}(q)^2} \text{sinc}^2 \left(\frac{w(q - q_2)}{2} \right). \quad (3.23.b)$$

This expression is the product of three terms; firstly, there is the emission lineshape of the gain medium, this is multiplied by the density of states of bound modes that are available to emit into. The final part is a geometrical factor, that is the square of the Fourier transform of a “tophat” function of width w , which represents the width of the gain area. There can be modulation of the emitted field in the gain region, so the sinc is allowed to be translated in q -space, and will centre itself at the zgv 2 point q_2 . Figure 3.12 shows the frequencies that maximise the effective gain and the frequency range that was emitted at in the simulations. This is presented alongside a the coupling strength $g(q, \omega)$ for a 400 nm gain section. This frequency of highest gain can then further be used to predict the mode shape $I(q)$, up to a factor of the weights of the mode in the $+q$ and $-q$ excitation (I^+, I^-), by a slight modification of

$g(q, \omega)$, to include both excitations,

$$I(q) \propto \frac{\gamma_{\text{pl}}(q)}{(\omega - \omega_{\text{pl}}(q))^2 + \gamma_{\text{pl}}(q)^2} \left(I^+ \text{sinc} \left(\frac{w(q - q_2)}{2} \right) + I^- \text{sinc} \left(\frac{w(q + q_2)}{2} \right) \right)^2, \quad (3.24)$$

which is in excellent agreement with the FDTD spectra.

3.7. Conclusions

This chapter has introduced *plasmonic stopped light lasing*, whereby plasmons are localised by reducing the group velocity of a wavepacket to zero whilst within a gain medium. This is in contrast to traditional nanolasing schemes, which localise energy in a resonant cavity.

In order to explain the concept, topics of dispersion, and the nuances of the complex-frequency/complex-wavevector pictures have been discussed. Frequency domain methods have been employed alongside an evolutionary optimisation algorithm in order to characterise the properties and quality of a structure and select for optimal structures within constraints.

An exemplary structure was introduced, composed of realistic materials, whose properties were studied throughout the rest of the chapter. Analysis in frequency domain was continued to investigate how, in the small signal gain regime, a two-level emitting resonator could compensate for the inherent material losses in metal layers, determining idealised threshold values of inversion required to free a mode of damping.

Equipped with this analysis, finite difference time domain simulations were made of the test structure, in order to capture the dynamics of spatial and nonlinear effects. The previous frequency domain analysis of the threshold inversion was corroborated by varying the gain density in each time domain simulation, and it was found that

lasing is indeed possible in this scheme.

The lasing mode was investigated, and a model for predicting its modal content proposed. It was found that the feedback provided from stopped light lasing ultimately derives from a dynamically formed vortex of power flow, with propagation and counter-propagation balancing between the dielectric and metal layers. Despite being stopped, the lasing mode carries a finite phase velocity, with an inward propagating phase modulation that can be detected from the top of the structure.

As an output of the lasing process, coherent plasmon polaritons (sitting on the cusp of the complex-wavevector dispersion curve) are emitted from the sides of the gain region.

This is a new type of subwavelength laser, where the active component is smaller than a few hundred nanometres, and coherently emits plasmons directly into a waveguide without relying on external coupling mechanisms. The dynamic formation of the cavity-free lasing mode is a new physical feature, the implications of which are open. It could become the basis for single frequency coherent SPP generation in quantum plasmonic applications [10, 11], or as the basis of a quantum fluid such as a photonic Bose-Einstein Condensate [94].

Symbol	Parameter	Value
ε_∞	Drude high frequency permittivity	4.0
ω_p	Drude plasma frequency	3130 ps ⁻¹
γ_p	Drude loss	10.7 ps ⁻¹
ε_{bg}	Background permittivity	11.68
ω_e	Emission frequency	778 ps ⁻¹
γ_e	Emission width	31.7 ps ⁻¹
σ_e	Emission cross section	2.12×10^{-7} μm ²
N	Carrier density	2×10^6 μm ⁻³
τ_{10}^{-1}	Non-radiative decay rate (0→1)	10 ps ⁻¹
τ_{21}^{-1}	Non-radiative decay rate (1→2)	0.002 ps ⁻¹
τ_{32}^{-1}	Non-radiative decay rate (2→3)	10 ps ⁻¹
r_p^0	Electrical pump rate (0→3)	1 ps ⁻¹

Table 3.1: Simulation parameters.

Parameters for frequency domain and FDTD simulations, divided into: metal Drude model, emitter Drude-Lorentz parameters, FDTD four-level system parameters.

Symbol	Parameter	Value
d_1	III-V layer thickness	0.110 μm
d_1	I TO layer thickness	0.050 μm
q_1	ZGV 1 wavevector	7.41 μm^{-1}
ω_1	ZGV 1 frequency	$805 + i 4.14 \text{ ps}^{-1}$
q_2	ZGV 2 wavevector	30.3 μm^{-1}
ω_2	ZGV 2 frequency	$778 + i 5.06 \text{ ps}^{-1}$
Δ_q	wavevector bandwidth	22.9 μm^{-1}
Δ_ω	frequency bandwidth	26.3 ps^{-1}
v_b	band velocity	$1/262 c$
β_1	cwv mode 1	$3.94 + i 0.131 \mu\text{m}^{-1}$
β_2	cwv mode 2	$-21.3 + i 6.71 \mu\text{m}^{-1}$
β_3	cwv mode 3	$51.2 + i 6.53 \mu\text{m}^{-1}$
β_4	cwv mode 4	$36.1 + i 16.1 \mu\text{m}^{-1}$
	cwv frequency	778 ps^{-1}

Table 3.2: Properties of optimised SL structure.

Divided into: Thicknesses of material layers, coordinates of zgv points in the dispersion relation, band metrics, complex wavevector modes at the FDTD emission frequency.

Chapter 4.

Active Plasmons in Nonequilibrium Graphene

4.1. Introduction

Graphene has gained widespread scientific interest since 2004 [95, 96, 97, 98, 99] when it was shown that it could be experimentally produced by exfoliating a single layer from graphite [22]. It is a 2D crystal of carbon, where the atoms are arranged in a flat hexagonal tiling, with σ -bonds binding each atom to its three nearest neighbours. Each atom has a remaining $2p_z$ orbital which contributes to the bonding by overlapping with its nearest neighbours forming a half-filled π -band [100]. The π -band can be modelled in a tight-binding formalism, which transforms orbitals of electrons sitting at one of the atomic sites, a or b, into energy eigenstate planewaves in the conduction and valence band. The tight binding band structure is shown in Fig. 4.1 about the K symmetry point, alongside diagrams of the lattice in real and reciprocal space. About this point, the dispersion relation of electrons is linear and the two bands meet with a vanishing energy gap, forming what is known as the *Dirac cone* since the

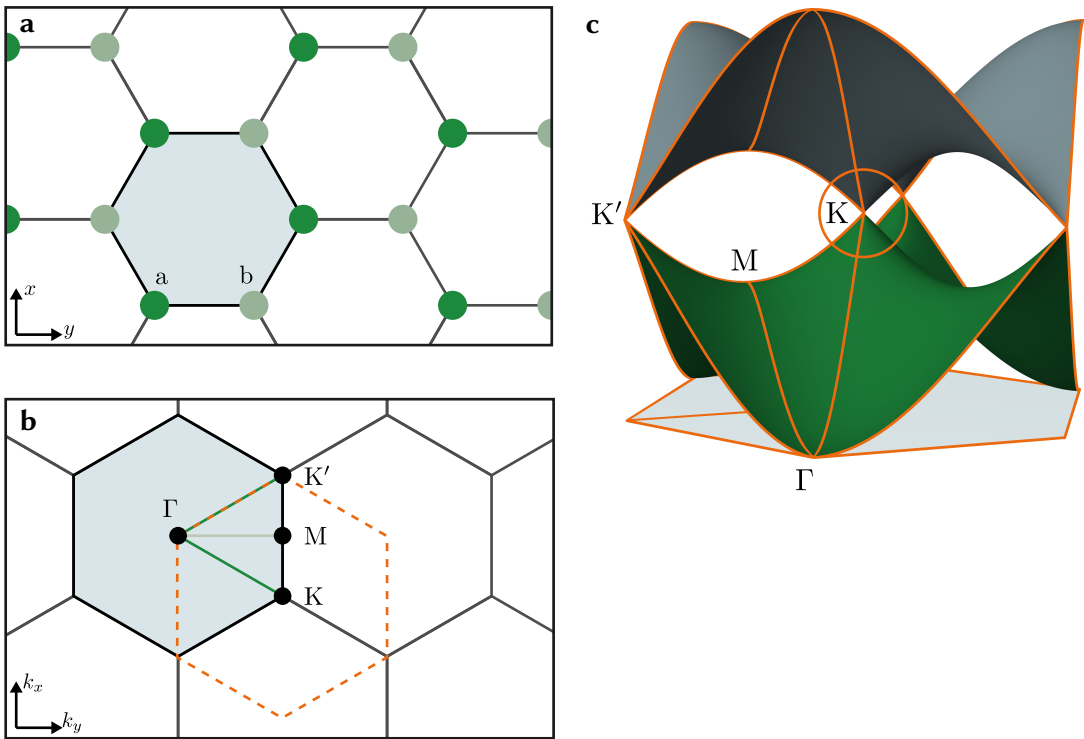


Figure 4.1: Graphene structure and tight binding model.

- a. Graphene's molecular structure, composed of two overlapping triangular sublattices of a and b sites. The hexagonal unit cell is shaded.
- b. Reciprocal space lattice, marking points of high symmetry (Γ , M, K, K'). The 1st Brillouin zone is shaded, and the Wigner-Seitz cell about the K point is highlighted.
- c. Tight binding electron dispersion about the K point. The fully occupied valence band is shown in green, and empty conduction band in black. The dispersion relation is conical in the immediate vicinity of the K point (and equivalently about the K' point).

electrons that sit there may be described by a relativistic Dirac equation. The equation describes massless particles with a “speed of light” given by the Fermi-velocity $v_F \approx c/300$ lending them the name *massless Dirac fermions* (MDFs).

It is graphene’s properties as a 2D metallic material with a linear dispersion and zero bandgap that give it remarkable electronic and optical properties [101, 102, 100, 103, 104]. It also allows for a strong optical interaction with the MDF plasma in both a linear [105, 106, 107, 108] and nonlinear regime [109, 110, 111, 112]. Though perhaps one of graphene’s most useful properties is its tunability; the Fermi-level of graphene can be set by chemical doping or a gate voltage [113, 114, 115, 116]. Coupled with a conical dispersion up to energies of ~ 1 eV, this allows broadband optical operation in the visible and infrared. This has been exploited for the construction of nanoscale devices such as photodetectors [117, 118, 119], modulators [120], saturable absorbers [121], metamaterial devices [122, 123, 124], and for use in sensing applications [125, 126].

The aspect of graphene that will be primarily focused on in this thesis is its ability to support plasmons [127, 128, 116, 129, 130, 131, 132, 133, 134]. The coupling of these charge density waves to the electromagnetic field allows for confinements that are on the order of 1/100 of the free-space wavelength [135, 128]. Plasmons appear as the poles of the Coulomb potential, calculated from the dynamic polarisation in the *random phase approximation* (RPA) [136, 137].

Despite having a high conductance, plasmons on doped graphene have high losses resulting in propagation lengths that are typically smaller than the wavelength [138]. This is due to Landau damping; the generation of electron hole pairs by the absorption of plasmons, as well as collisional damping channels [139, 131]. Much like in metal plasmonics, graphene’s utility as a plasmonic platform will rely on being able to mitigate these losses.

The semimetal properties can be utilised to this end. Exciting graphene with a

short optical pulse will generate hot electron/hole pairs. These carriers quickly relax via intraband processes within their respective band but are subject to a bottleneck for interband recombination processes which leads to the formation of a quasiequilibrium of inverted carriers yielding optical gain [140, 141, 142]. This gain is also available to plasmons which may be amplified by stimulated emission [143, 144, 145, 146] enhanced by the tight confinement of plasmons on the graphene sheet.

The balance of absorption and emission rates in graphene, and hence the presence of net gain, is critically dependent on the exact form of the plasmon dispersion relation. Previous studies have considered this in approximative form, rather than as the exact complex solution to the RPA polarisability. It therefore remains to be seen whether under conditions of inversion, finite temperature, collision loss, and doping, plasmons indeed exist and can become undamped.

Stimulated emission in a system is always accompanied by spontaneous emission where carrier pairs spontaneously recombine emitting broadband incoherent photons [147] and plasmons. The enhanced field of the plasmon modes and low group velocity gives rise to a high density of optical states, thereby accelerating the spontaneous emission rate from an equivalent dipole transition in free space [148].

From the point of view of the carrier system, spontaneous recombination by plasmon emission represents an ultrafast relaxation channel [149, 150, 144] that may indeed play a primary role in the dynamics of hot carrier relaxation [151, 152, 153, 154, 155, 156, 157]. This is a process that has often been attributed to *Auger recombination* (AR) [158, 159], part of a family of Auger processes, which are two-body Coulombic carrier-carrier scattering processes that include AR, impact ionisation, inter- and intraband scattering [156]. The particular role of this channel however is subject to discussion, as the collinear Auger processes are suppressed when considering dynamic screening in RPA [156, 160].

The timescales for carrier recombination emitting plasmons have been reported to vary between 10 fs and 100 ps in first theoretical studies [149, 150] therefore accurate determination of the timescales is key to establish the primacy of plasmons as a channel for inversion decay.

Experimentally, the relaxation of hot carriers has been observed in *time resolved, angle resolved photo-emission spectroscopy* (TR-ARPES) [149, 161, 162, 163, 164], and pump-probe setups [165, 166, 167, 159, 155, 141, 168, 169], and has shown thermalisation within the bands at a timescale of 10 fs and interband recombination decaying the inversion over ~ 100 fs.

Whereas the polarisability, and derived plasmons, have been studied extensively in the case of a thermal equilibrium of doped Graphene [170, 136, 137, 171, 172, 173, 174, 175, 176, 177, 178], there has so far not been a general formalism for calculating complex valued polarisabilities for nonequilibrium carrier distributions.

4.1.1. Organisation of chapter

This chapter will start in Sec. 4.2 by introducing the zero-temperature equilibrium polarisability of graphene, which will provide the basis in later sections for more generalised polarisabilities. The complex frequency plasmon dispersion will be presented, which exactly solves the RPA dielectric function, and compared to approximate schemes.

Next in Sec. 4.3, a method to generalise the plasmon dispersion to arbitrary isotropic carrier distributions will be derived. This will be assisted by the introduction of scale-free variables, which sets all quantities relative to the tunable Fermi-level.

The quasiequilibrium polarisability will be presented in Sec. 4.4 which describes photoinverted carriers that have thermalised within their respective bands. The plasmon dispersion of photoinverted graphene is calculated from the new polarisability

expression, for both intrinsic and doped graphene, showing that plasmons with gain are indeed possible in an idealised case.

Improvements are made to the model in Sec. 4.5, to include the effects of collision loss and finite temperature, which will both reduce the gain available to plasmons. The calculation for temperature presented in this section works for low temperatures, but will be shown to break down as T increases. This will be remedied in Sec. 4.6, where it is explicitly shown how to calculate the polarisability for arbitrary carrier distributions using a contour integral method. This allows for the evaluation of polarisabilities with high temperature Fermi distributions, but also that of a non-Fermi distribution of hot photoexcited graphene.

Section 4.7 calculates the spontaneous emission of photoinverted graphene, and the associated carrier recombination rates. This is done exactly at zero temperature, and with a Fermi's golden rule scheme for cases of collision loss and finite temperature, with an accuracy that is dependant on using the exact complex frequency plasmon dispersion.

Finally in Sec. 4.8, the inversion decay dynamics of the carrier system are considered with nonequilibrium plasmons emission as the channel for spontaneous recombination.

4.2. Plasmon Modes of Equilibrium Graphene

In a similar manner to the surface of a metal, 2D materials endowed with charge carriers, such as graphene, may support surface plasmon modes. One of the main differences though notes is that there is no bulk medium unlike for metal plasmons, and the charges are entirely confined to the 2D sheet. This means that the presence of modes relies solely on the characteristic of the surface conductivity σ_s , rather than the bulk properties of a conducting substrate.

Graphene, in contrast to metals, supports two types of collective plasmon excitations, labelled by their electromagnetic field configuration; the transverse magnetic (TM) modes that are associated with the longitudinal density-density response of the MDF plasma [136, 179, 180, 181, 178], and have similar field characteristics as their metal counterpart; and transverse electric (TE) modes associated with the transverse current-current response and have no metal counterpart. TE plasmons only exist in a limited frequency range and are weakly bound [178], as such, only the TM plasmons are considered in this thesis as they are strongly coupled to the MDF plasma [182, 183].

The dispersion relation of the TM mode can be solved using the transfer matrix method formalism of Sec. 2.3. Assuming a conducting sheet sandwiched between two (isotropic, non-magnetic) semi-infinite half-spaces, the transfer matrix is,

$$\mathcal{M} = \mathbf{U}_{\text{sup}}^{-1} \mathbf{S} \mathbf{U}_{\text{sub}} , \quad (4.1.a)$$

or in full,

$$\mathcal{M} = \frac{1}{2} \begin{pmatrix} 1 & Z_{\text{sup}} \\ 1 & -Z_{\text{sup}} \end{pmatrix} \begin{pmatrix} 1 & 0 \\ -Z_0\sigma_s & 1 \end{pmatrix} \begin{pmatrix} 1 & 1 \\ 1/Z_{\text{sub}} & 1/Z_{\text{sub}} \end{pmatrix} , \quad (4.1.b)$$

yielding the condition for the presence of bound modes as,

$$\frac{1}{Z_{\text{sub}}} + \frac{1}{Z_{\text{sup}}} + Z_0\sigma_s = 0 \quad (4.2)$$

which, for TM modes is,

$$\frac{\varepsilon_{\text{sub}}}{\sqrt{q^2 - \varepsilon_{\text{sub}}(\omega/c)^2}} + \frac{\varepsilon_{\text{sup}}}{\sqrt{q^2 - \varepsilon_{\text{sup}}(\omega/c)^2}} + \frac{ic}{\omega} Z_0\sigma_s = 0 . \quad (4.3)$$

Neglecting wave retardation, i.e. $q \gg \omega/c$, and by defining $\bar{\varepsilon} = (\varepsilon_{\text{sub}} + \varepsilon_{\text{sup}})/2$, one may cast this into a simplified form [184, 171, 175],

$$1 + \frac{iq}{2\bar{\varepsilon}\varepsilon_0\omega}\sigma_s(\mathbf{q}, \omega) = 0 , \quad (4.4)$$

here $\sigma_s(\mathbf{q}, \omega)$ is the nonlocal sheet conductivity, i.e. the linear electronic response to a monochromatic electromagnetic planewave.

Equation 4.4 will have solutions for a conductivity with positive imaginary part. The particular functional form of the conductivity will determine the characteristics of the plasmon solutions.

The plasmon may also be solved for in linear response theory of collective charge oscillations of a 2D electron gas [185]. In the *random phase approximation* (RPA), the plasmon dispersion is determined from the roots of the dielectric function [186, 187],

$$\varepsilon_{\text{RPA}} := 1 - V_q \Pi(\mathbf{q}, \omega) = 0 , \quad (4.5)$$

where $V_q = e^2 / 2\bar{\varepsilon}\varepsilon_0 q$ is the bare 2D Coulomb potential in reciprocal space and $\Pi(\mathbf{q}, \omega)$ is the irreducible polarisability, which is the Feynman propagator of electron-hole pairs [188]. Both Π and σ_s represent linear responses, so Eqs. 4.4 and 4.5 can be directly compared giving the relationship between the sheet conductivity and polarisability in RPA as,

$$\sigma_s(\mathbf{q}, \omega) = ie^2\omega/q^2 \Pi(\mathbf{q}, \omega) , \quad (4.6)$$

noting that the RPA has been shown to be surprisingly accurate for graphene [189].

The plasmon dispersion is defined by the zeroes of the dielectric function, which in general is a complex-valued function of complex variables. These zeros may be found for either a real-wavevector/complex-frequency or real-frequency/complex-wavevector, and it is the former that is considered here. That is solutions characterised by a real wavevector eigenvalue, q , with the imaginary part of the frequency representing a decay rate of plasmons over time. The exact solution to this equation, the *complex frequency plasmon dispersion* (CFPD), is sought within this chapter.

4.2.1. Complex Frequency Plasmon Dispersion

A major objective of this work is to characterise the gain and absorption spectra of graphene under a variety of electronic configurations. Plasmons in graphene will couple strongly to the electron-hole plasma, interacting via single-particle excitation processes: spontaneous emission, stimulated emission, and stimulated absorption. The imaginary part of the frequency of the plasmon dispersion encodes the net stimulated absorption/emission rate and therefore to get a handle on this, the CFPD should be solved for exactly within the RPA framework. Previously in the literature, the plasmon dispersion has been solved for in a low-loss approximation for zero temperature equilibrium graphene [136, 137].

The basis for calculations involving the polarisability¹ in RPA is the Lindhard formula [184, 136, 137, 172] given as a functional of the, in general nonequilibrium, electron distribution $n(\epsilon)$,

$$\Pi[n](\mathbf{q}, \omega) = \frac{g}{A} \sum_{s,s'=\pm} \sum_{\mathbf{k}} M_{\mathbf{k},\mathbf{k}+\mathbf{q}}^{ss'} \frac{n(\epsilon_{\mathbf{k}}^s) - n(\epsilon_{\mathbf{k}+\mathbf{q}}^{s'})}{\epsilon_{\mathbf{k}}^s - \epsilon_{\mathbf{k}+\mathbf{q}}^{s'} + \hbar\omega + i \times 0}. \quad (4.7)$$

The polarisability describes the noninteracting (unscreened) response of the MDF plasma to external density perturbations. Contained within is a sum over all possible transitions $(\mathbf{k}, s) \rightarrow (\mathbf{k} + \mathbf{q}, s')$, for each initial and final band $s, s' \in \{+, -\}$, at the given wavevector and frequency for a particular particle/hole distribution $n(\epsilon)$. The sum is weighted by the transition matrix element $M_{\mathbf{k},\mathbf{k}+\mathbf{q}}^{ss'}$, a quantity determined by the tight binding model that encodes the honeycomb geometry of Graphene, with the value, $M_{\mathbf{k},\mathbf{k}+\mathbf{q}}^{ss'} = [1 + ss' \cos(\theta_{\mathbf{k},\mathbf{k}+\mathbf{q}})]/2$ [190]. The Lindhard formula sums over degenerate spin and valley (about K and K' points) transitions, leading to the prefactor $g = 4$. In the MDF approximation, the electronic band dispersion is conical in the near vicinity of the Dirac points, i.e. $\epsilon_{\mathbf{k}}^s = s\hbar v_F |\mathbf{k}|$.

¹ Or strictly speaking, its leading order term.

Closed form and semi-analytical solutions to the Lindhard formula have been presented in the literature for the case of graphene in thermal equilibrium, i.e. for the electronic configuration taking the form of a Fermi-distribution,

$$n(\epsilon) = f(\epsilon - \mu, T) = \frac{1}{1 + \exp((\epsilon - \mu)/k_B T)} . \quad (4.8)$$

In the limit of zero temperatures the Fermi function reduces to a Heaviside step function, $f(\epsilon - \mu, T = 0) = \theta(\mu - \epsilon)$, and solutions to this have been first presented for real valued dynamic variables (\mathbf{q}, ω) in piecewise form in Refs. [136, 137]. Similarly, later temperature semi-analytical form for real variables has been derived [174].

Assuming a real valued wavevector that acts as the modal eigenvalue, the plasmon dispersion can be solved by finding the zeros of the dielectric function Eq. 4.5 for a complex frequency $\varepsilon_{\text{RPA}}(q, \omega_{\text{pl}}(q) - i\gamma_{\text{pl}}(q)) = 0$. The sign convention of γ_{pl} has been chosen such that it represents a decay rate for positive values, and amplification due to stimulated emission when $\gamma_{\text{pl}} < 0$. If the plasmon couples to single particle excitations, giving it a finite lifetime, then the frequency does indeed become complex and the dispersion becomes insoluble with formalisms that are only functions of real variables, i.e. containing Heaviside step functions.

For cases where the loss is small, $\gamma_{\text{pl}} \ll \omega_{\text{pl}}$, a first order approximation is often used to solve for the real part of the frequency using just the real part of the dielectric function,

$$\text{Re } \varepsilon_{\text{RPA}}(\omega_{\text{pl}}, q) \approx 0 , \quad (4.9.a)$$

then the imaginary part is given as² [173, 191, 192],

$$\gamma_{\text{pl}} \approx \text{Im } \varepsilon_{\text{RPA}}(\omega_{\text{pl}}, q) / \left. \text{Re} \frac{\partial \varepsilon_{\text{RPA}}}{\partial \omega} \right|_{\omega=\omega_{\text{pl}}} . \quad (4.9.b)$$

In regimes where $\text{Im } \varepsilon_{\text{RPA}}(\omega_{\text{pl}}, q) = 0$ then the above equations become exact, i.e. $\gamma_{\text{pl}} = 0$, which is the case for quasi-loss-free regimes where there is no Landau damping

² Or equivalently as $\gamma_{\text{pl}} \approx \text{Im } \Pi(\omega_{\text{pl}}, q) / \text{Re} \left. \frac{\partial \Pi}{\partial \omega} \right|_{\omega=\omega_{\text{pl}}}$.

(absorption or emission).

The polarisability becomes singular for $\omega \rightarrow v_F q$, which means that solutions of Eq. 4.9 (for real ω_{pl}) can not cross the Fermi line into the region of intraband excitations as $\Pi(q, \omega_{\text{pl}}(q)) \rightarrow \infty$ and Eq. 4.5 can never hold anywhere on the line. There may exist, and indeed do, complex solutions which do cross the Fermi line, making this low-loss approximation only appropriate for small wavevectors away from $\omega = v_F q$.

In order to present an accurate analysis of the single particle excitation processes in graphene the CFPD must be solved for exactly, first in the equilibrium case and subsequently in general for arbitrary nonequilibrium electronic distributions.

In Ref. [173] an analytic expression for the polarisability is presented, which subject to a change of unit convention and some refactoring, is given as,

$$\Pi_\mu^{T=0}(\mathbf{q}, \omega) := \Pi[f(\epsilon - \mu, T = 0)](\mathbf{q}, \omega) \quad (4.10.a)$$

$$= \frac{g\mu}{8\pi\hbar^2 v_F^2} \tilde{\Pi}_1 \left(\frac{\hbar v_F \mathbf{q}}{\mu}, \frac{\hbar\omega}{\mu} \right), \quad (4.10.b)$$

where,

$$\tilde{\Pi}_1(\tilde{\mathbf{q}}, \tilde{\omega}) = -4 + \tilde{q}^2 \frac{G^+(\frac{2+\tilde{\omega}}{\tilde{q}}) + G^-(\frac{2-\tilde{\omega}}{\tilde{q}})}{2\sqrt{\tilde{q}^2 - \tilde{\omega}^2}}, \quad (4.10.c)$$

with $G^\pm(z) = z\sqrt{1-z^2} \pm i \operatorname{arccosh}(z)$ and under the prescription that the frequency gains an infinitesimal positive imaginary part, $\omega \rightarrow \omega + i \times 0$. Negative values of μ are handled by prescribing that Π only depends on the absolute value of μ due to particle/hole symmetry.

The RPA plasmon dispersion can be solved for exactly. Given the analytic form of the polarisability, Eq. 4.10, the value of Π may be given directly as a function of a complex frequency. The exact solution deviates from the low-loss approximation when the curve enters the regime of Landau damping. In Ref. [173] the exact solution is plotted up to the point before the dispersion curve crosses the Fermi line. In this work, this is extended to show the exact CFPD solution for any wavevector including in the intraband regime where $v_F q > \omega$ [193].

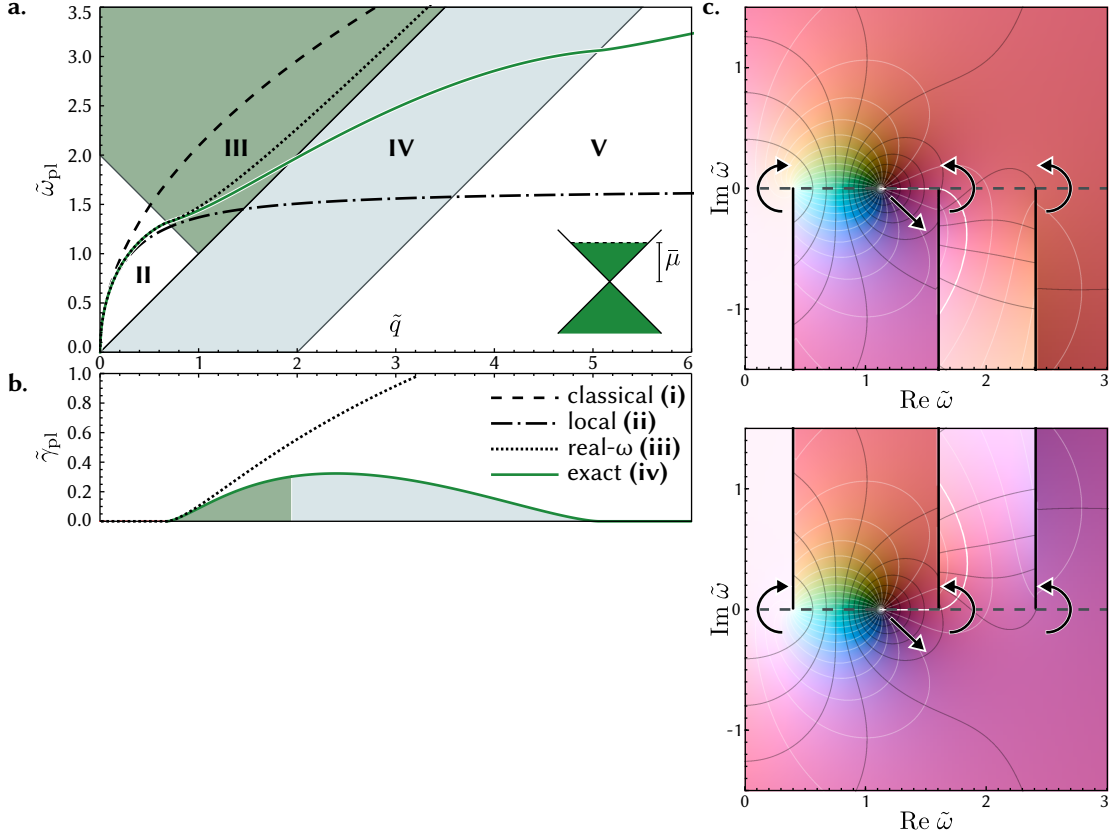


Figure 4.2: Complex frequency plasmon dispersion of equilibrium graphene.

a. Plasmon dispersion relation and b. loss of doped graphene in thermal equilibrium. Quantities are scaled to the chemical potential and Fermi velocity. The exact RPA solution CFPD is plotted (green solid line) with the low-loss approximation (black dotted line), the optical conductivity (black dot-dashed line), and Drude model (black dashed line). Regions of Landau damping are shown for interband (II: green) and intraband (IV: gray) processes, as well as for quasi-loss-free regions (II,V: white). Scaled coordinates are used where $\tilde{q} = \hbar v_F q / \mu$, $\tilde{\omega}_{\text{pl}} = \hbar \omega_{\text{pl}} / \mu$ c. For a fixed q , the value of ε_{RPA} is plotted over a complex $\tilde{\omega}$ (Sec. A.1). When the root crosses the real line, from the upper half-space to the lower, branches must be rotated 180° such as not to pass over it. Allowing the root to be found in a branch-free lower half-space.

The exact CFPD is solved and shown in Fig. 4.2.a for plasmons of zero-temperature equilibrium graphene with a finite chemical potential. For comparison, this is shown alongside the low-loss approximation as described in Eq. 4.9, as well as solving for a 2D Drude conductivity and a local ($q \rightarrow 0$) optical conductivity approximation [105]. The curves are plotted on top of the regions in (q, ω) space where single particle excitations are kinematically allowed (in green for interband, and gray for intraband), i.e. where the polarisability has finite imaginary part for real frequency and wavevector. The regions in white can not play part in absorption or emission processes, as transitions here cannot fulfil conservation of momentum, and as such the polarisability has zero imaginary part in these regions for real frequency and wavevector. For small wavevector, all solutions converge onto each other, before the Drude model solution separates off. Whilst in the quasi-loss-free region, the low-loss and CFPD solutions are identical, with the optical conductivity beginning to separate off. Within the interband Landau damping regime, the low-loss and CFPD solution deviate, with the low-loss tracking alongside the Fermi line, being unable to cross it. The CFPD however continues passing through the interband Landau damping regime, over the Fermi line, through the intraband Landau damping regime and out into the large wavevector quasi-loss-free regime. Due to the singularity at $\omega = v_F q$, the low-loss approximation can never cross the Fermi line, however the exact solution is able to bypass the singularity having acquired a finite imaginary part, and enter into the intraband absorption region.

In order to determine the roots of the dielectric function (Eq. 4.5), one must note that the polarisability function is multi-valued with branch cuts in the complex- ω plane. The form of the function as given in Eq. 4.10 is one configuration of the branches of this multiply valued function, i.e. a configuration that gives the correct value for real q and ω . It is analytic in the upper-half plane with branch cuts along the real

axis. The branch-cuts themselves are not physical; different versions of the function may be formulated which are identical in the vicinity of a particular value of ω for which the branch cuts differ. One can move smoothly from one branch to another in a process called *analytic continuation* where any path in a complex variable's space, i.e. ω here, varies smoothly from one value to the next parameterised along the path. The analytic continuation along a path is unique as long as the path does not pass through any singularities.

In order to solve for the dispersion relation, the wavevector q is swept along real values from zero, then for each value of q the branches of the function are chosen such that they are moved out of the way of the vicinity of the root in ω . Practically this means for $\text{Im } \omega > 0$, the branches, which hang from branch-point singularities on the real axis that cannot be removed, are chosen to point vertically and downwards (occupying the lower half space); and for $\text{Im } \omega < 0$, the branches point vertically and upwards. When the branch configuration changes, there is the choice as to whether to rotate each branch-cut clockwise or counter-clockwise, chosen such that the branch cuts will never sweep over the root that is being traced, as depicted in Fig. 4.2.b.

The resulting plasmon dispersion and loss curve that is retrieved from this procedure (solid line in Fig. 4.2) is continuous, with zero loss in the regions of no Landau damping and smooth throughout the damping regions including when crossing over the Fermi line.

4.3. Nonequilibrium Polarisability

The polarisability is an important object in its own right, apart from its inclusion in the plasmon dispersion and optical conductivity, it is used in dynamic screening of the Coulomb potential $\bar{V}_q = V_q/\varepsilon_{\text{RPA}}(\mathbf{q}, \omega)$ [194]. The screening enters into higher-order processes such as carrier-carrier and Auger processes [158] (Auger recombination,

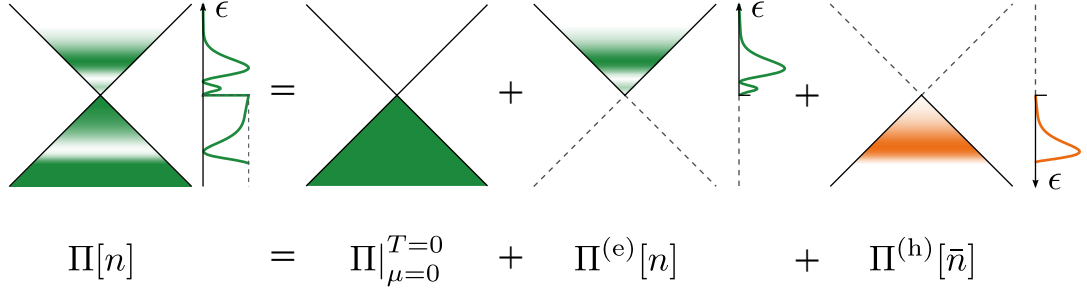


Figure 4.3: **Nonequilibrium polarisability.**

The nonequilibrium polarisability is a linear functional of the carrier distribution $n(\epsilon)$ and can be decomposed into a background intrinsic zero-temperature equilibrium polarisability plus contributions from nonequilibrium electrons and holes.

impact ionisation) as well as for coupling to other bosonic fields such as scattering with optical phonons [195, 196, 197]. Calculating the polarisability in increasingly complicated electronic configurations has been the subject of much research [198, 136, 170, 137, 174, 156].

The Lindhard formula for graphene Eq. 4.7, which was used to derive the equilibrium polarisability, is noted to be a linear functional of the carrier distribution $n(\epsilon)$. Using only this and the fact that a zero-temperature Fermi distribution is equivalent to a Heaviside Theta function, $f(\epsilon - \mu, T = 0) = \theta(\mu - \epsilon)$, the graphene polarisability may be derived for any arbitrary nonequilibrium carrier distribution. Starting with the following linearity identity,

$$\Pi[n] = \Pi \left[\int_{-\infty}^{\infty} d\epsilon \delta(\epsilon - \epsilon') n(\epsilon) \right] \quad (4.11.a)$$

$$= \int_{-\infty}^{\infty} d\epsilon \Pi [\delta(\epsilon - \epsilon')] n(\epsilon)$$

$$= \int_{-\infty}^{\infty} d\epsilon \Pi \left[\frac{\partial f(\epsilon' - \epsilon, T = 0)}{\partial \epsilon} \right] n(\epsilon)$$

$$\Pi[n] = \int_{-\infty}^{\infty} d\epsilon \frac{\partial \Pi_{\mu=\epsilon}^{T=0}}{\partial \epsilon} n(\epsilon). \quad (4.11.b)$$

This form integrates over the sea of filled hole states, which is divergent as it takes a

limit of an ever growing Fermi-edge to negative infinity. To regularise this integral one may separate off the carrier distribution into an intrinsic part and contributions from electrons and holes, as in Fig. 4.3, i.e.

$$n(\epsilon) = \underbrace{\theta(-\epsilon)}_{\text{intrinsic}} + \underbrace{n(\epsilon)\theta(\epsilon)}_{\text{electrons}} - \underbrace{\bar{n}(-\epsilon)\theta(-\epsilon)}_{\text{holes}}, \quad (4.12)$$

where $\bar{n}(\epsilon) = 1 - n(-\epsilon)$ is the hole distribution. This leads to the following elegant form³:

$$\Pi[n] = \Pi_{\mu=0}^{T=0} + \int_0^\infty d\epsilon \left[\frac{\partial \Pi_{\mu=\epsilon}^{T=0}}{\partial \epsilon} n(\epsilon) + \frac{\partial \Pi_{\mu=-\epsilon}^{T=0}}{\partial \epsilon} \bar{n}(\epsilon) \right] \quad (4.13)$$

$$= \Pi_{\mu=0}^{T=0} + \Pi^e[n] = \Pi^h[\bar{n}]. \quad (4.14)$$

The nonequilibrium polarisability is formed here of a background contribution of a zero temperature intrinsic equilibrium added to terms for the particle and hole plasmas. This allows the calculation of any nonequilibrium polarisability for any given carrier distribution $n(\epsilon)$ and is well suited to numerical evaluation, more details of which will be given in Sec. 4.6. The formalism here is general, and particularly does not include any graphene or approximation-specific features, such as band structure characteristics, relying only on the linearity of the Lindhard formula, a feature of taking the leading order term in RPA, and in the absence of self-energy corrections. This formalism is therefore applicable to calculating the polarisability and dielectric function out of equilibrium of general 2D fermion gasses within RPA.

4.3.1. Scale-free Representation

The conical band-structure of graphene, $\epsilon_k^s = s\hbar v_F |\mathbf{k}|$, does not define any energy scale, which can be shown to lead to a universal behaviour, described by scale-free coordinates.

³ Assuming particle/hole symmetry, as usual, means $\frac{\partial \Pi_{\mu=-\epsilon}^{T=0}}{\partial \epsilon} = \frac{\partial \Pi_{\mu=\epsilon}^{T=0}}{\partial \epsilon}$ and therefore, $\Pi^e = \Pi^h$

Taking the Lindhard Formula, Eq. 4.7, and scaling the dynamic variables, $\mathbf{q} \rightarrow \mathbf{q}/a$, $\omega \rightarrow \omega/a$ and carrier distribution, $n'(\epsilon) = n(a\epsilon)$, by a constant factor a , gives,

$$\begin{aligned}\Pi[n](\mathbf{q}, \omega) &= \frac{g}{A} \sum_{s,s'=\pm} \sum_{\mathbf{k}} M_{\mathbf{k},\mathbf{k}+\mathbf{q}}^{ss'} \frac{n(\epsilon_{\mathbf{k}}^s) - n(\epsilon_{\mathbf{k}+\mathbf{q}}^{s'})}{\epsilon_{\mathbf{k}}^s - \epsilon_{\mathbf{k}+\mathbf{q}}^{s'} + \hbar\omega + i \times 0} \\ &= \frac{g}{A} \sum_{s,s'=\pm} a^2 \sum_{\mathbf{k}/a} M_{\frac{\mathbf{k}}{a}, \frac{\mathbf{k}+\mathbf{q}}{a}}^{ss'} \frac{n(a\epsilon_{\mathbf{k}/a}^s) - n(a\epsilon_{(\mathbf{k}+\mathbf{q})/a}^{s'})}{a\epsilon_{\mathbf{k}/a}^s - a\epsilon_{(\mathbf{k}+\mathbf{q})/a}^{s'} + a\hbar\omega/a + i \times 0} \\ &= a \frac{g}{A} \sum_{s,s'=\pm} \sum_{\mathbf{k}/a} M_{\frac{\mathbf{k}}{a}, \frac{\mathbf{k}+\mathbf{q}}{a}}^{ss'} \frac{n'(\epsilon_{\mathbf{k}/a}^s) - n'(\epsilon_{(\mathbf{k}+\mathbf{q})/a}^{s'})}{\epsilon_{\mathbf{k}/a}^s - \epsilon_{(\mathbf{k}+\mathbf{q})/a}^{s'} + \hbar\omega/a + i \times 0}\end{aligned}\quad (4.15.a)$$

$$\Pi[n](\mathbf{q}, \omega) = a\Pi[n']\left(\frac{\mathbf{q}}{a}, \frac{\omega}{a}\right), \quad (4.15.b)$$

as a scaling rule. Borrowing from the form of Eq. 4.10.a, one can express polarisabilities in a form with all variables scaled to an energy $\bar{\mu}$.

$$\Pi[n(\epsilon)](\mathbf{q}, \omega) = \frac{g\bar{\mu}}{8\pi\hbar^2 v_F^2} \tilde{\Pi}[n(\tilde{\epsilon})] \left(\frac{\hbar v_F \mathbf{q}}{\bar{\mu}}, \frac{\hbar\omega}{\bar{\mu}} \right) \quad (4.16.a)$$

$$= \frac{g\bar{\mu}}{8\pi\hbar^2 v_F^2} \tilde{\Pi}[n(\tilde{\epsilon})](\tilde{\mathbf{q}}, \tilde{\omega}), \quad (4.16.b)$$

with the the following scaling definitions, $\tilde{\mathbf{q}} = \hbar v_F \mathbf{q} / \bar{\mu}$, $\tilde{\omega} = \hbar\omega / \bar{\mu}$, and $\tilde{\epsilon} = \epsilon / \bar{\mu}$, where variables marked with a tilde are scaled to $\bar{\mu}$, and the dimensionless $n(\tilde{\epsilon})$ replaces the absolute $n(\epsilon)$.

The universality becomes most clear when calculating the dielectric function, Eq. 4.5 becomes,

$$\varepsilon_{\text{RPA}}(\tilde{\mathbf{q}}, \tilde{\omega}) = 1 - \frac{\alpha_g}{\tilde{q}} \tilde{\Pi}(\tilde{\mathbf{q}}, \tilde{\omega}), \quad (4.17)$$

with the graphene fine-structure constant [199, 189],

$$\alpha_g = \frac{g}{4} \frac{c}{v_F} \frac{\alpha_0}{\bar{\epsilon}}, \quad (4.18)$$

where $\alpha_0 \approx 1/137$ is the vacuum fine-structure constant. Which for suspended graphene takes a value of $\alpha_g \approx 2.2$.

Finally, it remains to cast the derivative form (Eq. 4.13) in dimensionless terms.

$$\frac{\partial \Pi_{\mu}^{T=0}}{\partial \mu} = \frac{\partial}{\partial \mu} \Pi[f(\epsilon - \mu, T = 0)](\mathbf{q}, \omega) \quad (4.19.a)$$

$$= \frac{g}{8\pi\hbar^2 v_F^2} \frac{\partial}{\partial \tilde{\mu}} \left[\tilde{\epsilon}' \tilde{\Pi}_1 \left(\frac{\tilde{\mathbf{q}}}{\tilde{\mu}}, \frac{\tilde{\omega}}{\tilde{\mu}} \right) \right] \\ := \frac{g}{8\pi\hbar^2 v_F^2} \tilde{\Pi}'(\tilde{\mu}; \tilde{\mathbf{q}}, \tilde{\omega}) , \quad (4.19.b)$$

leading to the scale-free expression for polarisabilities of arbitrary carrier distributions:

$$\tilde{\Pi}[n](\tilde{\mathbf{q}}, \tilde{\omega}) = \tilde{\Pi}_0(\tilde{\mathbf{q}}, \tilde{\omega}) + \int_0^\infty d\tilde{\epsilon} \left[\tilde{\Pi}'(\tilde{\epsilon}; \tilde{\mathbf{q}}, \tilde{\omega}) n(\tilde{\epsilon}) + \tilde{\Pi}'(\tilde{\epsilon}; \tilde{\mathbf{q}}, \tilde{\omega}) \bar{n}(\tilde{\epsilon}) \right] , \quad (4.20)$$

with $\tilde{\Pi}_0 = \lim_{a \rightarrow 0} a \tilde{\Pi}_1(\tilde{\mathbf{q}}/a, \tilde{\omega}/a)$, being the dimensionless form of the intrinsic polarisability.

Within the Dirac-cone approximation, specific form of these terms may given as,

$$\tilde{\Pi}'(\tilde{\epsilon}; \tilde{\mathbf{q}}, \tilde{\omega}) = -4 + 2 \frac{G' \left(\frac{\tilde{\omega}+2\tilde{\epsilon}}{\tilde{q}} \right) + G' \left(\frac{\tilde{\omega}-2\tilde{\epsilon}}{\tilde{q}} \right)}{G' \left(\frac{\tilde{\omega}}{\tilde{q}} \right)} \quad (4.21.a)$$

$$\tilde{\Pi}_0 = -\frac{\tilde{q}}{2} \frac{\pi}{G' \left(\frac{\tilde{\omega}}{\tilde{q}} \right)} , \quad (4.21.b)$$

with,

$$G'(z) = \sqrt{1 - z^2} , \quad (4.21.c)$$

for $\tilde{\omega} \rightarrow \tilde{\omega} + 0i$.

As the solutions to Eq. 4.17 are independent of energy scale $\bar{\mu}$, all dispersion curves of electronic configurations that are similar (equal but for scale) can be mapped onto a single curve $\tilde{\omega}(\tilde{\mathbf{q}})$ of dynamic variables that are set to the same energy scale.

4.4. Quasiequilibrium

The first nonequilibrium state of graphene to consider is the quasiequilibrium where the electronic distribution in the conduction band and the valence band can both be

described by Fermi functions, with each having their own separate chemical potential, albeit sharing a common temperature. This serves as a first approximation to photoexcited graphene. When graphene is externally pumped by photons, they may be absorbed creating electron-hole pairs in a hot carrier distribution. The hot carrier distribution then relaxes and each band thermalises independently, assuming that intraband relaxation channels such as carrier-carrier scattering are at least an order of magnitude faster (tens of femtoseconds) [165, 166, 167, 159, 152, 155] than interband recombination processes, which themselves can be ultrafast [150, 200, 162, 168, 169]. This leaves the system in a momentary state of population inversion [201, 202] from where stimulated emission processes may exceed the rates of absorption allowing for net gain. The quasiequilibrium is therefore a snapshot of an evolving system that is modelled by a pair of Fermi distributions parameterised by electron and hole chemical potentials, μ_e , μ_h and temperature T , which will seek to return to equilibrium over time, as will be explored in Sec. 4.8.

An alternative way to parameterise the system would be through the carrier number and energy densities, N_e , N_h , U , which are found by summing over wavevector states for each species, $s \in \{e, h\}$,

$$N_s(\mu_s, T) = \frac{g}{A} \sum_{\mathbf{k}} f(\epsilon_{\mathbf{k}}^s - \mu_s, T) \quad (4.22a)$$

$$U_s(\mu_s, T) = \frac{g}{A} \sum_{\mathbf{k}} f(\epsilon_{\mathbf{k}}^s - \mu_s, T) \epsilon_{\mathbf{k}} , \quad (4.22b)$$

with the total energy density $U = U_e + U_h$. These integrate to polylogarithm functions [203],

$$N_s(\mu_s, T_c) = -\frac{2}{\pi} \frac{(k_B T)^2 \text{Li}_2(-e^{\mu_s/k_B T})}{(\hbar v_F)^2} \quad (4.23a)$$

$$U_s(\mu, T_c) = -\frac{4}{\pi} \frac{(k_B T)^3 \text{Li}_3(-e^{\mu_s/k_B T})}{(\hbar v_F)^2} . \quad (4.23b)$$

The carrier number and energy density become useful when considering the dynamics

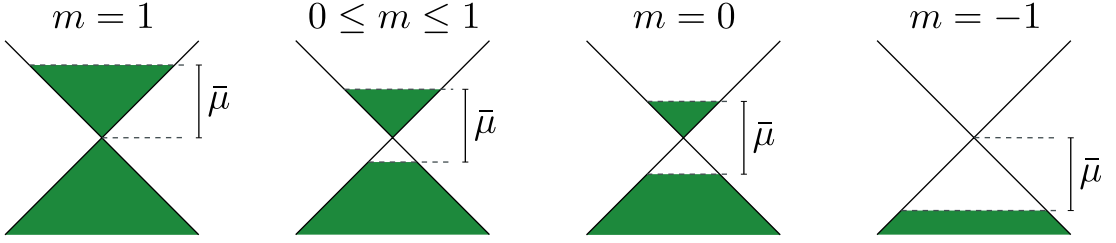


Figure 4.4: Carrier imbalance parameter.

The parameter m labels graphene variously in a state of n-doped equilibrium ($m = 1$), n-doped photoinverted quasiequilibrium ($0 \leq m \leq 1$), intrinsic photoinverted quasiequilibrium ($m = 0$), and p-doped quasiequilibrium ($m < 0$).

of the system, i.e. how it responds to external pumping such as photoexcitation, and how it subsequently relaxes.

The result of Sec. 4.3 can be immediately applied to the case of a zero-temperature quasiequilibrium. Assuming electrons and holes can be described respectively with chemical potentials μ_e, μ_h , then their distribution becomes,

$$n = f(\epsilon - \mu_e, T = 0) = \theta(\mu_e - \epsilon) \quad (4.24.a)$$

$$\bar{n} = f(\epsilon - \mu_h, T = 0) = \theta(\mu_h - \epsilon). \quad (4.24.b)$$

Inserting into Eq. 4.20 yields,

$$\tilde{\Pi}_{\mu_e, \mu_h}(\tilde{\mathbf{q}}, \tilde{\omega}) = \tilde{\Pi}_0(\tilde{\mathbf{q}}, \tilde{\omega}) + \int_0^\infty d\tilde{\epsilon} \tilde{\Pi}'(\tilde{\epsilon}; \tilde{\mathbf{q}}, \tilde{\omega}) [\theta(\mu_e - \epsilon) + \theta(\mu_h - \epsilon)]. \quad (4.25)$$

Then by extension of the integration range of Eq. 4.20 leads to,

$$\tilde{\Pi}_{\mu_e, \mu_h}(\tilde{\mathbf{q}}, \tilde{\omega}) = \tilde{\Pi}_0(\tilde{\mathbf{q}}, \tilde{\omega}) \quad (4.26.a)$$

$$\begin{aligned} &+ \int_{-\infty}^{\infty} d\tilde{\epsilon} \tilde{\Pi}'(\tilde{\epsilon}; \tilde{\mathbf{q}}, \tilde{\omega}) [\theta(\mu_e - \epsilon) - \theta(-\epsilon) + \theta(\mu_h - \epsilon) - \theta(-\epsilon)] \\ &= \frac{\mu_e}{\bar{\mu}} \tilde{\Pi}_1 \left(\frac{\tilde{q}\bar{\mu}}{\mu_e}, \frac{\tilde{\omega}\bar{\mu}}{\mu_e} \right) + \frac{\mu_h}{\bar{\mu}} \tilde{\Pi}_1 \left(\frac{\tilde{q}\bar{\mu}}{\mu_h}, \frac{\tilde{\omega}\bar{\mu}}{\mu_h} \right) - \tilde{\Pi}_0(\tilde{\mathbf{q}}, \tilde{\omega}). \end{aligned} \quad (4.26.b)$$

It makes sense to chose $\bar{\mu} = \mu_e + \mu_h$ as the scale parameter in this case, which allows us to further define the free parameter - the carrier imbalance parameter,

$$m = \frac{\mu_e - \mu_h}{\mu_e + \mu_h}. \quad (4.27)$$

This describes the imbalance of the electrons and holes in the carrier density, and ranges from $m = -1$ where $\mu_e = 0, \mu_h = \bar{\mu}$; to $m = 0$ where $\mu_e = \bar{\mu}/2, \mu_h = \bar{\mu}/2$; to $m = +1$ where $\mu_e = \bar{\mu}, \mu_h = 0$. This is illustrated in Fig. 4.4. Here only the range $m \in [0, 1]$ will be considered, as negative values of m return equivalent physics to positive ones due to the symmetry of the conduction and valence bands in the Dirac cone approximation. With this, Eq. 4.26.b becomes,

$$\tilde{\Pi}_m(\tilde{\mathbf{q}}, \tilde{\omega}) = \frac{1+m}{2} \tilde{\Pi}_1\left(\frac{2\tilde{q}}{1+m}, \frac{2\tilde{\omega}}{1+m}\right) + \frac{1-m}{2} \tilde{\Pi}_1\left(\frac{2\tilde{q}}{1-m}, \frac{2\tilde{\omega}}{1-m}\right) - \tilde{\Pi}_0(\tilde{q}, \tilde{\omega}). \quad (4.28)$$

When there are carriers in the conduction band above a range of vacant states in the valence band, there is a *population inversion*. In this state, electrons and holes can spontaneously recombine emitting a plasmon, but they can also recombine, emitting a coherent plasmon through stimulation by free plasmons on the sheet. Electrons in the conduction band, below μ_e , may recombine with holes in the valence band below μ_h . As such plasmons with energies below $\hbar\omega < \mu_e + \mu_h = \bar{\mu}$ may experience gain. The more similar the level of electron and hole populations are, the more phase space will be available for stimulated emission processes, from the maximal case of a symmetric (intrinsic) inversion for $m = 0$ down to no phase space for $m = \pm 1$ where there is no population inversion. Plasmons outside this frequency range may be absorbed, as was the case for equilibrium graphene, along with plasmons which can induce intraband transitions.

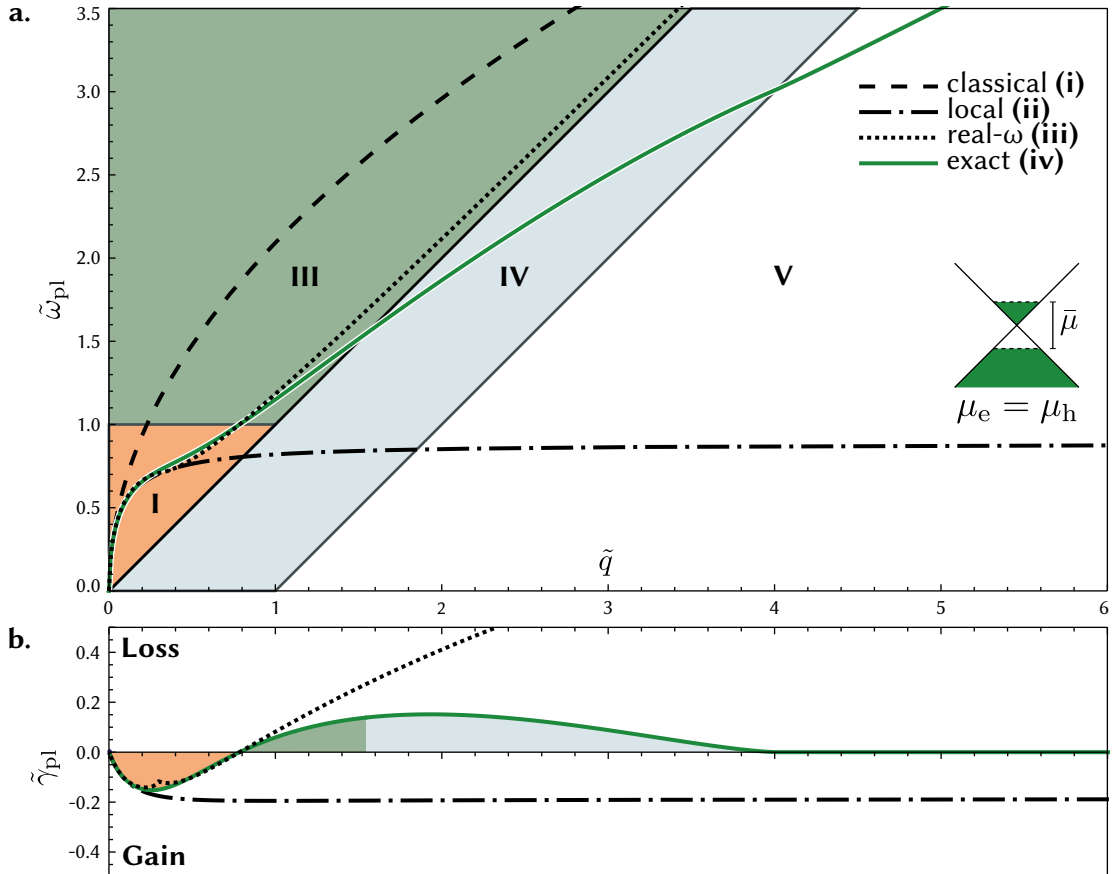


Figure 4.5: Complex frequency plasmon dispersion of photoinverted graphene.

a. Plasmon dispersion relation and b. loss of intrinsic graphene in photoinverted quasiequilibrium. The exact RPA solution CFPD is plotted (green solid) with the low-loss approximation (black dotted), the optical conductivity (black dot-dashed), and Drude model (black dashed). Regions of recombination are shown (i: orange) and regions for interband (ii: green) and intraband (iv: gray) damping, as well as for quasi-loss-free regions (v: white).

4.4.1. Intrinsic Graphene

The case of intrinsic inversion should be given some special attention. Optical excitation creates electrons and holes in a pairwise manner, given the equivalence of the conduction and valance band. Considering an intrinsic sheet of graphene that is optically pumped, the resulting quasiequilibrium after the initial excitation will have equal chemical potentials $\mu_e = \mu_h$, i.e. the imbalance parameter $m = 0$. The polarisability in this case takes the simplified form,

$$\tilde{\Pi}_{m=0}(\tilde{q}, \tilde{\omega}) = 2\tilde{\Pi}_1(\tilde{q}, \tilde{\omega}) - \tilde{\Pi}_0(\tilde{q}, \tilde{\omega}). \quad (4.29)$$

The CFPD can be solved for this photoinverted case and the result is plotted in Fig. 4.5 in analogy to Fig. 4.2, with the equivalent approximative solutions also plotted. Qualitatively, the curve is similar, following the Drude model curve for small \tilde{q} . However, for frequencies $\tilde{\omega}_{pl} < 1$, the plasmons are susceptible to stimulated emission of plasmons due to recombination of electron/hole pairs. This gives a negative decay rate $\tilde{\gamma}_{pl}$ which characterises amplification i.e. plasmon gain. This gain falls to zero for $\tilde{\omega}_{pl} = 1$ where there are no inverted electron hole pairs that have such an energy difference. For frequencies above this, the plasmon enters the interband Landau damping regime and has a positive decay rate again. At $T = 0$ the regions where emission and absorption processes occur are sharply separated at $\tilde{\omega}_{pl} = 1$: not only is the net rate zero here, but the rates for the separate absorption and emission processes go to zero, with emission having zero rate above $\tilde{\omega}_{pl} = 1$ and absorption having zero rate below. For finite temperature, the two rates will smear into all frequencies as the Fermi-edge is smeared, as will be discussed in Sec. 4.5.2. The curve then continues through the interband and intraband regions in a manner similar to the equilibrium plasmon.

In contrast to the CFPD, the low-loss approximation curve displays a distinctive and spurious dip in the gain region that arises from performing a Taylor expansion too close to a branch singularity at $\tilde{\omega} = 1 - \tilde{q}$. This curve, in common with its equilibrium

counterpart, cannot cross the Fermi line, but rather asymptotically approaches it with a loss that continues growing.

The dispersion under the local optical conductivity model limits to a finite value. Given that its model is local and can only see vertical transitions i.e. $q \rightarrow 0$, the loss is negative over the entire curve and as such only interband recombination processes are accounted for.

In this section, it has been shown how the inverted plasmon dispersion differs from that of equilibrium, how the CFPD solution of a nonlocal RPA polarisability is able to return accurate results in all absorption/emission regimes that other approximations can not. The CFPD also yields the exact plasmon gain/loss rate within the RPA, allowing for further analysis.

4.4.2. Extrinsic Graphene

The chemical potential of Graphene can be set by an external gate voltage, or by chemical doping of the sample, or indeed by interaction with the substrate. This has the effect of adding an excess of one species of carrier, either electrons or holes. When there is a difference between the number of electrons and holes, i.e. $N_e \neq N_h$, the carrier imbalance parameter, m , of extrinsic graphene will take an intermediate value between 0 and 1.

Figure 4.6 shows the regions in reciprocal space for which plasmons experience gain (I: orange), interband absorption (II: green), intraband absorption (IV: gray), and regions with no phase space for these processes (III: white). The relative sizes of these regions change with m , starting from equilibrium at $m = 1$ where the gain region (I) is vanishing and there is a large triangular loss-free region (II), down to $m = 0$ at full inversion where the loss-free triangle has shrunk to vanish, leaving a gain triangle in place. These extremal cases can be seen in Figs. 4.2 and 4.5. For intermediate values

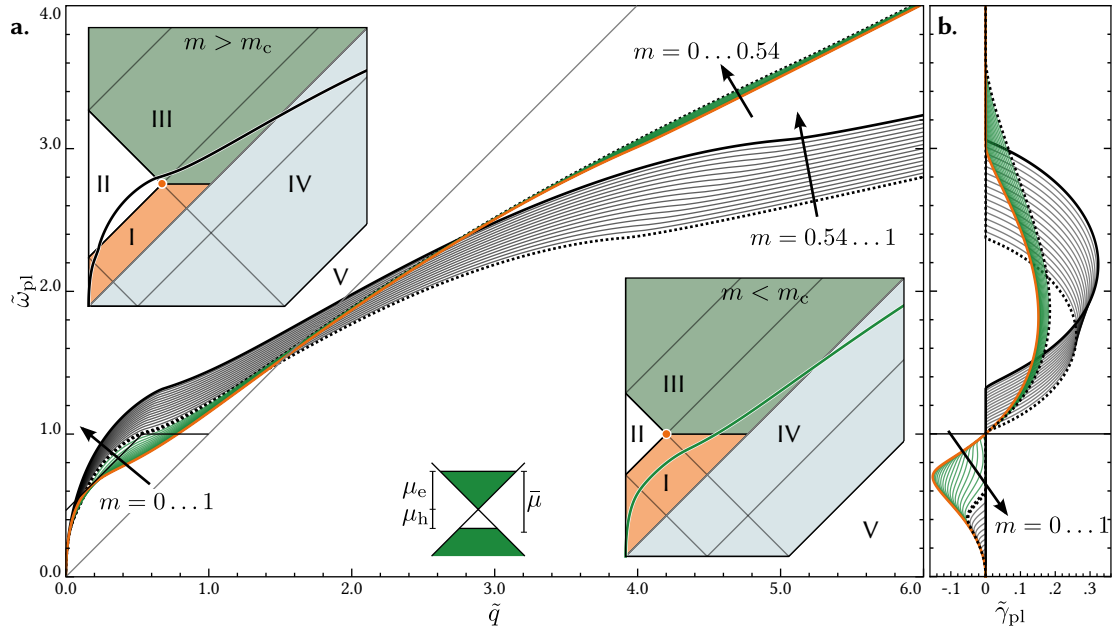


Figure 4.6: Complex frequency plasmon dispersion for varying carrier imbalance

a. Complex frequency dispersion curves of extrinsic photoinverted graphene for a varying carrier inversion parameter, $0 < m < 1$. The curves split into two bundles at a critical value m_c . Insets show representative curves either side of the splitting, shown against regions of Landau damping and recombination, the black curves passing above the critical branch point (orange dot) and the green curves below. b. Loss plotted over the frequency. For frequencies less than 1, the curves smoothly morph into each other, whereas past this range, a distinct splitting occurs.

the gain region becomes a trapezium with its upper vertex defining its size, located at $(\tilde{q} = m, \tilde{\omega} = 1)$. The loss free region remains a triangle as m is varied.

A range of CFPD curves for values of m between 0 and 1 are plotted. The extremal values of $m = 1$ (doped equilibrium), and $m = 0$ (intrinsic inverted) are drawn with the swarm of intermediate curves in-between. Two different families of curves are to be found, one set that passes from interband gain to interband loss directly, and the other that passes through the quasi loss-free region in-between. The first set includes the $m = 0$ curve, and each of the curves in the bundle follow the character of this curve tightly. The latter bundle includes the $m = 1$ curve, and although all the curves smoothly vary from one to another, there is more variance in this bundle. Whereas these bundles start out together, they start to diverge for $\tilde{\omega} > 1$, and varying m . This splitting is more clearly seen when considering the loss. The values of ω_{pl} are monotonic in q , which allows the loss γ_{pl} to be plotted, in a more instructive manner as a function of frequency instead of wavevector. This separates the gain spectrum into a gainy part, for $\omega_{pl} < 1$, and a lossy part for $\omega_{pl} > 1$. The loss shows a step change between the bundles about this point. The curves for a low- m pass through $(\omega_{pl} = 1, \gamma_{pl} = 0)$ with finite gradient, whereas the low- m curves are already trailing with a zero imaginary part having entered the quasi-loss-free regime beforehand. As the dispersion bundles have separated, the frequencies at which the curves leave the intraband absorption region, and hence when the loss returns to zero, do not match between each bundle. Even though the curves themselves are smooth and within a bundle, they show a marked bifurcation between the bundles. The mathematical origin of this is the curves entering onto a different leaf of the dielectric function's Riemann sheet. A more robust physical explanation is more elusive, and will remain the subject for future investigation. The critical value of m for which the transition occurs can be solved for. Since the character of the dispersion curve is dependent on

which side of the critical branch point (orange point) it passes. The branch point is located at $(\tilde{q} = m, \tilde{\omega} = 1)$, where regions I, II and III come together, so finding the critical branching value is finding the curve that passes through that point, i.e.

$$1 - \frac{\alpha_g}{m_c} \tilde{\Pi}_{m=m_c}(m_c, 1) = 0 . \quad (4.30)$$

For the case of suspended graphene, this takes a value of $m_c \approx 0.538$.

In this section, the idealised case of graphene in zero-temperature quasiequilibrium, which approximates the state of photoexcited graphene tens of femtoseconds after the initial excitation, was studied. The loss/gain profile was extracted for all curves parameterised by the carrier imbalance parameter, m , and scaled to the energy $\bar{\mu} = \mu_e + \mu_h$. A discontinuous behaviour was observed which separates the curves into a family of intrinsic-like curves and extrinsic-like ones.

4.5. Collision Loss and Temperature

This section improves on the polarisability model by considering collision losses, and then the impact of finite temperature on the CFPD and gain spectra of photoinverted graphene.

4.5.1. Collision Loss

Thus far graphene has been portrayed with its only source of loss coming from Landau damping. This so-far overlooks Drude losses, the presence of which is universal in traditional metal plasmonics [138]. In the simplest model, effects such as electron collisions with impurities, phonons [139], and other electrons, can be characterised by a collective collision time τ in the femtosecond range [175]. Such effects vary from sample to sample [165, 204] and through interaction with a substrate [205]. In a first model, τ is kept as a free parameter. The effect of collision loss on a polarisability

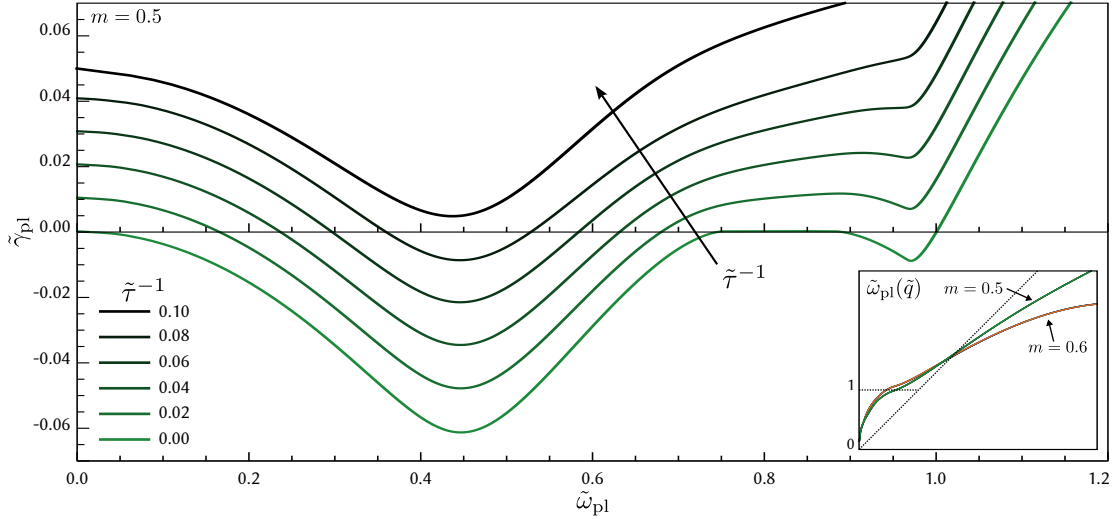


Figure 4.7: Impact of collision loss on plasmon decay rate.

Decay rate, at $m = 0.5$, as collision loss is added with scaled rates $\tilde{\tau}^{-1}$ from 0 to 0.1.

The corresponding plasmon dispersion is plotted inset for curves before and after the critical splitting (green and orange lines respectively) to no significant variation with collision rate.

function is properly treated by making the transformation [206]:

$$\tilde{I}_{\tilde{\tau}}(\tilde{\mathbf{q}}, \tilde{\omega}) = \frac{(\tilde{\omega} + i\tilde{\tau}^{-1})\tilde{I}(\tilde{\mathbf{q}}, \tilde{\omega} + i\tilde{\tau}^{-1})}{\tilde{\omega} + i\tilde{\tau}^{-1}\tilde{I}(\tilde{\mathbf{q}}, \tilde{\omega} + i\tilde{\tau}^{-1})/\tilde{I}(\tilde{\mathbf{q}}, 0)}, \quad (4.31)$$

which conserves local particle number, in contrast to the more simplistic addition of a uniform imaginary part, $\omega_{pl} - i\gamma_{pl} \rightarrow \omega_{pl} - i\gamma_{pl} - i\tau^{-1}$, which does not. Equation 4.31 can be applied to any of the polarisabilities introduced so far to solve for the CFPD in cases of photoinversion. Figure 4.7 shows the effect on the loss spectrum of adding finite collision loss in the range, $\tilde{\tau}^{-1} \in [0, 0.1]$ where $\tilde{\tau}^{-1} = \hbar\tau^{-1}/\bar{\mu}$.

The first thing of note is that the dispersion is not significantly affected by the incorporation of collision loss, and neither is the critical carrier inversion parameter m_c which separates the two bundles. Dispersion curves are plotted for two values of m and various values of $\tilde{\tau}$, which sit almost exactly on top of each other. What does change is the loss spectrum, which shifts by around $\tilde{\tau}^{-1}/2$. The curve also flattens out with the minimum becoming shallower for increasing $\tilde{\tau}^{-1}$. For a scale parameter

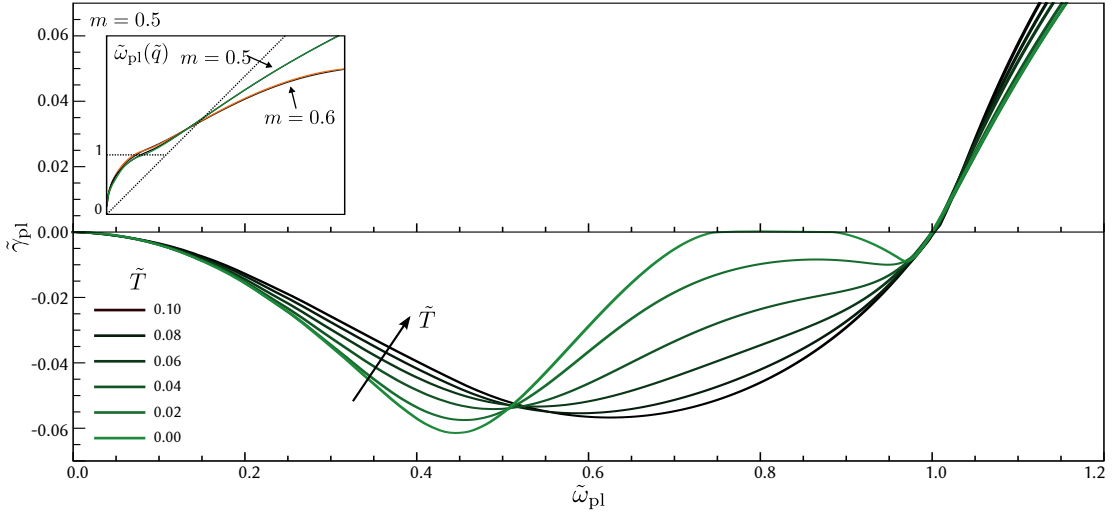


Figure 4.8: Impact of temperature on plasmon decay rate.

Decay rate, at $m = 0.5$, for scaled temperatures \tilde{T} from 0 to 0.1. The corresponding plasmon dispersion is plotted inset for curves before and after the critical splitting (green and orange lines respectively) to no significant variation with temperature.

of $\bar{\mu} = 0.2$ eV, the maximum value of $\tilde{\tau}^{-1} = 0.1$ corresponds to a collision time of $\tau = 16$ fs. At this collision rate all of the gain is extinguished, however for rates below this, there are frequency bands for which the collision loss is compensated by recombination, and the plasmons can be undamped and even still amplified.

4.5.2. Low Temperatures

The approximation that photoinverted graphene will relax to a quasiequilibrium can be improved by generalising the polarisability to finite temperatures. This question has been first addressed in the literature for finite temperature equilibria [174] but the form does not allow for the insertion of complex variables, nor hence the calculation of the CFPD.

The electronic distribution of a finite temperature quasiequilibrium can be represented as a correction to the zero temperature step function about the Fermi-level as

illustrated in Fig. 4.8. Due to the linearity in the electron distribution of the polarisability, an expression similar to Eq. 4.20 can be derived,

$$\tilde{\Pi}_m^{\tilde{T}} = \tilde{\Pi}_m + \int_0^\infty d\tilde{\epsilon} \tilde{\Pi}'(\tilde{\epsilon}) (\delta f(\tilde{\epsilon} - \tilde{\mu}_e, \tilde{T}) + \delta f(\tilde{\epsilon} - \tilde{\mu}_h, \tilde{T})) , \quad (4.32)$$

with $\delta f(\tilde{\epsilon} - \tilde{\mu}, \tilde{T}) = f(\tilde{\epsilon} - \tilde{\mu}, \tilde{T}) - f(\tilde{\epsilon} - \tilde{\mu}, 0)$, or breaking this down into separate integral components,

$$\begin{aligned} \tilde{\Pi}_m^{\tilde{T}} = & \tilde{\Pi}_m + \int_{\tilde{\mu}_e}^\infty d\tilde{\epsilon} \tilde{\Pi}'(\tilde{\epsilon}) f(\tilde{\epsilon} - \tilde{\mu}_e, \tilde{T}) - \int_0^{\tilde{\mu}_e} d\epsilon \tilde{\Pi}'(\tilde{\epsilon}) f(\tilde{\mu}_e - \tilde{\epsilon}, \tilde{T}) \\ & + \int_{\tilde{\mu}_h}^\infty d\tilde{\epsilon} \tilde{\Pi}'(\tilde{\epsilon}) f(\tilde{\epsilon} - \tilde{\mu}_h, \tilde{T}) - \int_0^{\tilde{\mu}_h} d\epsilon \tilde{\Pi}'(\tilde{\epsilon}) f(\tilde{\mu}_h - \tilde{\epsilon}, \tilde{T}) . \end{aligned} \quad (4.33)$$

This expression gives the finite temperature polarisability as a zero temperature component plus finite temperature corrections. This can now be used to calculate finite temperature CFPD curves, however a subtlety needs to be addressed. The kernel of the integral, $\tilde{\Pi}'(\tilde{\epsilon}; \tilde{\mathbf{q}}, \tilde{\omega})$ has branch points in $\tilde{\omega}$ space which vary in position with $\tilde{\epsilon}$, which is integrated over. It is weighed by Fermi functions that peak closest to the respective chemical potentials and decay exponentially away from this. It is therefore a good approximation, whilst \tilde{T} is small, to fix the branch points at $\tilde{\epsilon}$ to the *centre of mass* of the weight functions. The technical details of branch specification are detailed in Sec. A.2.

The gain/loss spectrum $\gamma_{pl}(\omega_{pl})$ is plotted (in analogy to Fig. 4.7, in Fig. 4.8) for values of \tilde{T} varying between 0 and 0.1 for an inversion of $m = 0.5$. These parameters correspond to a range of temperatures $T \in [0, 232.1]$ K for a scale of $\bar{\mu} = 0.2$ eV. As temperature increases, the gain peak blueshifts and broadens with the bimodal nature at $\tilde{T} = 0$ becoming a single peak. The peak gain value does not significantly diminish in this temperature range. Again, the dispersion curves $\omega_{pl}(\tilde{q})$, are not significantly affected on either side of the bundle splitting, though the critical parameter shifts slightly from $m_c \approx 0.56$ for $\tilde{T} = 0.1$ to $m_c \approx 0.538$ at zero temperature.

A point of note here is that the transition between gain and loss remains at $\tilde{\omega} = 1$ for all temperatures. At zero temperature, this would be the frequency above which the phase space of emission processes vanishes and that of absorption processes begins. For finite temperature, the smearing of the Fermi functions ensures that there is phase space for emission and absorption processes both above and below $\tilde{\omega} = 1$, however the net rate is balanced exactly at this point.

The approximation of treating the branches of Eq. 4.33 at single points begins to break down for $\tilde{T} \gtrsim 0.2$, see Fig. 4.9. This is because although Eq. 4.33 is analytic in the top-half $\tilde{\omega}$ plane, it is not so in the bottom half, such that when the plasmon transitions from gain to loss (i.e. at $\gamma_{\text{pl}} = 0, \omega_{\text{pl}} = 1$), the values of the polarisability are no longer strictly valid. It should be clarified however that the dispersion curves and loss spectrum for \tilde{q} before $\omega_{\text{pl}}(\tilde{q}) < 1$ are valid and are exact CFPD solutions. A more rigorous treatment of the nonequilibrium polarisability is required, which will be treated in the next section.

4.6. Hot Carriers

In order to calculate the CFPD for arbitrary carrier distributions, one needs to evaluate the integral of Eq. 4.13 and interpret this as a complex contour integral in $\tilde{\epsilon}$. Only one of the integral terms is considered here,

$$\Pi[n](\tilde{\mathbf{q}}, \tilde{\omega}) = \int_0^\infty d\tilde{\epsilon} \tilde{\Pi}'(\tilde{\epsilon}; \tilde{\mathbf{q}}, \tilde{\omega}) n(\tilde{\epsilon}) + \dots \quad (4.34)$$

This presents itself as an integral along the real axis from $\tilde{\epsilon} = 0$ to $\tilde{\epsilon} = \infty$, though any path through the complex $\tilde{\epsilon}$ plane with the same endpoints will yield the same value so long as the new path can be deformed onto the original in a continuous manner, without crossing any of the integrand's singularities.

There are two sources of singularities: from the kernel, $\tilde{\Pi}'(\tilde{\epsilon}; \tilde{\mathbf{q}}, \tilde{\omega})$, and from the

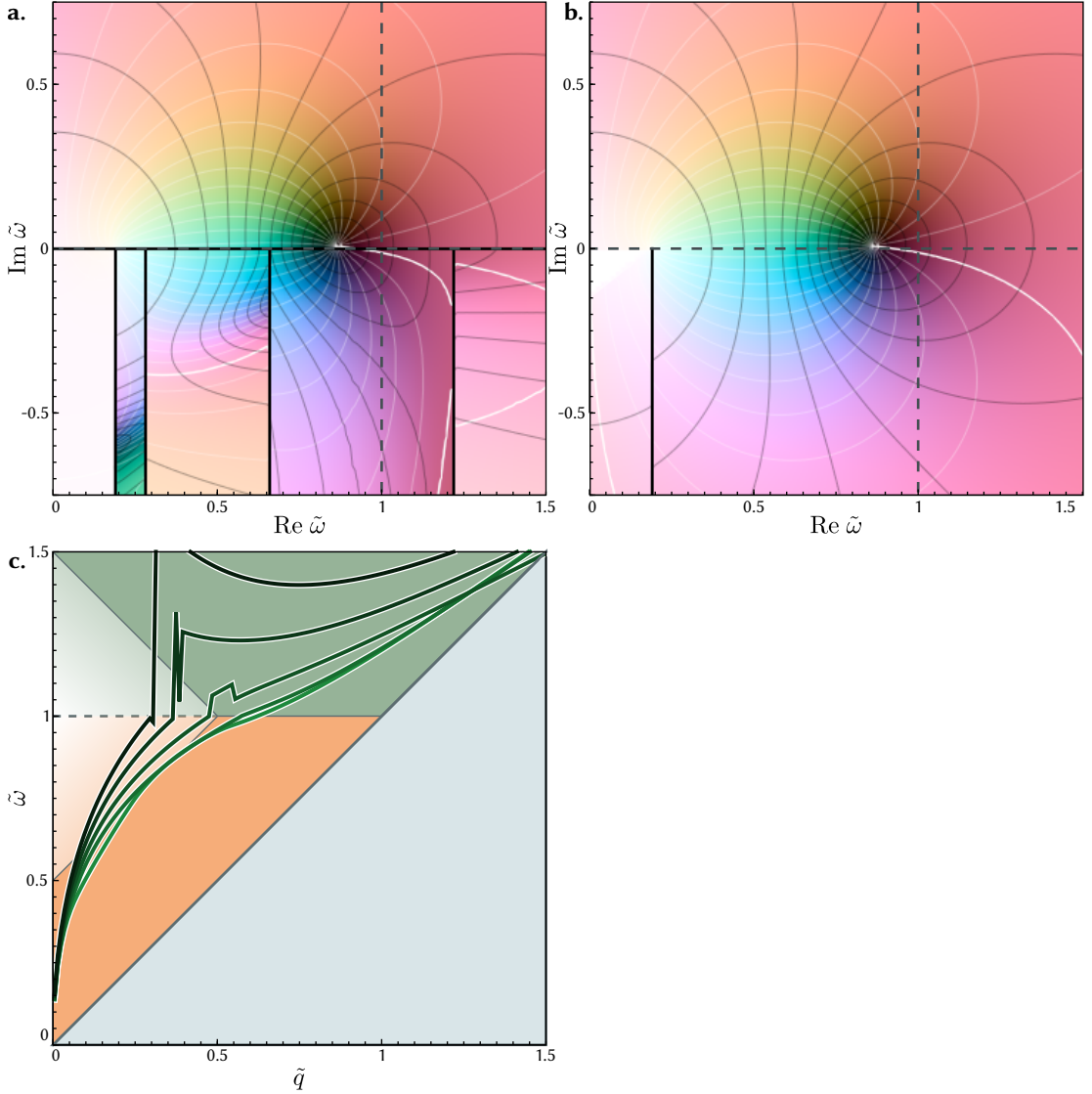


Figure 4.9: **Limitation of low-temperature polarisability approach.**

The solution space of $\varepsilon_{\text{RPA}}(\tilde{q}, \tilde{\omega})$ over a complex $\tilde{\omega}$ is plotted in **a.** and **b.** for quasiequilibrium graphene with $\tilde{T} = 0.5$, $m = 0.5$ at $\tilde{q} = 0.2$. The root is the encircled black spot, as described in Sec. A.1. **a.** uses the method of Sec. 4.5.2, and is analytic in the upper half-plane, but not in the lower, this can be seen as the contour lines do not intersect at right angles. **b.** uses the method introduced in Sec. 4.6, and is analytic everywhere (apart from branch points). **c.** shows dispersion curves for temperatures varying from $\tilde{T} \in [0, 0.5]$, they are correct for $\tilde{\omega}_{\text{pl}} < 1$ while the complex solution is in the upper half-plane, but breaks down for $\tilde{\omega}_{\text{pl}} > 1$.

distribution, $n(\tilde{\epsilon})$. The particular character of each is dependent on details of their functional form. Singularities in the kernel may move around in $\tilde{\epsilon}$ space with changes in the dynamic variables \tilde{q} and $\tilde{\omega}$, whereas the singularities in the distribution are fixed. To perform analytic continuation on $\Pi[n](\tilde{q}, \tilde{\omega})$ over a complex $\tilde{\omega}$ is equivalent to evaluating the integral Eq. 4.34 over a path that doesn't cross any of the singularities as $\tilde{\omega}$ varies.

For the form of $\tilde{\Pi}'(\tilde{\epsilon})$ as given in Eqs. 4.21, there are four square-root branch point singularities located at,

$$\tilde{\epsilon}_t^s = \pm_t \frac{\tilde{\omega} \pm_s \tilde{q}}{2} , \quad (4.35)$$

with $s, t \in \{+, -\}$, and four leaves of the function, two from each of the square root terms in the numerator. The leaf of the function for the start point of the contour is set such that $\tilde{\Pi}'(\tilde{\epsilon} = 0) = 0$, this choice ensures that the polarisability reduces to its equilibrium form ($\tilde{\Pi}_1$, see Eq. 4.10) for a zero-temperature Fermi distribution, $n(\tilde{\epsilon}) = \theta(\tilde{\epsilon} - 1)$.

To solve for the dispersion relation, the wavevector \tilde{q} is scanned over real values starting from $\tilde{q} = 0$. Each possible $\tilde{\omega}(\tilde{q})$ puts the branch points $\tilde{\epsilon}_t^s$ in a different position.

4.6.1. Fermi Distribution

The first nonequilibrium plasmon dispersion to solve for is the finite temperature intrinsic quasiequilibrium, i.e. $n(\tilde{\epsilon}) = \bar{n}(\tilde{\epsilon}) = f(\tilde{\epsilon} - \tilde{\mu}, \tilde{T})$, a Fermi distribution of electrons and holes in the conduction and valence bands respectively, with matching chemical potentials.

The carrier distribution carries its own set of singularities, fixed in position in $\tilde{\epsilon}$ space. Fermi distributions have poles at the Matsubara frequencies

$$\tilde{\epsilon}_n^M = \tilde{\mu} + i(2n + 1)\pi\tilde{T} . \quad (4.36)$$

The deformation of the integration contour can be generalised to be able to pass over simple poles, so long as for each pole the contour crosses, the contribution of that pole ($2\pi i$ times the residue about the pole) is subtracted from the final result. For a Fermi distribution, the integral around an infinitesimal closed loop about each pole has the form,

$$\oint_{C_n} d\tilde{\epsilon} f(\tilde{\epsilon} - \tilde{\mu}, \tilde{T}) \tilde{\Pi}'(\tilde{\epsilon}) = -2\pi i \tilde{T} \tilde{\Pi}'(\tilde{\epsilon}_n^M), \quad (4.37)$$

which is equal to the value of the contour integral step-changes by as each pole is taken through the contour.

The movement of the singularities of the kernel along solutions to the dispersion relation, $\tilde{\epsilon}_t^s(\tilde{q}, \tilde{\omega}_{pl}(\tilde{q}))$, can be accounted for. Their imaginary part is given by $\text{Im } \tilde{\omega}/2$ (Eq. 4.35), which will be positive for plasmons with gain, and negative for loss. As in the zero temperature case, and low temperature solutions (Sec. 4.5.2), the imaginary part starts positive, for a gain region before entering the lower half-space for the Landau damping regime. In order to allow the branch singularities to enter the lower $\tilde{\epsilon}$ half-space, the original horizontal line contour (Fig. 4.10.a) can be deformed, by passing over any number of the Matsubara poles in the lower half space to give a clear area for the branch points to pass through (Fig. 4.10.b). Then for higher values of \tilde{q} , the dispersion will enter the intraband regime and the branch points $\tilde{\epsilon}_\pm^-$ will cross the imaginary axis. This space can also be opened out, once $\tilde{\omega}$ has crossed the real axis, and requires no further poles to be encircled (Fig. 4.10.c).

Following this procedure, Eq. 4.17 can be solved for to find the plasmon dispersion curves for varying temperature. Figure 4.11 plots these for suspended graphene with symmetric carrier distributions. As \tilde{T} increases, each successive curve becomes steeper. The increased steepness means that the dispersion curves stay in the gain region for shorter intervals of \tilde{q} , whilst remaining in the Landau damping regime ($\tilde{\omega} \gtrsim \tilde{q} - 1$) for longer. This manifests itself as a blueshift in the absorption peak

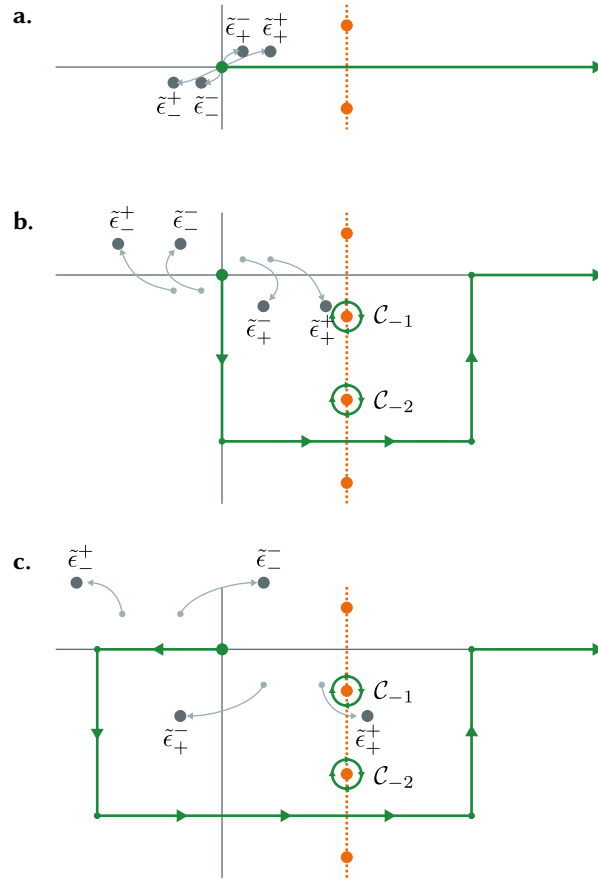


Figure 4.10: Polarisability as a complex contour integration.

The polarisability is calculated as a contour (green) in complex $\tilde{\epsilon}$ space. There are two types of singularity, branch points (grey), which move with $(\tilde{q}, \tilde{\omega})$ and poles (orange) which are fixed in place. a. is the contour for small values of \tilde{q} , evaluated over $[0, \infty)$. The contour is deformed in b. to include a number of the Matsubara poles such that the branch points can move within the lower half-space. In c. the contour is further deformed to allow the $\tilde{\epsilon}_+^-$ to move into the bottom-left quadrant.

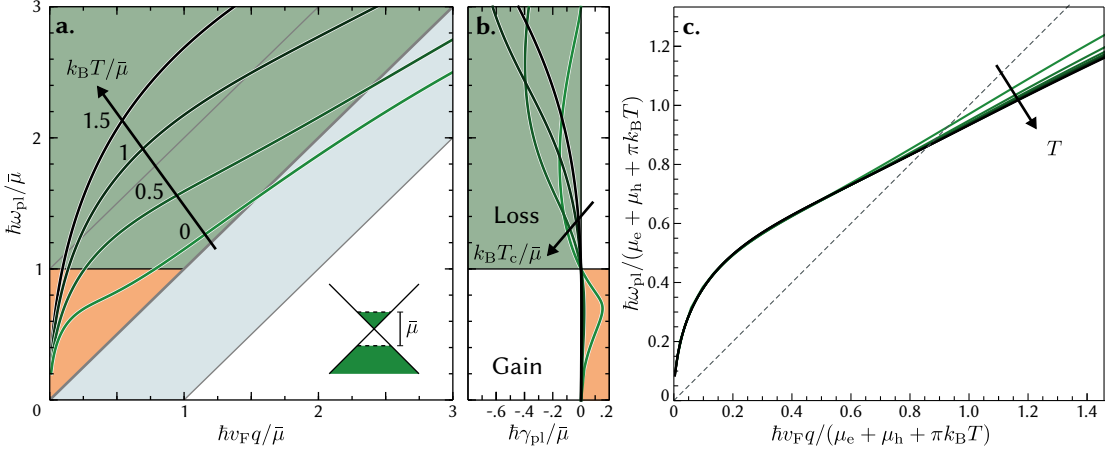


Figure 4.11: High temperature plasmon dispersion curves.

- a. Dispersion and b. loss curves of intrinsic photoinverted graphene, for temperatures varying $\tilde{T} \in [0, 1.5]$. c. Curves are rescaled by a factor $1 + \pi\tilde{T}$, they limit to a universal behaviour for increasing \tilde{T} , this is at the expense of not being able to draw regions of Landau damping and recombination.

and with the peak value of absorption increasing. Despite this, the absorption curves come out shallower for frequencies immediately above $\tilde{\omega} = 1$, as the phase-space for gain processes bleeds into this regime.

If the curves are rescaled such that $\bar{\mu} = \mu_e + \mu_h + \pi k_B T$ rather than the usual $\bar{\mu} = \mu_e + \mu_h$, then the curves begin to align on top of each other. This allows high temperature curves to be estimated without calculation from lower temperature ones.

4.6.2. Non-Fermi Distribution

Having shown the complex contour method applied to calculating the polarisability of high-temperature quasiequilibrium Fermi distributions, we turn to the question of calculating for arbitrary (isotropic) nonequilibrium carrier distributions. A case that one may wish to consider is that of a graphene sheet optically pumped by an external field. Here carriers are excited vertically from the valence to the conduction band,

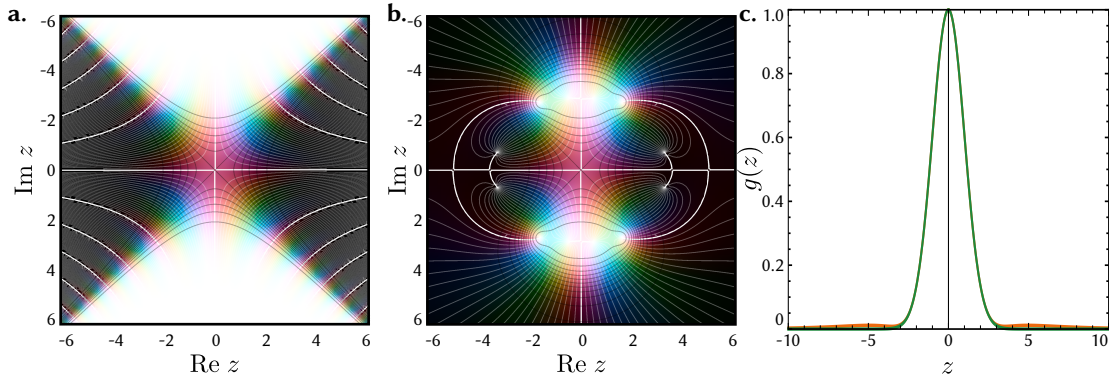


Figure 4.12: Padé approximant for a Gaussian.

- a. Complex plot (Sec. A.1) of a Gaussian. b. Its (4,8) Padé approximant, showing 4 roots and 8 poles. c. The two are compared as functions of a real variable for the Gaussian (green), and its approximant (orange) showing additional side lobes.

generating electron hole pairs in a distribution with energies centred on $\epsilon = \pm \hbar\omega_p/2$ and with a width of $\hbar\gamma_p$ [207].

A model for this distribution would be a Gaussian function, $g(z) = e^{-z^2/2}$, added to a finite temperature Fermi function background, i.e.

$$n(\epsilon) = n_0 g\left(\frac{\epsilon - \hbar\omega_p/2}{\gamma_p}\right) + f(\epsilon - \mu_s, T), \quad (4.38)$$

where n_0 is the carrier occupation number at the top of the photoinversion peak, which will be a function of the pump beam intensity and duration.

The Gaussian function is well behaved in the sense that it has no singularities in the complex plane, however it diverges super-exponentially along the imaginary axis which makes the complex contour method numerically unstable. An alternative to using the Gaussian function would be to use one of its Padé approximants. A Padé approximant is the ratio of two power series of order n and m respectively. This gives the function n roots and m simple poles in the complex plane. The Gaussian is an even function, which means its approximant should have an even number of roots. It is also strictly positive, which is to say none of these roots lie on the real axis, and indeed

since real valued functions have their roots located at complex conjugate pairs, the approximant needs to have a multiple of 4 roots to preserve this property. The number of poles is determined by similar argument, with the addition that the function should go to zero for large values of z . The asymptotic behaviour of the function is that of z^{n-m} , so by choosing ($n = 4, m = 8$), we return a strictly positive function that goes to zero with $1/z^4$. The (4, 8) Padé approximant is given as,

$$g_{4,8}(z) = \frac{1 - \frac{z^2}{6} + \frac{z^4}{120}}{1 + \frac{z^2}{3} + \frac{z^4}{20} + \frac{z^6}{240} + \frac{z^8}{5760}}, \quad (4.39)$$

which is plotted alongside the Gaussian in Fig. 4.12 in the complex plane and on the real axis and can be seen to be a good match with the exception of small side-lobes either side of the main peak. Since this approximation has introduced $m = 8$ simple poles into the complex plane, explicit care must be taken that the contour integration of Eq. 4.34 does not pass over the singularities without taking into account the residues as prescribed previously in the case of the Fermi function.

The polarisability $\Pi[n]$, calculated from Eq. 4.38 with a Padé approximant, is explored with parameter values of $\hbar\omega_p/2 = 2\bar{\mu}$, $\gamma_p = 0.175\bar{\mu}$, $\tilde{T} = 0.05$, and $\mu_e = \mu_h$ in Fig. 4.13 for peak carrier occupations between 0 and 0.5. Firstly, in a), the dimensionless conductivity is plotted for external optical excitation, i.e. $q \rightarrow 0$, $\omega \in \mathbb{R}$, where,

$$Z_0\sigma_s(\tilde{q}, \tilde{\omega}) = i\alpha_0 \frac{g}{2} \frac{\tilde{\omega}}{\tilde{q}^2} \tilde{\Pi}(\tilde{q}, \tilde{\omega}). \quad (4.40)$$

It can be seen that the real part of the conductivity, which at zero pump is flat for $\omega \gtrsim 1$ begins to dip for increased pump strength at $\omega = \omega_p$. The corresponding imaginary part is modified for all frequencies centred about this point as the refractive index changes. The conductivity drops to zero at $\omega = \omega_p$ as the sheet is pumped to transparency at $n_0 = 0.5$.

Figure 4.13.b and .c plots the plasmon dispersion and loss for this polarisability configuration for varying occupation number. The plasmon dispersion shifts every-

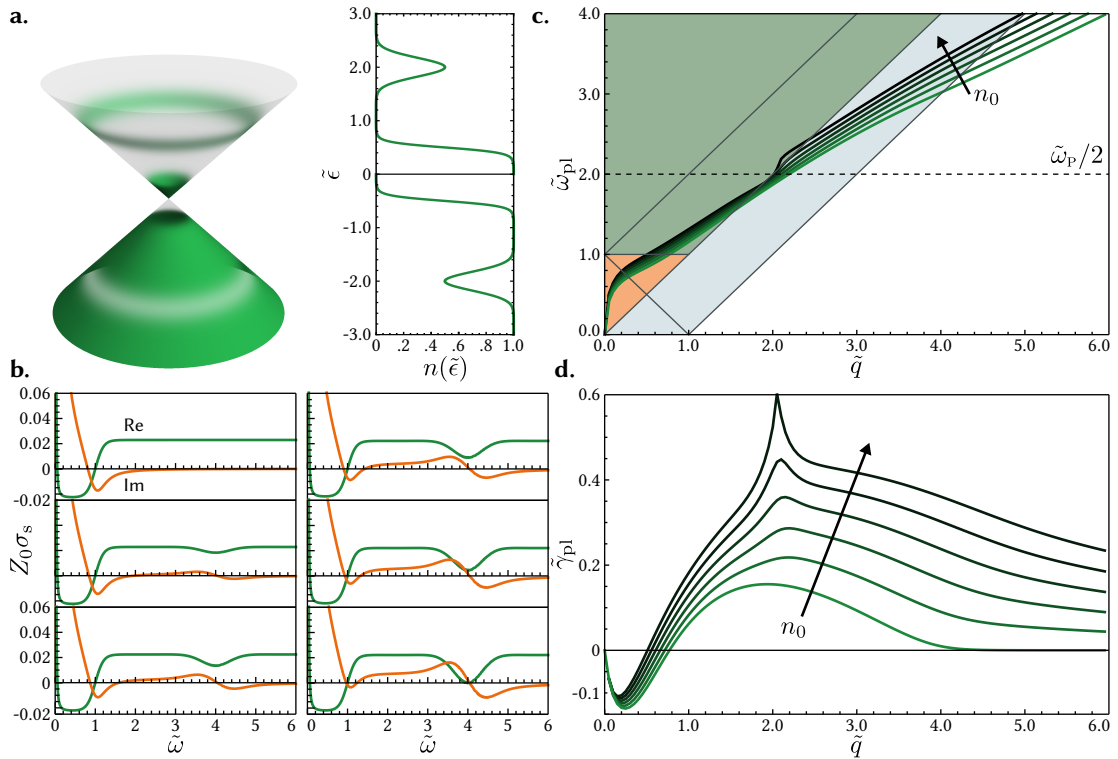


Figure 4.13: Polarisability of a hot electron distribution.

- a. A hot carrier distribution of a symmetrically excited Gaussian distribution of electrons and holes over a quasiequilibrium background simulating photoinversion
- b. The optical conductivity of this is plotted, for occupation levels n_0 , (the height of the Gaussian) between 0 and 0.5. Both real (green) and imaginary (orange) parts of the conductivity change about the pump frequency, ω_p .
- c. Plasmon dispersions and d. losses for this polarisability are also plotted. The curves noticeably kink about the pump frequency ω_p .

where, but most markedly at $\omega = \omega_p/2$ where the steepness dramatically increases. Perhaps surprisingly, there is no reduction in the plasmon loss at any frequency despite carrier pairs being available for recombination. This can be attributed to the change in refractive index morphing the plasmon dispersion to exclude it from regions where there is phase-space for stimulated recombination. This can be seen in the gain region ($\tilde{\omega} < 1$), where the gain is due to quasiequilibrium photoinversion. Here the gain decreases, not because there is any more phase-space for absorption processes, but rather that the plasmon dispersion curve has steepened in this region, leaving less phase space for the quasiequilibrium recombination processes. As the pump increases, this also induces a sharp peak of the loss around $v_F q = \omega_p/2$, again this is about where the plasmon dispersion has been perturbed the most.

This section has shown that the polarisability can be calculated as a functional of arbitrary carrier distributions as a function of a complex variable. The resulting plasmon dispersions from quasiequilibrium and a hot carrier model have been shown. A change in the carrier distribution can have a dramatic impact on the plasmon dispersion and loss, though provisionally from what has been seen, wherever there is a spread in carriers, there is an increase in the phase space opened up for absorption processes that is not matched with an increase in emission processes.

4.7. Spontaneous Emission Spectrum

There are three fundamental single particle excitation processes occurring in graphene: spontaneous emission, stimulated emission, and stimulated absorption. Spontaneous emission occurs when an electron in a higher energy state transitions to occupy an empty state of lower energy, and a plasmon is emitted in the process. In absorption, an incoming plasmon is converted into an electron-hole pair, or equivalently raises a lower energy electron into a higher unoccupied level. Whereas in stimulated emis-

sion an incoming plasmon forces an electron to transition into an unoccupied lower energy state, releasing an additional plasmon in the process that is coherent with the first. It is the processes of absorption and stimulated emission that induce Landau gain or loss in plasmons, and therefore are responsible for the imaginary part of the plasmon frequency γ_{pl} , which is the net decay rate (absorption minus emission),

$$2\gamma_{\text{pl}} = \gamma_{\text{pl}}^{\text{abs}} - \gamma_{\text{pl}}^{\text{emit}}, \quad (4.41)$$

where the factor of 2 is because γ_{pl} is a *field* decay rate, whereas $\gamma_{\text{pl}}^{\text{abs}}$ and $\gamma_{\text{pl}}^{\text{emit}}$ are *intensity* decay rates.

Spontaneous emission on the other hand does not enter into γ_{pl} but can be calculated indirectly from it by considering the rate of plasmon decay for each wavevector labelled plasmon state.

$$\frac{\partial n_{\text{pl}}(q)}{\partial t} = -\gamma_{\text{pl}}^{\text{emit}}(q)(n_{\text{pl}}(q) + 1). \quad (4.42)$$

This is a sum of a stimulated part ($n_{\text{pl}}(q)$) and a spontaneous part (+1). The spectral rate of emission within a frequency interval $[\omega, \omega + d\omega]$ is extracted by taking the partial sum over all wavevector states,

$$R_{\text{pl}}^{\text{spon}} = \frac{1}{A} \sum_{\mathbf{q}} \gamma_{\text{pl}}^{\text{emit}}(q) = \int_0^\infty d\omega G_{\text{pl}}(\omega) \quad (4.43.a)$$

$$= \int_0^\infty d\omega \frac{\partial q(\omega)}{\partial \omega} \frac{q(\omega)}{2\pi} \gamma_{\text{pl}}^{\text{emit}}(q(\omega)), \quad (4.43.b)$$

with the plasmon density of states, $D_{\text{pl}} = \frac{\partial q(\omega)}{\partial \omega} q(\omega)/2\pi$, and the *inverse* of the plasmon dispersion relation $q(\omega)$, such that $q(\omega_{\text{pl}}(q)) = q$. The plasmon spectral recombination rate areal density, G_{pl} is therefore given as the plasmon emission rate $\gamma_{\text{pl}}^{\text{emit}}$ weighted to the density of states D_{pl} for plasmons in the frequency interval $[\omega, \omega + d\omega]$. From here the particle (or hole) recombination rate may be extracted, by dividing through by the particle areal density to give the recombination rate of

electrons:

$$\Gamma_{\text{pl}}^{\text{e}} = R_{\text{pl}}^{\text{spon}} / N(\mu_{\text{e}}, T) , \quad (4.44)$$

where $N(\mu_{\text{e}}, T)$ is the particle number density in the conduction band.

It is not necessarily obvious how to extract the emission and absorption rates, $\gamma_{\text{pl}}^{\text{emit}}$ and $\gamma_{\text{pl}}^{\text{abs}}$. For zero temperature, these rates are mutually exclusive, i.e. $\gamma_{\text{pl}}^{\text{abs}} = 0$ for $\gamma_{\text{pl}}^{\text{emit}} \neq 0$ and vice-versa, since in the regions where there is phase space for absorption processes, there is none for emission. This is to say, the rates can be expressed with step functions,

$$\gamma_{\text{pl}}^{\text{emit}}(q) = -2\gamma_{\text{pl}}(q)\theta(\bar{\mu} - \hbar\omega(q)) \quad (4.45.\text{a})$$

$$\gamma_{\text{pl}}^{\text{abs}}(q) = 2\gamma_{\text{pl}}(q)\theta(\hbar\omega(q) - \bar{\mu}) . \quad (4.45.\text{b})$$

For finite temperatures and hot carrier distributions, where the regimes overlap each other, the situation is complicated. Looking at the Lindhard formula Eq. 4.7, there is a sum of distribution functions, which is equivalent to the sum of a Fermi function product for the phase space of each process.

$$n(\epsilon_{\mathbf{k}}^s) - n(\epsilon_{\mathbf{k}+\mathbf{q}}^{s'}) = \underbrace{n(\epsilon_{\mathbf{k}}^s)\left(1 - n(\epsilon_{\mathbf{k}+\mathbf{q}}^{s'})\right)}_{\text{Absorption}} - \underbrace{n(\epsilon_{\mathbf{k}+\mathbf{q}}^{s'})\left(1 - n(\epsilon_{\mathbf{k}}^s)\right)}_{\text{Stimulated Emission}} , \quad (4.46)$$

which is to say, the polarisability itself can be split up into,

$$\Pi[n](\mathbf{q}, \omega) = \Sigma^{\text{abs}}[n](\mathbf{q}, \omega) - \Sigma^{\text{emit}}[n](\mathbf{q}, \omega) , \quad (4.47)$$

with,

$$\Sigma^{\text{emit}}[n](\mathbf{q}, \omega_{\text{pl}}) = \frac{g}{A} \text{Im} \sum_{s,s'=\pm} \sum_{\mathbf{k}} M_{\mathbf{k},\mathbf{k}+\mathbf{q}}^{ss'} \frac{n(\epsilon_{\mathbf{k}+\mathbf{q}}^{s'})\left(1 - n(\epsilon_{\mathbf{k}}^s)\right)}{\epsilon_{\mathbf{k}}^s - \epsilon_{\mathbf{k}+\mathbf{q}}^{s'} + \hbar\omega_{\text{pl}} + i \times 0} , \quad (4.48)$$

and an equivalent term for Σ^{abs} .

The rates for the two individual processes can be calculated approximatively by a *Fermi's golden rule* (FGR) expression. Borrowing from the low-loss approximation

Eq. 4.9, the expression,

$$\gamma_{\text{pl}} \approx V_q \text{Im} \Pi(\omega_{\text{pl}}, q) \left/ \text{Re} \frac{\partial \varepsilon_{\text{RPA}}}{\partial \omega} \right|_{\omega=\omega_{\text{pl}}} . \quad (4.49)$$

$\Pi(\omega_{\text{pl}}, q)$ can be split into absorption and emission components⁴ using $2\gamma_{\text{pl}} = \gamma_{\text{pl}}^{\text{abs}} - \gamma_{\text{pl}}^{\text{emit}}$,

$$\gamma_{\text{pl}}^{\text{abs}} \approx 2V_q \Sigma^{\text{abs}}(\omega_{\text{pl}}, q) \left/ \text{Re} \frac{\partial \varepsilon_{\text{RPA}}}{\partial \omega} \right|_{\omega=\omega_{\text{pl}}} \quad (4.50.\text{a})$$

$$\gamma_{\text{pl}}^{\text{emit}} \approx 2V_q \Sigma^{\text{emit}}(\omega_{\text{pl}}, q) \left/ \text{Re} \frac{\partial \varepsilon_{\text{RPA}}}{\partial \omega} \right|_{\omega=\omega_{\text{pl}}} . \quad (4.50.\text{b})$$

This approximation may fair better than the low-loss approximation, since we can put in the exactly solved real part of the dispersion. This expansion will still start to break down as the Fermi line is approached, though the emission term will fare much better than the absorption since, at least for quasiequilibrium at moderate temperatures, the emission rate approaches zero before the dispersion hits the Fermi line. From here the absorption term can be derived from the exact net term as $\gamma_{\text{pl}}^{\text{abs}} = 2\gamma_{\text{pl}} + \gamma_{\text{pl}}^{\text{emit}}$.

The emission partial polarisability can be put into integrable form, assuming only interband recombination processes are significant, as,

$$\Sigma^{\text{emit}}(q, \omega) = \frac{gq^2}{8\pi\hbar} \frac{\theta(\omega - v_F q)}{\sqrt{\omega^2 - v_F^2 q^2}} \int_{-1}^{+1} du \sqrt{1-u^2} n \left(\frac{\hbar\omega + \hbar v_F qu}{2} \right) \bar{n} \left(\frac{\hbar\omega - \hbar v_F qu}{2} \right) . \quad (4.51)$$

which is derived in the appendix of [193].

The spontaneous emission is calculated and plotted in Fig. 4.14 for zero temperature quasiequilibrium graphene, exactly (red lines) and in various approximations. Since for zero temperature, Eq. 4.45 holds and G_{pl} and $\Gamma_{\text{pl}}^{\text{e}}$ can be calculated exactly [(i) in the figure] from the CFPD using the directly extracted $\gamma_{\text{pl}}(q)$. Three FGR approximations are derived by calculating $\gamma_{\text{pl}}^{\text{emit}}$ from Eq. 4.50.b, using the dispersion relations

⁴ This step is not exact either, as the polarisability Π enters into ε_{RPA} , though as we will see, it makes a good approximation.

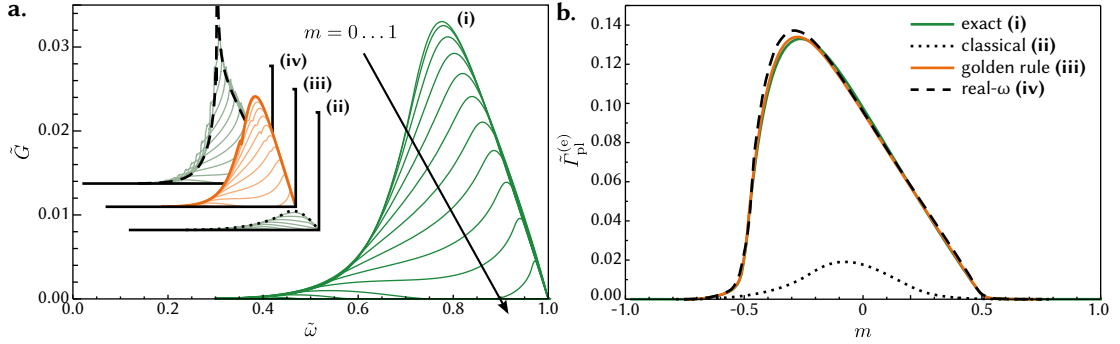


Figure 4.14: Spontaneous plasmon emission and electron recombination.

a. Plasmon spontaneous emission spectra, \tilde{G}_{pl} and b. electron recombination rates $\tilde{I}_{\text{pl}}^{\text{e}}$ at zero temperature. Exact results derived from CFPD curves (i) are plotted against approximate results derived from FGR for a classical Drude model (ii), CFPD curves (iii), and low-loss approximation. Curves are dependent on carrier imbalance, m .

$\omega_{\text{pl}}(q)$ from the classical Drude model (ii), the CFPD solution (iii), and the low-loss approximation; curves which have been shown previously in Fig. 4.2. The exact result, obtained from the CFPD will be used to test and benchmark the appropriateness of FGR solutions, which is important as regimes where exact solutions cannot be obtained are explored.

The figure plots the dimensionless quantities $\tilde{G}_{\text{pl}} = (\hbar v_F)^2 G_{\text{pl}} / \bar{\mu}^2$ and $\tilde{I}_{\text{pl}}^{\text{e}} = \hbar I_{\text{pl}}^{\text{e}} / \bar{\mu}$, which have the usual universality property⁵. Each set of curves in Fig. 4.14 a scans the spontaneous emission spectrum over $\tilde{\omega}$ for varying levels of carrier inversion m . The symmetrically inverted case $m = 0$ acts as the envelope for each of the other curves as the level of spontaneous emission drops with a reduction in inversion. The curves all vanish to zero for $\tilde{\omega} > 1$ due to there being no phase space outside this regime. Of the approximative curves, the Drude model performs the worst, being a factor of 5 slower than the exact solution. This is due to a density of states that is an order of 10 times smaller than for the other curves, despite having a raw emission rate

⁵ \tilde{G}_{pl} is scaled to the square of the energy scale $\bar{\mu}$ as it is an areal density (2D) quantity.

$\gamma_{\text{pl}}^{\text{emit}}$ that is larger comparatively. Using the low-loss approximation (iii) yields results that are the right order of magnitude, but have spurious spikes in the curves which are a result of the first order approximation overshooting when the dispersion curve passes near any branch points. The CFPD dispersion approximation yields results that are most quantitatively similar to the exact solution, though the match is not perfect and distinctive dips are also observed near where the solution passes in the vicinity of branch points.

In Fig. 4.14.d, each of the \tilde{G}_{pl} curves are integrated over frequency then scaled to the electron density to return the electron recombination rate. The equivalent procedure may be applied for holes and, due to particle-hole symmetry, can be related as $\tilde{\Gamma}_{\text{pl}}^{\text{h}}(m) = \tilde{\Gamma}_{\text{pl}}^{\text{e}}(-m)$. The resulting curves are not themselves though symmetric about $m = 0$ because for electrons, for $m > 0$ they are the majority carrier, and for $m < 0$ the minority and hence more sensitive to a change in carrier numbers. The skew to the left indicates that the rate of electron recombination is strongest when holes are the majority carrier, i.e. when for each electron, the amount of holes available to recombine with is saturated. The classical Drude limit has recombination rates a factor of 5 slower than what is predicted using the exact formalism, and with rates previously predicted in [144]. The other approximations work rather better in this picture, with any inconsistencies that were present in the spectral form having been averaged out in the recombination rate and largely matching the exact result.

In this formalism, carrier recombination rates are predicted to be a factor 5 faster than previously calculated. When using representative energy scales, e.g. $\bar{\mu} = 0.2 \text{ eV}$ yield recombination times of 34 fs (at $m = 0$).

Nonequilibrium Plasmon emission must therefore be considered as an important channel for interband carrier recombination alongside the optical phonon emission [195, 196, 197, 139] and Auger recombination channels [208, 154, 156, 158] when the

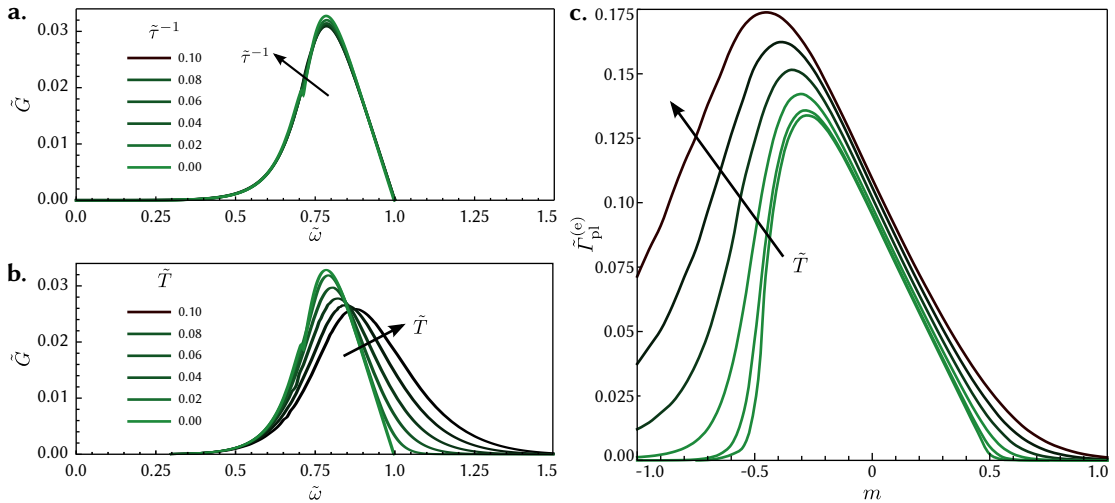


Figure 4.15: **Impact of temperature and collisions on spontaneous emission.**

Plasmon gain spectrum $\tilde{G}_{\text{pl}}(\tilde{\omega})$ for intrinsic graphene ($m = 0$) for: **a.** collision losses spanning $\tilde{\tau}^{-1} \in [0, 0.08]$, and **b.** temperatures spanning $\tilde{T}^{-1} \in [0, 0.1]$. Electron recombination rates over the same temperature range are plotted in **c** over carrier imbalance m .

dynamics of hot carriers in graphene are analysed [159, 141, 161].

4.7.1. Recombination Rates at Finite Temperature and Collision Loss

Armed with a reliable way to estimate spontaneous emission and MDF recombination rates, it remains to investigate how this changes with the inclusion of finite temperature, or collision losses.

By including collision loss and finite temperature effects, Eq. 4.45 no longer holds, as the loss rate γ_{pl} is now not entirely due to recombination, with added contributions from collision and Landau damping loss bleeding in. In this situation the FGR approximation of Eq. 4.50.b must be used. Curves for $m = 0$ (representing the envelope) are plotted in the CFPD FGR approximation for finite collision rates in Fig. 4.15.a and finite temperature in Fig. 4.15.b. In the case of collision loss, the rates hardly change

at all. This is because collision loss, although increasing the plasmon loss, is not a recombination mechanism, and therefore does not contribute in the FGR expansion. Any changes, including the smoothing out of the kink in the curve, are due to the small changes in the dispersion curve from which the FGR is calculated.

The situation for a finite temperature is quite different. The character of the emission rate $\gamma_{\text{pl}}^{\text{emit}}$ shows a blueshift as the hard edge at $\tilde{\omega} = 1$ for $T = 0$ softens out to finite values for $\tilde{\omega} > 1$ as the phase space opens, much as was the case for the stimulated emission rates (Fig. 4.8). While the peak value of spontaneous emission decreases with temperature, the spectrum as a whole broadens. This can be seen most clearly in the MDF recombination rates, which increase with temperature for all values of m . Again, when electrons are the minority carrier, their recombination rates are more sensitive to changes in temperature, with increased phase space for increased temperature.

The recombination time drops as temperature increases, from a value of 34 fs at zero temperature, as reported in the previous section, to a peak value of $1/\Gamma_{\text{pl}}^{\text{e}} = 18$ fs for $T = 230$ K and $m = -0.5$.

Summarising the results of this section, FGR approximations of the emission and absorption components of the plasmon rates have been shown. The accuracy of these is critical on using the real part of the exactly solved CFPD solution, with approximative solutions (classical Drude model, and RPA polarisability in a low-loss approximation) giving results that are either factors out, or with spurious features. The emission rate can be used to calculate the spontaneous emission rates and derived carrier recombination rates, which are found to be sensitive to temperature, but insensitive to levels of collision losses. The recombination rates are significantly faster than previously predicted and must be considered in an analysis of carrier relaxation.

4.8. Carrier Relaxation Dynamics

It was established in the previous section that spontaneous plasmon emission is an ultrafast process in photoinverted graphene, with rates exceeding that of optical phonon emission by orders of magnitude [144]. The resulting rates for carrier recombination indicate that plasmon emission may be the dominant decay channel for nonequilibrium carrier relaxation in graphene, a process that had been previously been attributed to Auger recombination (AR) [159, 158], which is subject to debate as AR processes are suppressed under RPA dynamic screening models [156, 160].

The recombination rates presented in the previous section are the instantaneous values based on a fixed carrier distribution, whereas carrier recombination will precisely seek to change the distribution over time. In order to accurately predict how *nonequilibrium plasmon emission* (NPE) affects the carrier dynamics, a time-domain study of the carrier and plasmon system becomes necessary together with additional recombination pathways such as optical phonon emission, which may interplay and seek to take heat out of the system.

For this section, the carrier system is assumed to relax instantaneously to quasiequilibrium characterised by chemical potentials μ_e and μ_h , for electrons and holes respectively in the conduction and valence bands, and a common carrier temperature T_c , which feeds into Fermi carrier distributions in each band as described in Sec. 4.4. Meanwhile the bosonic excitations, plasmons and optical phonons, are resolved by wavevector $n_\beta(\mathbf{q})$ for each species bath, β .

The carrier system's number and energy density moments, N_e , N_h , and U evolve in time as driven by an external optical excitation pump term and due to relaxation

terms that couple to the boson baths.

$$\dot{N}_e = \dot{N}_h = \dot{N}^{\text{pump}} - \dot{N}^{\text{rel}} \quad (4.52.\text{a})$$

$$\dot{U} = \dot{U}^{\text{pump}} - \dot{U}^{\text{rel}} . \quad (4.52.\text{b})$$

Carriers are always generated pairwise as an electron and a hole, which results in their rates being equal.

Assuming the system is pumped by a normally incident quasi-monochromatic, $\hbar\omega_p$, planewave with a slowly varying envelope $I(t)$, then the carrier pairs excited and energy dissipated into the system is given by,

$$\dot{N}^{\text{pump}} = \text{Re}[\sigma_s^{\text{inter}}(\omega)]|E(t)|^2/(2\hbar\omega) \quad (4.53.\text{a})$$

$$\dot{U}^{\text{pump}} = \text{Re}[\sigma_s(\omega)]|E(t)|^2/2, \quad (4.53.\text{b})$$

where $\sigma_s(\omega)$ is the optical conductivity ($q = 0$) as in Eq. 4.6, σ_s^{inter} is the contribution to the sheet conductivity from interband processes only, and $E(t)$ is the in plane component of the electric field generated from a beam with an input intensity of $I(t)$, given as,

$$|E(t)|^2 = 2Z_0 \left| \frac{1}{1 + Z_0\sigma_s(\omega)/2} \right|^2 I(t) , \quad (4.54)$$

as derived from the TMM formalism in Sec. 2.3.3.

The system relaxes according to Boltzmann collision integrals, which account for intraband scattering and interband recombination and pair generation processes. Each boson field reservoir, β , contributes to the number and energy density relaxation rates. Whereas only interband processes affect the number density, as these are the processes that produce electron-hole pairs, both inter- and intraband processes ($\lambda \in \{\text{ee}, \text{hh}, \text{eh}\}$) relax the energy density,

$$\dot{N}^{\text{rel}} = \sum_{\beta} R_{\beta} \quad (4.55.\text{a})$$

$$\dot{U}^{\text{rel}} = \sum_{\beta, \lambda} S_{\beta, \lambda} . \quad (4.55.\text{b})$$

These rates themselves are summed over wavevector resolved processes, over each band combination,

$$R_\beta = \frac{1}{A} \sum_{\mathbf{q}} r_{\beta,\text{eh}}(\mathbf{q}) \quad (4.56.\text{a})$$

$$S_{\beta,\lambda} = \frac{1}{A} \sum_{\mathbf{q}} \hbar\omega_\beta(\mathbf{q}) r_{\beta,\lambda}(\mathbf{q}) . \quad (4.56.\text{b})$$

with $r_{\beta,\lambda}(\mathbf{q})$ being the net spectral emission rate, including both stimulated and spontaneous processes,

$$r_{\beta,\lambda}(\mathbf{q}) = \gamma_{\beta,\lambda}^{\text{emit}}(\mathbf{q}) [n_\beta(\mathbf{q}) + 1] - \gamma_{\beta,\lambda}^{\text{abs}}(\mathbf{q}) n_\beta(\mathbf{q}) . \quad (4.57)$$

The bosonic fields themselves then relax via this interaction with the carrier system, but additionally through decay processes through other channels characterised by a relaxation rate $\dot{n}_\beta^{\text{rel}}(\mathbf{q})$,

$$\dot{n}_\beta = \sum_{\lambda} r_{\beta,\lambda}(\mathbf{q}) - \dot{n}_\beta^{\text{rel}}(\mathbf{q}) . \quad (4.58)$$

These additional relaxation processes can be phenomenologically modelled by a characteristic time τ_β ,

$$\dot{n}_\beta^{\text{rel}}(\mathbf{q}) = \tau_\beta^{-1} [n_\beta(\mathbf{q}) - n_\beta^{\text{eq}}(\mathbf{q}, T_0)] , \quad (4.59)$$

where $n_\beta^{\text{eq}}(\mathbf{q}, T_0)$ is the equilibrium distribution at an ambient temperature T_0 .

Initially a study of the carrier/plasmon system in isolation will be presented, then optical phonons will be included. The initial conditions for each simulation are the same; a pulse of fluence $133 \mu\text{J} / \text{cm}^2$ with frequency $\hbar\omega = 1 \text{ eV}$ is incident on ambient temperature intrinsic equilibrium graphene. During excitation, in order that each initialisation is the same, relaxation processes are turned off. This leaves the system in an inverted state with $\mu_e = \mu_h \approx 0.3 \text{ eV}$ and $T_c \approx 0.2 \text{ eV} / k_B$ (2320 K). As the system starts intrinsically doped $\mu_e = \mu_h$ and all carrier excitations are pairwise, the electron and hole chemical potentials will remain equal, i.e. a carrier imbalance of $m = 0$, throughout the simulation. The plasmon system is resolved isotropically in wavevector, i.e. $n_{\text{pl}}(\mathbf{q}) = n_{\text{pl}}(q)$.

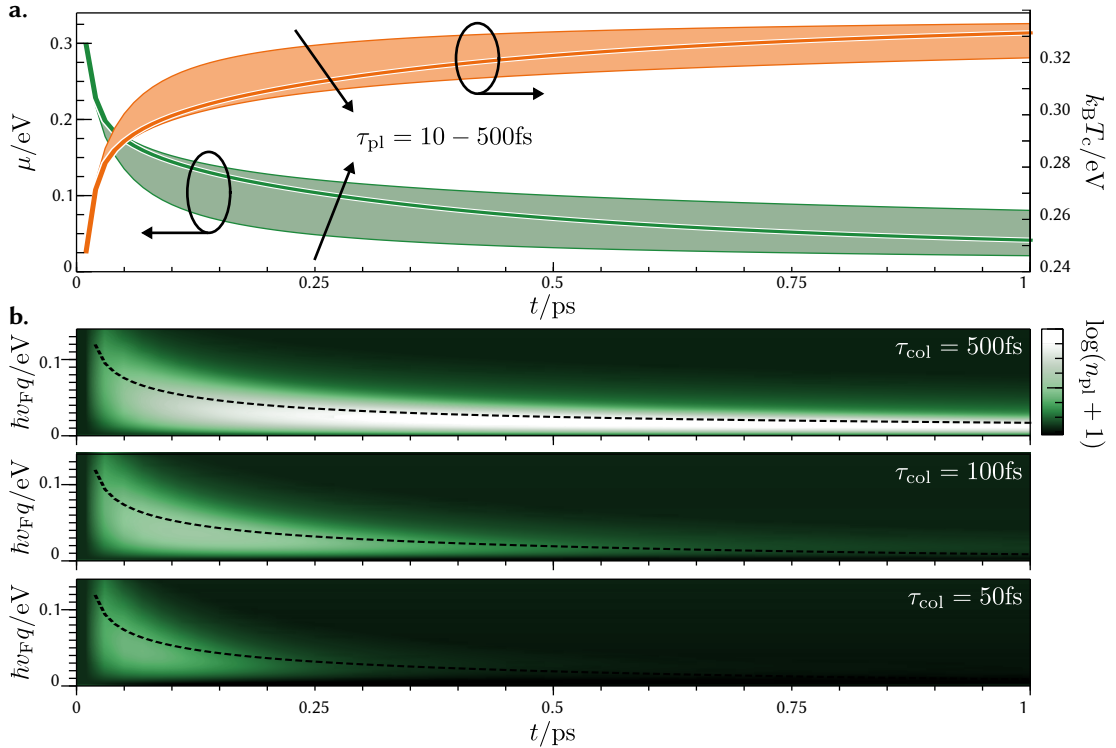


Figure 4.16: Relaxation dynamics of coupled plasmon and carrier system.

- a. Chemical potential (Green) and temperature (orange) of the carrier system relaxing over time. Solid lines are for a collision time $\tau_{\text{pl}} = 100 \text{ fs}$ while shaded areas vary from this in the range $\tau_{\text{pl}} \in [10, 500] \text{ fs}$.
- b. shows the wavevector resolved plasmon occupation $n_{\text{pl}}(q)$. Black dashed lines mark the transition from absorption to emission.

4.8.1. Relaxation Via the Plasmon Channel

The relaxation after excitation of the isolated carrier/plasmon system (without optical phonons) is considered for a range of collision rates τ_{pl} in the range [10, 500] fs. Figure 4.16 shows how, in the first 1 ps after excitation, the carrier system (a) and plasmon system (b) relaxes. There is a sharp drop in inversion in the first 50 fs as the initially empty plasmon bath is populated via interband recombination of carrier pairs. The temperature correspondingly rises in this interval, which although the energy density is dropping due to conversion to plasmons, the temperature must rise such that the highest occupied carriers still have a probability of occupation. Plasmons may only be emitted at energies below 2μ , i.e. for $\gamma_{\text{pl}}(\mathbf{q}) = 0$, above this they are reabsorbed; the Fermi-edge drops over time meaning that plasmons that were previously emitted may now be reabsorbed. This reabsorption also increases the temperature, as there are many electron-hole pair combinations that each plasmon may decay into, conserving energy and momentum, despite having been created from a single particular pair; this will seek to smear out the carrier distribution. Over the next 200 fs the recombination rates slow down as inversion is converted into temperature reducing the net emission of plasmons as in Fig. 4.11. The dropping Fermi-edge means that plasmons that had been emitted are being reabsorbed into the carrier system. This slows down the decay rate of both the energy and number density which may be described as a *plasmon emission bottleneck*. With an increasing collision loss, more plasmons are removed from the system, meaning that their energy is not being converted into electron-hole pairs, lifting the bottleneck and allowing the carrier inversion to decay more quickly. This is most obviously noticed by comparing the steepness of the outermost curves for the carrier temperature and chemical potential with inversion lingering at $\mu = 0.1$ eV for $\tau_{\text{pl}} = 500$ fs but quickly depleting at $\tau_{\text{pl}} = 10$ fs.

4.8.2. Optical Phonons

Phonons also play a role in the relaxation of a hot carrier distribution [197], being a channel for both intraband scattering [159] and interband pair generation / recombination [196]. *Longitudinal optical* (LO) and *transverse optical* (TO) phonons are the dominant channels for coupling to the carrier system. They couple about the Γ and K symmetry points, allowing intra- and inter-valley transitions respectively; about these points they are quasi-dispersion free having a single frequency. These are the ϵ_{ro} and ϵ_{ko} phonons, for which $\epsilon_{\text{ro}} = 196 \text{ meV}$, $\epsilon_{\text{ko}} = 160 \text{ meV}$. There is also an acoustic phonon that couples at the K point in this manner, ϵ_{KA} with $\epsilon_{\text{KA}} = 120 \text{ meV}$. Closed form expressions for the net spectral emission rates, as in Eq. 4.57, can be derived due to the dispersion free nature of the modes, and are presented in the supplementary material of Ref [209].

Figure 4.17.a shows how the carrier system relaxes in the presence of only the phonons, i.e. with plasmons not included. The phonons are modelled to follow a Bose-Einstein distribution with a separate temperature for each phonon species. Since each species is mono-energetic, the temperature will uniquely determine the occupation number of that species. Such description assumes an instantaneous relaxation of the phonons to be uniformly distributed over wavevector. The phonon relaxation time is assumed to be $\tau_{\text{ph}} = 2.5 \text{ ps}$ [197].

In the first 500 fs the carrier temperature drops accompanied by an increase in chemical potential and a rise in phonon temperatures. This is indicative of intraband scattering, where the number density stays the same, but energy is transferred from the carriers to phonons. Once the phonon and carrier temperatures match, they then largely follow each other, slowly decreasing as phonons are emitted from interband recombination of carriers.

Next plasmons and phonons are simulated together, the trace of carrier and phonon

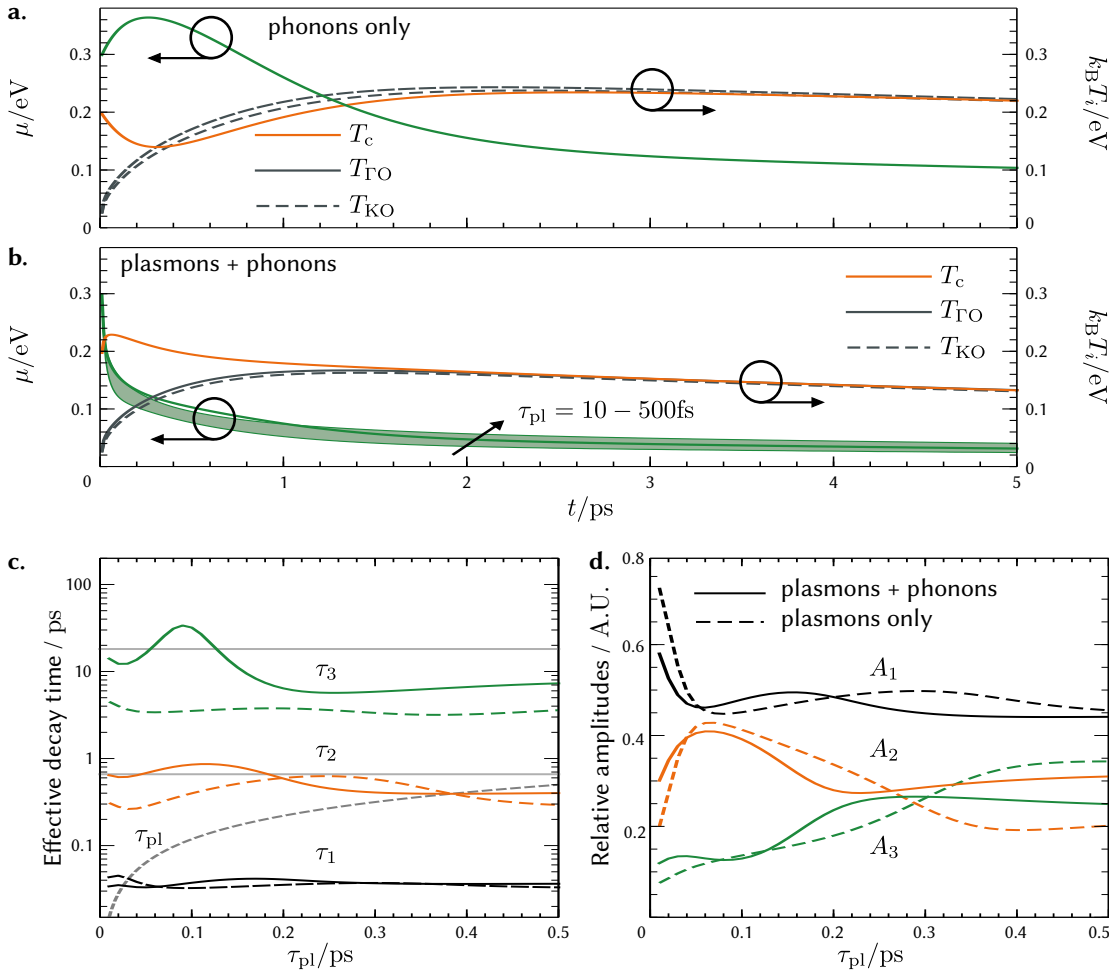


Figure 4.17: Relaxation dynamics of carriers coupled plasmons and phonons.

- Carrier temperature and chemical potential of carriers coupled only to phonons, also shows the relaxation of phonon temperatures over time.
- re-introduces plasmons, along with phonons, for varying collision times τ_{pl} .
- and d. show extracted parameters (A_i, τ_i) of a tri-exponential fit of $\mu(t)$ for plasmons in isolation, and plasmons and phonons.

configuration is given in Fig. 4.17.b. Initially inversion drops sharply as plasmons are emitted, but this is not accompanied by a sharp rise in carrier temperature, as was the case with plasmons alone, as the coupling with phonons removes excess temperature from the carrier plasma through intraband emission. Again, once the carrier and phonon temperatures have equalised after around 1 ps, the inversion slowly drains, albeit, in contrast to with phonons alone, the chemical potential has by now been significantly cut. With an increase in the plasmon decay rate, energy is removed from the system faster, though with the phonons now acting as an efficient channel to extract heat, this effect is less sensitive to the decay rate than with plasmons alone.

Further inferences can be made by examining the characteristic of the chemical potential drop in more detail. A tri-exponential function, $\mu = \mu_0 \sum_{i=1}^3 A_i \exp(-t/\tau_i)$, can be fit to the time evolution. Figure 4.17.c shows this fit for both NPE alone and NPE with phonons, as plasmon collision loss varies. The timescales that emerge (τ_1, τ_2, τ_3) separate out into distinct values that are largely independent on the collision loss. The fastest timescale, $\tau_1 \approx 0.03$ ps represents the filling of the initially empty plasmon bath via spontaneous recombination of electron-hole pairs. The amplitude, A_1 , of this timescale is steady for $\tau_{\text{pl}} > \tau_1$, though in the opposite limit, where plasmons are absorbed at a faster rate than they are created, the amplitude shoots up as most of the energy is extracted from the system in this way. The second timescale $\tau_2 \approx 0.3$ ps is associated with the conversion of inversion to temperature, by emitting plasmons below the Fermi-edge, the edge dropping, and the same plasmons re-absorbing above it. The amplitude A_2 , of this process drops as A_1 rises when plasmons are quickly dissipated for $\tau_{\text{pl}} < \tau_1$, this is because there will be no plasmons in the bath to re-absorb back into the carrier system. The final rate τ_3 represents the remaining drain of energy as the saturated plasma bath depletes. As the collision loss increases, $\tau_{\text{pl}} \gtrsim 0.2$ ps, the proportion of the inversion lost through this mechanism increases, thereby

depleting the next slowest rate amplitude A_2 . This channel is the only one whose rate is significantly affected by the inclusion of phonons, with the characteristic time τ_3 universally increasing; this can be attributed to the phonons being a separate store of energy that is passed through before exiting the system.

Overall, the dependence on collision loss only affects the dynamics significantly if it is small enough to empty the plasmon bath faster than it is filled, at $\tau_{\text{pl}} \lesssim 0.2 \text{ ps}$. The addition of phonons into the model however most strongly influences the dynamics by slowing down the decay of inversion and reducing its dependence on the plasmon relaxation rate.

This establishes that NPE acts as an efficient mechanism for the equilibration of thermal photoinverted graphene. Hot electron-hole pairs may recombine creating a plasmon, removing energy and carriers from the MDF plasma. This energy is redistributed back to the carrier system and through phonon channels to eventually be removed from the system as the plasmon bath is depleted due to electron collisions. The predictions are self-consistent and in agreement with experimental findings [141] without requiring arbitrary tuning.

4.9. Conclusions

This chapter has introduced a method of calculating the polarisability of graphene for arbitrary carrier distributions in the Dirac cone approximation. This has allowed for the calculation of the complex frequency plasmon dispersion curves, which are exact solutions of the poles of the Coulomb potential in RPA. The complex nature of the solution encodes in its imaginary part the rates of loss and gain for plasmons in regions where there is coupling through absorption and stimulated emission to the MDF plasma. By calculating the emission spectrum, this work gives indication that plasmons with gain can indeed exist in graphene under realistic conditions.

The resilience of the plasmons under conditions of collision loss, finite temperature, and chemical doping has been demonstrated. The modal loss added by the inclusion of collisions is proportional to the inverse of the collisional lifetime, whereas the effects of temperature and doping is to blueshift the frequency of the peak loss rate. The dispersion of the plasmons is largely unaffected by collisions and low temperatures, but sensitive to doping, exhibiting a critical splitting in the families of curves observed. The plasmons of hot nonequilibrium carriers are shown to have strong dependency on the carrier distribution.

Spontaneous emission, that accompanies the stimulated gain, is also described in this model. A Fermi's golden rule scheme allows for the extraction of the spontaneous plasmon emission spectrum, but also for the carrier recombination rates. These are calculated under the effects of collision, temperature, and doping. While collisions do not contribute to this channel, temperature and doping have a strong influence. The rates calculated for nonequilibrium graphene are shown to be a factor 5 times faster than previously estimated. This suggests that plasmons play a key role in the dynamics of hot carrier inversion decay, that has been observed in pump-probe and TR-ARPES experiments.

The dynamics of carrier relaxation is investigated in interaction with plasmon and phonon reservoirs. It is shown that by emitting into the plasmon channels, energy can be removed from the carrier system on 100 fs timescales, which is consistent with recent experimental results [159, 141].

Chapter 5.

Conclusion

This thesis has been themed on controlling light in two dimensions with active plasmonics. Two particular topics were focused on, stopped light lasing and gain in nonequilibrium graphene, where in both plasmons are coupled to electronic systems to exploit the stimulated emission into plasmonic channels.

The question asked of stopped light was: By controlling the dispersion relation of light in a plasmonic waveguide such that energy is brought to rest at zero group velocity within a gain medium, can a regime of lasing be entered without a cavity storing the light in a resonant mode?

Designing a structure than not only stops light, but minimises the dispersion over a large range of wavevectors, allows a wavepacket to be formed that localises over a gain medium. The localisation derives from balanced and opposing energy flows in metallic and dielectric layers that form vortices around the edges of the gain medium. Lasing is indeed shown to be possible; time domain simulations show the transition from amplified spontaneous emission to lasing via characteristic relaxation oscillations.

The dynamics of the lasing mode are unusual. Energy is localised, but the mode

Chapter 5. Conclusion

does not form a standing wave, but rather a propagating one with zero group velocity. This is analogous to a barber's pole, where the stripes are continually moving but the pole stays in place. The stopped light laser is a source of coherent plasmons that are well described with a complex wavevector. This is in contrast to the lasing mode itself which is described with complex frequencies.

From here, there are a number of avenues one may take to build on this work. Firstly, simulations have been done in 2D (one dimension parallel to the structure, x , and the other perpendicular, z). In the third (homogenised) dimension, y , emitters are coherent with each other and of equal inversion. In 3D this need not be the case. Additionally, polarisation effects that were not present in 2D become available adding extra dynamics that must be studied.

This all should lead to an experimental realisation of a stopped light structure. Theoretical models and simulations should be geared to inform the design of a structure that can be fabricated in the lab, accounting for imperfections and variations not present in the idealised model.

Turning to graphene, the question posed in the introduction can now be answered: If graphene is optically pumped such that its carriers enter a state of inversion, are plasmon modes supported and can the inversion compensate for any material losses and lead to amplification of the plasmons?

Graphene has been shown to support plasmons with gain, including under realistic conditions of finite temperature, chemical doping, and collision loss. In order to arrive at this answer a model for calculating polarisabilities for nonequilibrium carrier distributions was derived and this allowed for the calculation of complex-frequency plasmon dispersion relations which encode the gain and loss.

It has also been shown that the relaxation of hot carrier distributions is ultra-fast due to spontaneous broadband nonequilibrium emission of plasmons on a timescale

Chapter 5. Conclusion

of ~ 100 fs. This is in agreement with experimental findings that have thus far relied on theoretically suppressed Auger processes to justify the observed rates.

To build on this work, one may wish to consider multi-layer graphene or other 2D materials such as TMDS. The model for calculating nonequilibrium polarisabilities is not specific to monolayer graphene, and could be applied to such materials, and indeed to models of monolayer graphene beyond the Dirac cone approximation. This could lead to the construction of graphene based plasmonic devices, beyond suspended graphene, or graphene on a simple substrate that has been considered here.

Another extension worth considering is anisotropic excitation: When graphene is photoexcited, carriers pairs are produced with a definite momentum distribution on the cone. At present, this can not be modelled in this framework, but should be investigated in order to consider the dynamics of photoexcitation more fully.

An obvious question that arises from this thesis is can the topics of graphene and stopped light be combined to form a graphene plasmonic stopped light laser? The fast inversion relaxation and a broadband spontaneous emission of graphene make it unsuitable for lasing by itself. However, this could be mitigated by using graphene as the metallic component of an SL structure, not as the emitter, and a TMD for the semiconductor. TMDS have a finite direct bandgap which should make them ideal for such a purpose. This would allow for a stopped light laser where, not only is the mode subwavelength, but the entire device is too.

Chapter 5. Conclusion

Appendices

A.1. Plots of Functions of a Complex Variable

In this thesis, it has occasionally been necessary to plot functions of a complex variable. These functions are often difficult to visualise since they map one pair of real variables to another $f : x + iy \rightarrow u + iv$, requiring four dimensions in total for the domain and the range.

Here functions of a complex variable are plotted as 2D colour plots, where the range of the function is mapped to a colour that is plotted over the domain.

Colours are assigned such that every point on the extended complex plane $\hat{\mathbb{C}}$ (Complex numbers and the point at infinity) is uniquely coloured. Here $\hat{\mathbb{C}}$ is mapped to the Riemann sphere, defined as the points labelled with polar angles (θ, φ) on a sphere of radius $1/2$ that touches the complex plane at 0 at its base, as depicted in Fig. A.1. Points on the complex plane are mapped to the sphere by a construction where a line is drawn from the top of the sphere to a point on the plane; the point is mapped to the intersection of that line and the sphere. This is expressed more concisely as $(\theta(r), \varphi) = re^{i\varphi} \rightarrow (2 \operatorname{arccot} r, \varphi)$.

The sphere is coloured in a CIE L^{*}a^{*}b^{*} colour space, with the top point being white, the bottom black, with the saturation maximal around the equator (representing unit

Appendix 1. Plots of Functions of a Complex Variable

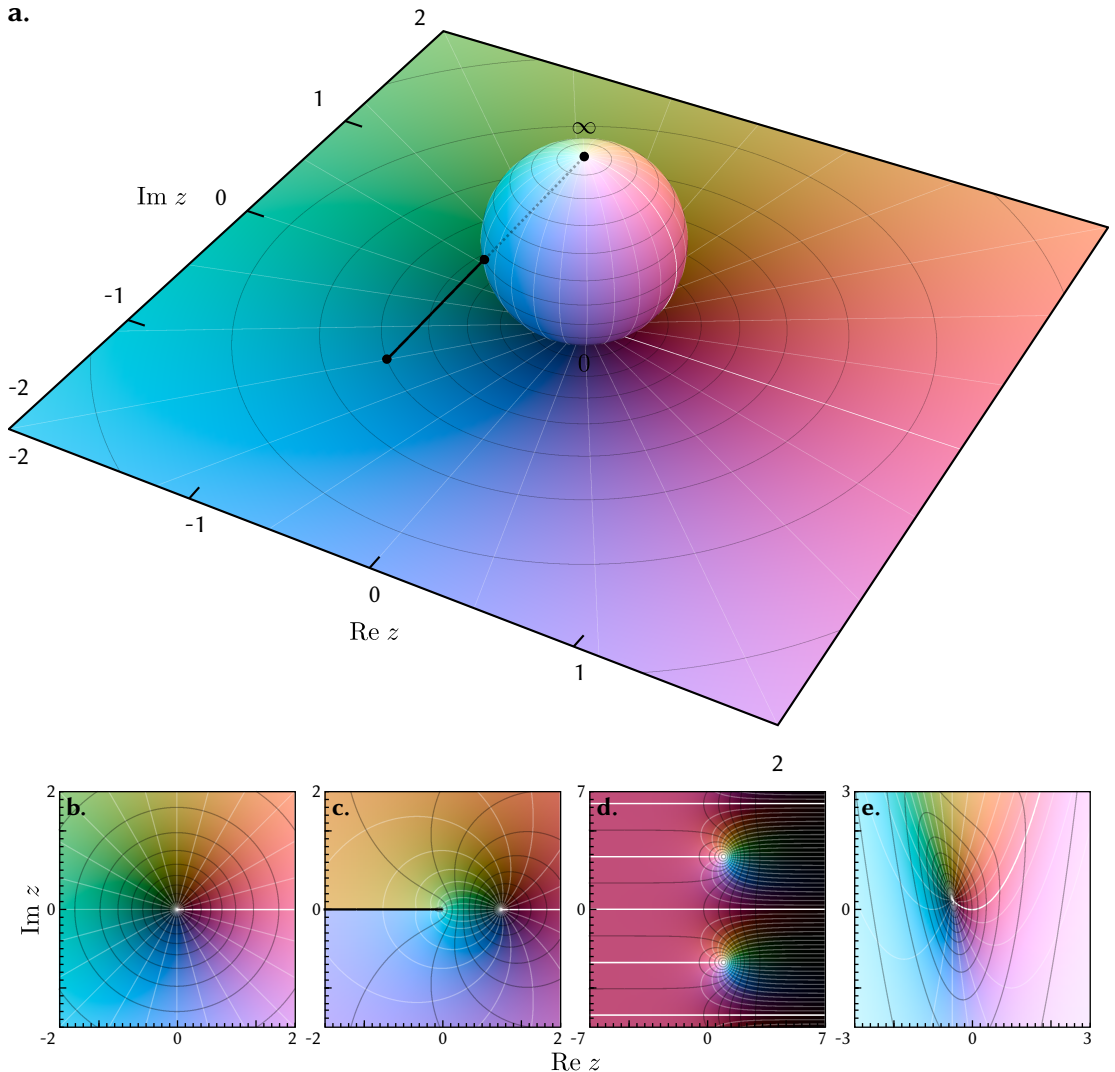


Figure A.1: Riemann sphere and complex plots.

- a. projection of the Riemann sphere onto the complex plane, each point on the sphere is assigned a unique colour, which maps to the extended complex plane.
- b, c, d, e. show complex plots of the following functions:
 - b. Identity function, $f(z) = z$, zeros show in black as sources of contour lines.
 - c. Logarithm, $f(z) = \log z$, note the branch cut along the negative real axis.
 - d. Fermi Function, $f(z) = (1 + \exp(z - 1))^{-1}$, poles here are shown in white and are sinks of contour lines.
 - e. Non-analytic function, $f(x + iy) = 1 + 2x + iy - ix^2$. Non-analytic functions are not conformal maps in the complex plane, producing contours that do not intersect at right angles.

complex numbers). The phase maps to the hue of the colour, with red being real positive numbers. The *lab* colour space has the advantage that it is “perceptually uniform”, which is to say that colours that vary only by hue, look the same brightness and saturation to a human eye. This will avoid spurious bright bands that appear in an sRGB colour space.

In the plots, contours are drawn for constant amplitude in black, and constant phase in white. Analytic functions are conformal maps - they preserve angles, therefore plots of analytic functions will have their contours intersect at right-angles (except at singular points and zeros, and points of zero derivative). In such a depiction, roots and poles are sources and sinks of contours of constant phase, and are circled by contours of constant amplitude, with roots being a black point, and poles being a white point. Branch points are drawn in this plot as thicker black lines. This is depicted in examples in Fig. A.1 in addition to a function that is not analytic hence not a conformal map.

A.2. Branches of the Polarisability Function

The dimensionless polarisability of zero temperature doped graphene, given in Eq. 4.10, is a multi-valued function of a complex variable. The function, as given, has branch cuts, and a straight evaluation will return the principal branch. In the analysis of Sec. 4.2.1, it can be required that the function needs to be analytically continued over a branch cut.

Here the functions $\tilde{\Pi}_1$, $\tilde{\Pi}'$, and $\tilde{\Pi}_0$ are presented as functions of a complex $\tilde{\omega}$ for constant $\tilde{\mathbf{q}}$, with the additional dependence of a branch parameter ξ , which is a list of integers.

The original functions are,

$$\tilde{\Pi}_1(\tilde{\mathbf{q}}, \tilde{\omega}) = -4 + \tilde{q}^2 \frac{G^+(\frac{2+\tilde{\omega}}{\tilde{q}}) + G^-(\frac{2-\tilde{\omega}}{\tilde{q}})}{2\sqrt{\tilde{q}^2 - \tilde{\omega}^2}} \quad (\text{A.1.a})$$

$$\tilde{\Pi}'(\tilde{\epsilon}; \tilde{\mathbf{q}}, \tilde{\omega}) = -4 + 2 \frac{G'(\frac{\tilde{\omega}+2\tilde{\epsilon}}{\tilde{q}}) + G'(\frac{\tilde{\omega}-2\tilde{\epsilon}}{\tilde{q}})}{G'(\frac{\tilde{\omega}}{\tilde{q}})} \quad (\text{A.1.b})$$

$$\tilde{\Pi}_0(\tilde{\mathbf{q}}, \tilde{\omega}) = -\frac{\tilde{q}}{2} \frac{\pi}{G'(\frac{\tilde{\omega}}{\tilde{q}})}, \quad (\text{A.1.c})$$

with,

$$G^\pm(z) = z\sqrt{1-z^2} \pm i \operatorname{arccosh}(z) \quad (\text{A.2.a})$$

$$G'(z) = \sqrt{1-z^2}. \quad (\text{A.2.b})$$

The branch cuts originate from square-root and logarithmic ($\operatorname{arccosh}$) branch point singularities.

Redefining the auxiliary functions as,

$$G'_{m,n}(z) = e^{i\pi/2(n+m)} \sqrt{e^{-i\pi(n+1/2)}(z-1)} \sqrt{e^{-i\pi(m+1/2)}(z+1)} \quad (\text{A.3.a})$$

$$G_{m,n,p}(z) = zG'_{m,n}(z) + i \log(e^{-i\pi(p+1/2)}(z + iG'_{m,n}(z))) - \pi p. \quad (\text{A.3.b})$$

sets each branch cut to be angled vertically downwards along the negative imaginary axis. m controls the branch cut at $z = -1$ and n at $z = +1$. By incrementing or decrementing this value, the branch is rotated counter-clockwise 180° . p controls the branch of the logarithm, is set such that it's branch cut is not exposed, but is rather hidden in the other leaf of the square root.

The polarisability functions can then be set such that all the branch cuts point down-

wards in $\tilde{\omega}$. In the general case, this is controlled by eight integers:

$$\tilde{H}_1(\tilde{\mathbf{q}}, \tilde{\omega}; \xi) = -4 + \tilde{q} \frac{G_{\xi_1, \xi_2, \xi_3}\left(\frac{\tilde{\omega}+2}{\tilde{q}}\right) - G_{\xi_6, \xi_7, \xi_8}\left(\frac{\tilde{\omega}-2}{\tilde{q}}\right) - \pi}{2G'_{\xi_4, \xi_5}\left(\frac{\tilde{\omega}}{\tilde{q}}\right)} \quad (\text{A.4.a})$$

$$\tilde{H}'(\tilde{\epsilon}; \tilde{\mathbf{q}}, \tilde{\omega}; \xi) = -4 + 2 \frac{G'_{\xi_1, \xi_2}\left(\frac{\tilde{\omega}+2\tilde{\epsilon}}{\tilde{q}}\right) + G'_{\xi_6, \xi_7}\left(\frac{\tilde{\omega}-2\tilde{\epsilon}}{\tilde{q}}\right)}{G'_{\xi_4, \xi_5}\left(\frac{\tilde{\omega}}{\tilde{q}}\right)} \quad (\text{A.4.b})$$

$$\tilde{H}_0(\tilde{\mathbf{q}}, \tilde{\omega}; \xi) = -\frac{\pi \tilde{q}}{2G'_{\xi_4, \xi_5}\left(\frac{\tilde{\omega}}{\tilde{q}}\right)}. \quad (\text{A.4.c})$$

As with the auxiliary G functions, incrementing ξ_i will rotate its associated branch by 180° counter-clockwise. When tracing roots, each time the root moves from the upper half-space to the lower or vice-versa, each branch cut should be determined to rotate either clockwise or counter-clockwise such that it does not cross over the root.

Appendix 2. Branches of the Polarisability Function

References

- [1] J. A. Dionne, L. A. Sweatlock, M. T. Sheldon, A. P. Alivisatos, and H. A. Atwater, “Silicon-Based Plasmonics for On-Chip Photonics,” *IEEE Journal of Selected Topics in Quantum Electronics*, vol. 16, no. 1, pp. 295–306, 2010.
- [2] A. V. Zayats and I. I. Smolyaninov, “Near-field photonics: surface plasmon polaritons and localized surface plasmons,” *Journal of Optics A: Pure and Applied Optics*, vol. 5, no. 4, p. S16, 2003.
- [3] D. K. Gramotnev and S. I. Bozhevolnyi, “Plasmonics beyond the diffraction limit,” *Nat Photon*, vol. 4, pp. 83–91, feb 2010.
- [4] K. F. MacDonald, Z. L. Samson, M. I. Stockman, and N. I. Zheludev, “Ultrafast active plasmonics,” *Nat Photon*, vol. 3, pp. 55–58, jan 2009.
- [5] O. Hess, J. B. Pendry, S. A. Maier, R. F. Oulton, J. M. Hamm, and K. L. Tsakmakidis, “Active nanoplasmonic metamaterials,” *Nature Materials*, vol. 11, pp. 573–584, jun 2012.
- [6] J. N. Anker, W. P. Hall, O. Lyandres, N. C. Shah, J. Zhao, and R. P. Van Duyne, “Biosensing with plasmonic nanosensors,” *Nature Materials*, vol. 7, pp. 442–453, jun 2008.
- [7] L. Cao and M. L. Brongersma, “Active Plasmonics: Ultrafast developments,” *Nat Photon*, vol. 3, pp. 12–13, jan 2009.

References

- [8] L. Tang, S. E. Kocabas, S. Latif, A. K. Okyay, D.-S. Ly-Gagnon, K. C. Saraswat, and D. A. B. Miller, “Nanometre-scale germanium photodetector enhanced by a near-infrared dipole antenna,” *Nat Photon*, vol. 2, pp. 226–229, apr 2008.
- [9] M. Kauranen and A. V. Zayats, “Nonlinear plasmonics,” *Nat Photon*, vol. 6, pp. 737–748, nov 2012.
- [10] Z. Jacob and V. M. Shalaev, “Plasmonics Goes Quantum,” *Science*, vol. 334, pp. 463–464, oct 2011.
- [11] M. S. Tame, K. R. McEnergy, S. K. Ozdemir, J. Lee, S. A. Maier, and M. S. Kim, “Quantum plasmonics,” *Nat Phys*, vol. 9, pp. 329–340, jun 2013.
- [12] J. B. Pendry, “Negative Refraction Makes a Perfect Lens,” *Physical Review Letters*, vol. 85, pp. 3966–3969, oct 2000.
- [13] H. Lee, Y. Xiong, N. Fang, W. Srituravanich, S. Durant, M. Ambati, C. Sun, and X. Zhang, “Realization of optical superlens imaging below the diffraction limit,” *New Journal of Physics*, vol. 7, no. 1, p. 255, 2005.
- [14] A. Poddubny, I. Iorsh, P. Belov, and Y. Kivshar, “Hyperbolic metamaterials,” *Nat Photon*, vol. 7, pp. 948–957, dec 2013.
- [15] A. Silva, F. Monticone, G. Castaldi, V. Galdi, A. Alù, and N. Engheta, “Performing Mathematical Operations with Metamaterials,” *Science*, vol. 343, pp. 160–163, jan 2014.
- [16] J. B. Pendry, D. Schurig, and D. R. Smith, “Controlling electromagnetic fields.,” *Science (New York, N.Y.)*, vol. 312, pp. 1780–2, jun 2006.
- [17] U. Leonhardt, “Optical conformal mapping.,” *Science (New York, N.Y.)*, vol. 312, pp. 1777–80, jun 2006.
- [18] I. Radko, V. Volkov, J. Beermann, A. Evlyukhin, T. Søndergaard, A. Boltasseva, and S. Bozhevolnyi, “Plasmonic metasurfaces for waveguiding and field enhancement,” *Laser & Photonics Review*, vol. 3, pp. 575–590, nov 2009.

References

- [19] P. M. Z. Davies, J. M. Hamm, Y. Sonneneck, S. A. Maier, and O. Hess, “Plasmonic Nanogap Tilings: Light-Concentrating Surfaces for Low-Loss Photonic Integration,” *ACS Nano*, vol. 7, pp. 7093–7100, aug 2013.
- [20] J. A. Dionne, K. Diest, L. A. Sweatlock, and H. A. Atwater, “PlasMOStor: A Metal–Oxide–Si Field Effect Plasmonic Modulator,” *Nano Letters*, vol. 9, pp. 897–902, feb 2009.
- [21] K. S. Novoselov, D. Jiang, F. Schedin, T. J. Booth, V. V. Khotkevich, S. V. Morozov, and A. K. Geim, “Two-dimensional atomic crystals.” *Proceedings of the National Academy of Sciences of the United States of America*, vol. 102, pp. 10451–3, jul 2005.
- [22] K. S. Novoselov, A. K. Geim, S. V. Morozov, D. Jiang, Y. Zhang, S. V. Dubonos, I. V. Grigorieva, and A. A. Firsov, “Electric field effect in atomically thin carbon films.” *Science*, vol. 306, pp. 666–9, oct 2004.
- [23] K. F. Mak, C. Lee, J. Hone, J. Shan, and T. F. Heinz, “Atomically Thin MoS₂: A New Direct-Gap Semiconductor,” *Physical Review Letters*, vol. 105, p. 136805, sep 2010.
- [24] A. Nagashima, N. Tejima, Y. Gamou, T. Kawai, and C. Oshima, “Electronic Structure of Monolayer Hexagonal Boron Nitride Physisorbed on Metal Surfaces,” *Physical Review Letters*, vol. 75, pp. 3918–3921, nov 1995.
- [25] P. Bharadwaj and L. Novotny, “Optoelectronics in Flatland,” *Optics and Photonics News*, vol. 26, no. 7, pp. 24–31, 2015.
- [26] S. A. Maier, *Plasmonics: Fundamentals And Applications*. Springer, 2007.
- [27] D. J. Griffiths, *Introduction to Electrodynamics*. Always learning, Pearson, fourth edi ed., 2013.
- [28] P. Kinsler, “How to be causal: time, spacetime and spectra,” *European Journal of Physics*, vol. 32, no. 6, p. 1687, 2011.

References

- [29] K. Yee, “Numerical solution of initial boundary value problems involving maxwell’s equations in isotropic media,” 1966.
- [30] A. Taflove, *Computational electrodynamics: the finite-difference time-domain method*. Antennas and Propagation Library, Artech House, 1995.
- [31] W. M. Spears, *Evolutionary Algorithms: The Role of Mutation and Recombination*. Natural Computing Series, Springer Berlin Heidelberg, 2000.
- [32] M. Choi, S. H. Lee, Y. Kim, S. B. Kang, J. Shin, M. H. Kwak, K.-Y. Kang, Y.-H. Lee, N. Park, and B. Min, “A terahertz metamaterial with unnaturally high refractive index,” *Nature*, vol. 470, pp. 369–373, feb 2011.
- [33] J. B. Khurgin, “Optical buffers based on slow light in electromagnetically induced transparent media and coupled resonator structures: comparative analysis,” *Journal of the Optical Society of America B*, vol. 22, no. 5, pp. 1062–1074, 2005.
- [34] L. V. Hau, S. E. Harris, Z. Dutton, and C. H. Behroozi, “Light speed reduction to 17 metres per second in an ultracold atomic gas,” *Nature*, vol. 397, pp. 594–598, feb 1999.
- [35] C. Liu, Z. Dutton, C. H. Behroozi, and L. V. Hau, “Observation of coherent optical information storage in an atomic medium using halted light pulses,” *Nature*, vol. 409, pp. 490–493, jan 2001.
- [36] M. D. Lukin and A. Imamoglu, “Controlling photons using electromagnetically induced transparency,” *Nature*, vol. 413, pp. 273–276, sep 2001.
- [37] R. W. Boyd and D. J. Gauthier, “Controlling the velocity of light pulses,” *Science*, vol. 326, pp. 1074–1077, 2009.
- [38] M. Ibanescu, “Anomalous dispersion relations by symmetry breaking in axially uniform waveguides,” *Phys. Rev. Lett.*, vol. 92, p. 63903, 2004.
- [39] M. F. Yanik and S. Fan, “Stopping Light All Optically,” *Physical Review Letters*, vol. 92, p. 83901, feb 2004.

References

- [40] M. Ibanescu, S. G. Johnson, D. Roundy, Y. Fink, and J. D. Joannopoulos, “Microcavity confinement based on an anomalous zero group-velocity waveguide mode,” *Opt. Lett.*, vol. 30, pp. 552–554, 2005.
- [41] S. Zhang, D. A. Genov, Y. Wang, M. Liu, and X. Zhang, “Plasmon-Induced Transparency in Metamaterials,” *Physical Review Letters*, vol. 101, p. 47401, jul 2008.
- [42] N. Papasimakis, V. A. Fedotov, N. I. Zheludev, and S. L. Prosvirnin, “Metamaterial Analog of Electromagnetically Induced Transparency,” *Physical Review Letters*, vol. 101, p. 253903, dec 2008.
- [43] Y. A. Vlasov, M. O’Boyle, H. F. Hamann, and S. J. McNab, “Active control of slow light on a chip with photonic crystal waveguides.”, *Nature*, vol. 438, pp. 65–9, nov 2005.
- [44] T. F. Krauss, “Slow light in photonic crystal waveguides,” *J. Phys. D Appl. Phys.*, vol. 40, p. 2666, 2007.
- [45] T. Baba, “Slow light in photonic crystals,” *Nat. Photon.*, vol. 2, pp. 465–473, aug 2008.
- [46] P.-C. Ku, F. Sedgwick, C. J. Chang-Hasnain, P. Palinginis, T. Li, H. Wang, S.-W. Chang, and S.-L. Chuang, “Slow light in semiconductor quantum wells.,” *Optics letters*, vol. 29, pp. 2291–3, oct 2004.
- [47] P. R. Berman, “Goos-Hänchen shift in negatively refractive media,” *Phys. Rev. E*, vol. 66, p. 67603, dec 2002.
- [48] K. L. Tsakmakidis, A. D. Boardman, and O. Hess, “‘Trapped rainbow’ storage of light in metamaterials,” *Nature*, vol. 450, pp. 397–401, nov 2007.
- [49] E. I. Kirby, J. M. Hamm, T. W. Pickering, K. L. Tsakmakidis, and O. Hess, “Evanescent gain for slow and stopped light in negative refractive index heterostructures,” *Physical Review B*, vol. 84, p. 41103, jul 2011.
- [50] S. Mookherjea and A. Oh, “Effect of disorder on slow light velocity in optical slow-wave structures,” *Optics Letters*, vol. 32, no. 3, pp. 289–291, 2007.

References

- [51] R. J. P. Engelen, D. Mori, T. Baba, and L. Kuipers, “Two Regimes of Slow-Light Losses Revealed by Adiabatic Reduction of Group Velocity,” *Physical Review Letters*, vol. 101, p. 103901, sep 2008.
- [52] D. R. Smith, J. B. Pendry, and M. C. K. Wiltshire, “Metamaterials and negative refractive index,” *Science (New York, N.Y.)*, vol. 305, pp. 788–92, aug 2004.
- [53] S. Zhang, W. Fan, K. J. Malloy, S. R. J. Brueck, N. C. Panoiu, and R. M. Osgood, “Near-infrared double negative metamaterials,” *Optics express*, vol. 13, pp. 4922–30, jun 2005.
- [54] J. Valentine, S. Zhang, T. Zentgraf, E. Ulin-Avila, D. A. Genov, G. Bartal, and X. Zhang, “Three-dimensional optical metamaterial with a negative refractive index,” *Nature*, vol. 455, pp. 376–9, sep 2008.
- [55] M. Stockman, “Criterion for Negative Refraction with Low Optical Losses from a Fundamental Principle of Causality,” *Physical Review Letters*, vol. 98, pp. 1–4, apr 2007.
- [56] P. Kinsler and M. McCall, “Causality-Based Criteria for a Negative Refractive Index Must Be Used With Care,” *Physical Review Letters*, vol. 101, pp. 1–4, oct 2008.
- [57] A. Karalis, E. Lidorikis, M. Ibanescu, J. D. Joannopoulos, and M. Soljačić, “Surface-Plasmon-Assisted Guiding of Broadband Slow and Subwavelength Light in Air,” *Physical Review Letters*, vol. 95, p. 63901, aug 2005.
- [58] K. L. Tsakmakidis, T. W. Pickering, J. M. Hamm, A. F. Page, and O. Hess, “Completely Stopped and Dispersionless Light in Plasmonic Waveguides,” *Physical Review Letters*, vol. 112, p. 167401, apr 2014.
- [59] P. Yao, C. Van Vlack, A. Reza, M. Patterson, M. M. Dignam, and S. Hughes, “Ultrahigh Purcell factors and Lamb shifts in slow-light metamaterial waveguides,” *Physical Review B*, vol. 80, p. 195106, nov 2009.

References

- [60] A. Franken, “Generation of Optical Harmonics,” *Physical Review Letters*, vol. 7, no. 1, pp. 118–120, 1961.
- [61] J. R. Lakowicz, “Radiative decay engineering 3. Surface plasmon-coupled directional emission,” *Analytical biochemistry*, vol. 324, pp. 153–169, jan 2004.
- [62] Y. Fu, J. Zhang, and J. R. Lakowicz, “Metallic-Nanostructure-Enhanced Fluorescence of Single Flavin Cofactor and Single Flavoenzyme Molecules,” *The journal of physical chemistry. C, Nanomaterials and interfaces*, vol. 115, pp. 7202–7208, mar 2011.
- [63] A. Aubry, D. Y. Lei, A. I. Fernández-Domínguez, Y. Sonnenaud, S. A. Maier, and J. B. Pendry, “Plasmonic Light-Harvesting Devices over the Whole Visible Spectrum,” *Nano Letters*, vol. 10, pp. 2574–2579, jul 2010.
- [64] M. S. Jang and H. A. Atwater, “Plasmonic Rainbow Trapping Structures for Light Localization and Spectrum Splitting,” *Physical Review Letters*, vol. 107, p. 207401, nov 2011.
- [65] D. M. Callahan, J. N. Munday, and H. A. Atwater, “Solar Cell Light Trapping beyond the Ray Optic Limit,” *Nano Letters*, vol. 12, pp. 214–218, jan 2012.
- [66] R. Zhang, S. R. Garner, and L. V. Hau, “Creation of Long-Term Coherent Optical Memory via Controlled Nonlinear Interactions in Bose-Einstein Condensates,” *Physical Review Letters*, vol. 103, p. 233602, dec 2009.
- [67] J. T. Mok and B. J. Eggleton, “Photonics: Expect more delays,” *Nature*, vol. 433, pp. 811–812, feb 2005.
- [68] A. J. Kenyon, C. E. Chryssou, C. W. Pitt, T. Shimizu-Iwayama, D. E. Hole, N. Sharma, and C. J. Humphreys, “Luminescence from erbium-doped silicon nanocrystals in silica: Excitation mechanisms,” *Journal of Applied Physics*, vol. 91, no. 1, 2002.
- [69] E. Plum, V. A. Fedotov, P. Kuo, D. P. Tsai, and N. I. Zheludev, “Towards the lasing

References

- spaser: controlling metamaterial optical response with semiconductor quantum dots,” *Optics Express*, vol. 17, no. 10, pp. 8548–8551, 2009.
- [70] H. Carrère, X. Marie, L. Lombez, and T. Amand, “Optical gain of InGaAsN/InP quantum wells for laser applications,” *Applied Physics Letters*, vol. 89, no. 18, pp. –, 2006.
- [71] P. Sperber, W. Spangler, B. Meier, and A. Penzkofer, “Experimental and theoretical investigation of tunable picosecond pulse generation in longitudinally pumped dye laser generators and amplifiers,” *Optical and Quantum Electronics*, vol. 20, no. 5, pp. 395–431, 1988.
- [72] O. Painter, “Two-dimensional photonic band-gap defect mode laser,” *Science*, vol. 284, pp. 1819–1821, 1999.
- [73] H. Altug, D. Englund, and J. Vučković, “Ultrafast photonic crystal nanocavity laser,” *Nature Physics*, vol. 2, no. 7, pp. 484–488, 2006.
- [74] K. Iga, F. Koyama, and S. Kinoshita, “Surface emitting semiconductor lasers,” *IEEE J. Quantum Electron.*, vol. 24, pp. 1845–1855, 1988.
- [75] S. L. McCall, A. F. J. Levi, R. E. Slusher, S. J. Pearton, and R. A. Logan, “Whispering-gallery mode microdisk lasers,” *Appl. Phys. Lett.*, vol. 60, pp. 289–291, 1992.
- [76] K. J. Vahala, “Optical microcavities,” *Nature*, vol. 424, pp. 839–846, 2003.
- [77] H. Cao, “Lasing in random media,” *Waves in Random Media*, vol. 13, pp. R1–R39, jul 2003.
- [78] D. S. Wiersma, “The physics and applications of random lasers,” *Nat Phys*, vol. 4, pp. 359–367, may 2008.
- [79] S. C. Bloch, “Eighth velocity of light,” *American Journal of Physics*, vol. 45, pp. 538–549, jun 1977.

References

- [80] A. Reza, M. M. Dignam, and S. Hughes, “Can light be stopped in realistic metamaterials?” *Nature*, vol. 455, pp. E10–E11, oct 2008.
- [81] G. V. Naik, V. M. Shalaev, and A. Boltasseva, “Alternative plasmonic materials: beyond gold and silver,” *Adv. Mater.*, vol. 25, pp. 3264–3294, 2013.
- [82] M. A. Noginov, L. Gu, J. Livenere, G. Zhu, A. K. Pradhan, R. Mundle, M. Bahoura, Y. A. Barnakov, and V. A. Podolskiy, “Transparent conductive oxides: Plasmonic materials for telecom wavelengths,” *Applied Physics Letters*, vol. 99, no. 2, p. 021101, 2011.
- [83] M. Khajavikhan, A. Simic, M. Katz, J. H. Lee, B. Slutsky, A. Mizrahi, V. Lomakin, and Y. Fainman, “Thresholdless nanoscale coaxial lasers,” *Nature*, vol. 482, pp. 204–207, feb 2012.
- [84] E. N. Economou, “Surface plasmons in thin films,” *Phys. Rev.*, vol. 182, pp. 539–554, 1969.
- [85] A. Karalis, J. Joannopoulos, and M. Soljačić, “Plasmonic-dielectric systems for high-order dispersionless slow or stopped subwavelength light,” *Phys. Rev. Lett.*, vol. 103, p. 43906, 2009.
- [86] T. W. Pickering, J. M. Hamm, A. F. Page, S. Wuestner, and O. Hess, “Cavity-free plasmonic nanolasing enabled by dispersionless stopped light,” *Nature Communications*, vol. 5, p. 4972, sep 2014.
- [87] A. Otto, “Excitation of nonradiative surface plasma waves in silver by method of frustrated total reflection,” *Zeitschrift Fur Physik*, vol. 216, no. 4, pp. 398–&, 1968.
- [88] R. H. Ritchie, E. T. Arakawa, J. J. Cowan, and R. N. Hamm, “Surface-Plasmon Resonance Effect in Grating Diffraction,” *Physical Review Letters*, vol. 21, pp. 1530–1533, nov 1968.
- [89] G. I. Stegeman, R. F. Wallis, and A. A. Maradudin, “Excitation of surface polaritons by end-fire coupling,” *Optics Letters*, vol. 8, no. 7, pp. 386–388, 1983.

References

- [90] S. Wuestner, A. Pusch, K. L. Tsakmakidis, J. M. Hamm, and O. Hess, “Overcoming Losses with Gain in a Negative Refractive Index Metamaterial,” *Physical Review Letters*, vol. 105, p. 127401, sep 2010.
- [91] A. Pusch, S. Wuestner, J. M. Hamm, K. L. Tsakmakidis, and O. Hess, “Coherent Amplification and Noise in Gain-Enhanced Nanoplasmonic Metamaterials: A Maxwell-Bloch Langevin Approach,” *ACS Nano*, vol. 6, pp. 2420–2431, mar 2012.
- [92] J. A. Roden and S. D. Gedney, “Convolution PML (CPML): An efficient FDTD implementation of the CFS-PML for arbitrary media,” *Microwave and Optical Technology Letters*, vol. 27, pp. 334–339, dec 2000.
- [93] S. Wuestner, T. W. Pickering, J. M. Hamm, A. F. Page, A. Pusch, and O. Hess, “Ultrafast dynamics of nanoplasmonic stopped-light lasing,” *Faraday Discussions*, vol. 178, pp. 307–324, 2015.
- [94] I. Carusotto and C. Ciuti, “Quantum fluids of light,” *Reviews of Modern Physics*, vol. 85, pp. 299–366, feb 2013.
- [95] M. J. Allen, V. C. Tung, and R. B. Kaner, “Honeycomb Carbon: A Review of Graphene,” *Chemical Reviews*, vol. 110, pp. 132–145, jan 2010.
- [96] F. Schwierz, “Graphene transistors,” *Nat Nano*, vol. 5, pp. 487–496, jul 2010.
- [97] V. C. Sanchez, A. Jachak, R. H. Hurt, and A. B. Kane, “Biological Interactions of Graphene-Family Nanomaterials: An Interdisciplinary Review,” *Chemical Research in Toxicology*, vol. 25, pp. 15–34, jan 2012.
- [98] D. R. Cooper, B. D’Anjou, N. Ghattamaneni, B. Harack, M. Hilke, A. Horth, N. Majlis, M. Massicotte, L. Vandsburger, E. Whiteway, and V. Yu, “Experimental Review of Graphene,” 2012.
- [99] M. Pumera, “Electrochemistry of graphene, graphene oxide and other graphenoids: Review,” *Electrochemistry Communications*, vol. 36, pp. 14–18, nov 2013.

References

- [100] A. H. Castro Neto, F. Guinea, N. M. R. Peres, K. S. Novoselov, and A. K. Geim, “The electronic properties of graphene,” *Reviews of Modern Physics*, vol. 81, pp. 109–162, jan 2009.
- [101] K. S. Novoselov, A. K. Geim, S. V. Morozov, D. Jiang, M. I. Katsnelson, I. V. Grigorieva, S. V. Dubonos, and A. A. Firsov, “Two-dimensional gas of massless Dirac fermions in graphene.,” *Nature*, vol. 438, pp. 197–200, nov 2005.
- [102] P. Avouris, Z. Chen, and V. Perebeinos, “Carbon-based electronics,” *Nat Nano*, vol. 2, pp. 605–615, oct 2007.
- [103] F. Bonaccorso, Z. Sun, T. Hasan, and A. C. Ferrari, “Graphene photonics and optoelectronics,” *Nature Photonics*, vol. 4, pp. 611–622, aug 2010.
- [104] S. Das Sarma, S. Adam, E. H. Hwang, and E. Rossi, “Electronic transport in two-dimensional graphene,” *Reviews of Modern Physics*, vol. 83, pp. 407–470, may 2011.
- [105] L. A. Falkovsky and S. S. Pershoguba, “Optical far-infrared properties of a graphene monolayer and multilayer,” *Phys. Rev. B*, vol. 76, p. 153410, oct 2007.
- [106] A. B. Kuzmenko, E. van Heumen, F. Carbone, and D. van der Marel, “Universal Optical Conductance of Graphite,” *Phys. Rev. Lett.*, vol. 100, p. 117401, mar 2008.
- [107] R. R. Nair, P. Blake, A. N. Grigorenko, K. S. Novoselov, T. J. Booth, T. Stauber, N. M. R. Peres, and A. K. Geim, “Fine Structure Constant Defines Visual Transparency of Graphene,” *Science*, vol. 320, p. 1308, jun 2008.
- [108] K. F. Mak, M. Y. Sfeir, Y. Wu, C. H. Lui, J. A. Misewich, and T. F. Heinz, “Measurement of the Optical Conductivity of Graphene,” *Physical Review Letters*, vol. 101, p. 196405, nov 2008.
- [109] S. A. Mikhailov, “Non-linear electromagnetic response of graphene,” *Europhysics Letters (EPL)*, vol. 79, p. 27002, jul 2007.

References

- [110] E. Hendry, P. J. Hale, J. Moger, A. K. Savchenko, and S. A. Mikhailov, “Coherent Nonlinear Optical Response of Graphene,” *Physical Review Letters*, vol. 105, p. 097401, aug 2010.
- [111] K. L. Ishikawa, “Nonlinear optical response of graphene in time domain,” *Physical Review B*, vol. 82, p. 201402, nov 2010.
- [112] M. L. Nesterov, J. Bravo-Abad, A. Y. Nikitin, F. J. García-Vidal, and L. Martín-Moreno, “Graphene supports the propagation of subwavelength optical solitons,” *Laser & Photonics Reviews*, vol. 7, no. 2, pp. L7–L11, 2013.
- [113] B. J. Kim, H. Jang, S.-K. Lee, B. H. Hong, J.-H. Ahn, and J. H. Cho, “High-performance flexible graphene field effect transistors with ion gel gate dielectrics.,” *Nano Letters*, vol. 10, pp. 3464–6, sep 2010.
- [114] H. Liu, Y. Liu, and D. Zhu, “Chemical doping of graphene,” *Journal of Materials Chemistry*, vol. 21, no. 10, p. 3335, 2011.
- [115] L. Ju, B. Geng, J. Horng, C. Girit, M. Martin, Z. Hao, H. A. Bechtel, X. Liang, A. Zettl, Y. R. Shen, and F. Wang, “Graphene plasmonics for tunable terahertz metamaterials.,” *Nature Nanotechnology*, vol. 6, pp. 630–4, oct 2011.
- [116] Z. Fei, A. S. Rodin, G. O. Andreev, W. Bao, A. S. McLeod, M. Wagner, L. M. Zhang, Z. Zhao, M. Thiemens, G. Dominguez, M. M. Fogler, A. H. Castro Neto, C. N. Lau, F. Keilmann, and D. N. Basov, “Gate-tuning of graphene plasmons revealed by infrared nano-imaging.,” *Nature*, vol. 487, pp. 82–5, jul 2012.
- [117] T. Mueller, F. Xia, and P. Avouris, “Graphene photodetectors for high-speed optical communications,” *Nature Photonics*, vol. 4, no. March, pp. 297–301, 2010.
- [118] F. Withers, T. H. Bointon, M. F. Craciun, and S. Russo, “All-Graphene Photodetectors,” *ACS Nano*, vol. 7, no. 6, pp. 5052–5057, 2013.

References

- [119] C.-H. Liu, Y.-C. Chang, T. B. Norris, and Z. Zhong, “Graphene photodetectors with ultra-broadband and high responsivity at room temperature.,” *Nature Nanotechnology*, vol. 9, pp. 273–8, apr 2014.
- [120] M. Liu, X. Yin, E. Ulin-Avila, B. Geng, T. Zentgraf, L. Ju, F. Wang, and X. Zhang, “A graphene-based broadband optical modulator.,” *Nature*, vol. 474, pp. 64–7, jun 2011.
- [121] Q. Bao, H. Zhang, Y. Wang, Z. Ni, Y. Yan, Z. X. Shen, K. P. Loh, and D. Y. Tang, “Atomic-Layer Graphene as a Saturable Absorber for Ultrafast Pulsed Lasers,” *Advanced Functional Materials*, vol. 19, pp. 3077–3083, oct 2009.
- [122] S. H. Lee, M. Choi, T.-T. Kim, S. Lee, M. Liu, X. Yin, H. K. Choi, S. S. Lee, C.-G. Choi, S.-Y. Choi, X. Zhang, and B. Min, “Switching terahertz waves with gate-controlled active graphene metamaterials.,” *Nature Materials*, vol. 11, pp. 936–41, nov 2012.
- [123] A. Vakil and N. Engheta, “Fourier optics on graphene,” *Physical Review B*, vol. 85, p. 075434, feb 2012.
- [124] J. M. Hamm and O. Hess, “Two Two-Dimensional Materials Are Better than One,” *Science*, vol. 340, pp. 1298–1299, jun 2013.
- [125] F. Schedin, E. Lidorikis, and A. Lombardo, “Surface-enhanced Raman spectroscopy of graphene,” *ACS Nano*, vol. 4, no. 10, pp. 5617–5626, 2010.
- [126] S. K. Lee, H. Y. Jang, S. Jang, E. Choi, and B. H. Hong, “All graphene-based thin film transistors on flexible plastic substrates,” *Nano Letters*, vol. 12, pp. 3472–6, 2012.
- [127] S. Y. Shin, N. D. Kim, J. G. Kim, K. S. Kim, D. Y. Noh, K. S. Kim, and J. W. Chung, “Control of the π plasmon in a single layer graphene by charge doping,” *Applied Physics Letters*, vol. 99, no. 8, p. 082110, 2011.
- [128] J. Chen, M. Badioli, P. Alonso-González, S. Thongrattanasiri, F. Huth, J. Osmond, M. Spasenović, A. Centeno, A. Pesquera, P. Godignon, A. Z. Elorza, N. Camara, F. J.

References

- García de Abajo, R. Hillenbrand, and F. H. L. Koppens, “Optical nano-imaging of gate-tunable graphene plasmons,” *Nature*, vol. 487, pp. 77–81, jul 2012.
- [129] A. N. Grigorenko, M. Polini, and K. S. Novoselov, “Graphene plasmonics,” *Nat Photon*, vol. 6, pp. 749–758, nov 2012.
- [130] Q. Bao and K. P. Loh, “Graphene photonics, plasmonics, and broadband optoelectronic devices,” *ACS Nano*, vol. 6, pp. 3677–94, may 2012.
- [131] T. Low and P. Avouris, “Graphene Plasmonics for Terahertz to Mid-Infrared Applications,” *ACS Nano*, vol. 8, no. 2, pp. 1086–1101, 2014.
- [132] T. Stauber, “Plasmonics in Dirac systems: from graphene to topological insulators,” *J. Phys: Condens. Matter*, vol. 26, p. 123201, mar 2014.
- [133] F. J. García de Abajo, “Graphene plasmonics: Challenges and opportunities,” *ACS Photonics*, vol. 24, 2014.
- [134] A. Agarwal and G. Vignale, “Plasmons in spin-polarized graphene: A way to measure spin polarization,” *Physical Review B*, vol. 91, p. 245407, jun 2015.
- [135] F. H. L. Koppens, D. E. Chang, and F. J. García de Abajo, “Graphene plasmonics: a platform for strong light-matter interactions,” *Nano Letters*, vol. 11, pp. 3370–7, aug 2011.
- [136] B. Wunsch, T. Stauber, F. Sols, and F. Guinea, “Dynamical polarization of graphene at finite doping,” *New Journal of Physics*, vol. 8, pp. 318–318, dec 2006.
- [137] E. H. Hwang and S. Das Sarma, “Dielectric function, screening, and plasmons in two-dimensional graphene,” *Physical Review B*, vol. 4111, p. 205418, may 2007.
- [138] P. Tassin, T. Koschny, M. Kafesaki, and C. M. Soukoulis, “A comparison of graphene, superconductors and metals as conductors for metamaterials and plasmonics,” *Nature Photonics*, vol. 6, pp. 259–264, 2012.

References

- [139] H. Yan, T. Low, W. Zhu, Y. Wu, M. Freitag, X. Li, P. Avouris, and F. Xia, “Damping pathways of mid-infrared plasmons in graphene nanostructures,” *Nature Photonics*, vol. 7, no. May, p. 394, 2013.
- [140] V. Ryzhii, M. Ryzhii, and T. Otsuji, “Negative dynamic conductivity of graphene with optical pumping,” *Journal of Applied Physics*, vol. 101, no. 8, p. 083114, 2007.
- [141] T. Li, L. Luo, M. Hupalo, J. Zhang, M. C. Tringides, J. Schmalian, and J. Wang, “Femtosecond Population Inversion and Stimulated Emission of Dense Dirac Fermions in Graphene,” *Physical Review Letters*, vol. 108, p. 167401, apr 2012.
- [142] T. Winzer, E. Malić, and A. Knorr, “Microscopic mechanism for transient population inversion and optical gain in graphene,” *Physical Review B*, vol. 87, p. 165413, apr 2013.
- [143] F. Rana, “Graphene Terahertz Plasmon Oscillators,” *IEEE Transactions on Nanotechnology*, vol. 7, no. 1, pp. 91–99, 2008.
- [144] F. Rana, J. H. Strait, H. Wang, and C. Manolatou, “Ultrafast carrier recombination and generation rates for plasmon emission and absorption in graphene,” *Physical Review B*, vol. 84, p. 045437, jul 2011.
- [145] A. A. Dubinov, V. Y. Aleshkin, V. Mitin, T. Otsuji, and V. Ryzhii, “Terahertz surface plasmons in optically pumped graphene structures,” *Journal of Physics: Condensed Matter*, vol. 23, no. 14, p. 145302, 2011.
- [146] V. V. Popov, O. V. Polischuk, A. R. Davoyan, V. Ryzhii, T. Otsuji, and M. S. Shur, “Plasmonic terahertz lasing in an array of graphene nanocavities,” *Physical Review B*, vol. 86, p. 195437, nov 2012.
- [147] M. Mecklenburg, J. Woo, and B. C. Regan, “Tree-level electron-photon interactions in graphene,” *Physical Review B*, vol. 81, p. 245401, jun 2010.
- [148] A. Y. Nikitin, F. J. García-Vidal, and L. Martín-Moreno, “Analytical expressions for the

References

- Electromagnetic Dyadic Green's Function in Graphene and thin layers," *IEEE J. Quantum Elect.*, vol. 19, no. 3, 2013.
- [149] A. Bostwick, T. Ohta, T. Seyller, K. Horn, and E. Rotenberg, "Quasiparticle dynamics in graphene," *Nature Physics*, vol. 3, pp. 36–40, dec 2007.
- [150] P. A. George, J. H. Strait, J. M. Dawlaty, S. Shivaraman, M. Chandrashekhar, F. Rana, and M. G. Spencer, "Ultrafast Optical-Pump Terahertz-Probe Spectroscopy of the Carrier Relaxation and Recombination Dynamics in Epitaxial Graphene," *Nano Letters*, vol. 8, no. 12, pp. 4248–4251, 2008.
- [151] A. Girdhar and J. P. Leburton, "Soft carrier multiplication by hot electrons in graphene," *Applied Physics Letters*, vol. 99, no. 4, p. 043107, 2011.
- [152] E. Malić, T. Winzer, E. Bobkin, and A. Knorr, "Microscopic theory of absorption and ultrafast many-particle kinetics in graphene," *Physical Review B*, vol. 84, p. 205406, nov 2011.
- [153] R. Kim, V. Perebeinos, and P. Avouris, "Relaxation of optically excited carriers in graphene," *Physical Review B*, vol. 84, p. 075449, aug 2011.
- [154] T. Winzer and E. Malić, "Impact of Auger processes on carrier dynamics in graphene," *Physical Review B*, vol. 85, p. 241404, jun 2012.
- [155] B. Y. Sun, Y. Zhou, and M. W. Wu, "Dynamics of photoexcited carriers in graphene," *Physical Review B*, vol. 85, p. 125413, mar 2012.
- [156] A. Tomadin, D. Brida, G. Cerullo, A. C. Ferrari, and M. Polini, "Nonequilibrium dynamics of photoexcited electrons in graphene: Collinear scattering, Auger processes, and the impact of screening," *Physical Review B*, vol. 88, p. 035430, jul 2013.
- [157] B. Y. Sun and M. W. Wu, "Microscopic theory of ultrafast dynamics of carriers photoexcited by THz and near-infrared linearly polarized laser pulses in graphene," *New Journal of Physics*, vol. 15, p. 083038, aug 2013.

References

- [158] D. Brida, A. Tomadin, C. Manzoni, Y. J. Kim, A. Lombardo, S. Milana, R. R. Nair, K. S. Novoselov, A. C. Ferrari, G. Cerullo, and M. Polini, “Ultrafast collinear scattering and carrier multiplication in graphene.” *Nature Communications*, vol. 4, p. 1987, jan 2013.
- [159] M. Breusing, S. Kuehn, T. Winzer, E. Malić, F. Milde, N. Severin, J. P. Rabe, C. Ropers, A. Knorr, and T. Elsaesser, “Ultrafast nonequilibrium carrier dynamics in a single graphene layer,” *Physical Review B*, vol. 83, p. 153410, apr 2011.
- [160] K. J. Tielrooij, J. C. W. Song, S. A. Jensen, A. Centeno, A. Pesquera, A. Zurutuza Elorza, M. Bonn, L. S. Levitov, and F. H. L. Koppens, “Photoexcitation cascade and multiple hot-carrier generation in graphene,” *Nat Phys*, vol. 9, pp. 248–252, apr 2013.
- [161] I. Gierz, J. C. Petersen, M. Mitrano, C. Cacho, I. C. E. Turcu, E. Springate, A. Stöhr, A. Köhler, U. Starke, and A. Cavalleri, “Snapshots of non-equilibrium Dirac carrier distributions in graphene.” *Nature Materials*, vol. 12, pp. 1119–24, dec 2013.
- [162] J. C. Johannsen, S. Ulstrup, F. Cilento, A. Crepaldi, M. Zacchigna, C. Cacho, I. C. E. Turcu, E. Springate, F. Fromm, C. Raidel, T. Seyller, F. Parmigiani, M. Grioni, and P. Hofmann, “Direct View of Hot Carrier Dynamics in Graphene,” *Physical Review Letters*, vol. 111, p. 027403, jul 2013.
- [163] I. Gierz, S. Link, U. Starke, and A. Cavalleri, “Faraday Discussions Emerging Photon Technologies for Chemical Dynamics,” *Faraday Discussions*, vol. 171, pp. 311–321, 2014.
- [164] I. Gierz, F. Calegari, S. Aeschlimann, M. Chávez Cervantes, C. Cacho, R. T. Chapman, E. Springate, S. Link, U. Starke, C. R. Ast, and A. Cavalleri, “Tracking Primary Thermalization Events in Graphene with Photoemission at Extreme Time Scales,” *Physical Review Letters*, vol. 115, p. 86803, aug 2015.
- [165] J. M. Dawlaty, S. Shivaraman, M. Chandrashekhar, F. Rana, and M. G. Spencer, “Measurement of ultrafast carrier dynamics in epitaxial graphene,” *Applied Physics Letters*, vol. 92, no. 4, p. 042116, 2008.

References

- [166] H. Choi, F. Borondics, D. A. Siegel, S. Y. Zhou, M. C. Martin, A. Lanzara, and R. A. Kaindl, “Broadband electromagnetic response and ultrafast dynamics of few-layer epitaxial graphene,” *Applied Physics Letters*, vol. 94, no. 17, p. 172102, 2009.
- [167] M. Breusing, C. Ropers, and T. Elsaesser, “Ultrafast Carrier Dynamics in Graphite,” *Physical Review Letters*, vol. 102, p. 086809, feb 2009.
- [168] L. M. Malard, K. Fai Mak, A. H. Castro Neto, N. M. R. Peres, and T. F. Heinz, “Observation of intra- and inter-band transitions in the transient optical response of graphene,” *New Journal of Physics*, vol. 15, p. 015009, jan 2013.
- [169] S. A. Jensen, Z. Mics, I. Ivanov, H. S. Varol, D. Turchinovich, F. H. L. Koppens, M. Bonn, and K. J. Tielrooij, “Competing Ultrafast Energy Relaxation Pathways in Photoexcited Graphene,” *Nano Letters*, vol. 14, no. 10, pp. 5839–5845, 2014.
- [170] O. Vafeck, “Thermoplasma Polariton within Scaling Theory of Single-Layer Graphene,” *Physical Review Letters*, vol. 97, p. 266406, dec 2006.
- [171] S. A. Mikhailov and K. Ziegler, “New Electromagnetic Mode in Graphene,” *Physical Review Letters*, vol. 99, p. 016803, jul 2007.
- [172] X.-F. Wang and T. Chakraborty, “Collective excitations of Dirac electrons in a graphene layer with spin-orbit interactions,” *Physical Review B*, vol. 75, p. 033408, jan 2007.
- [173] P. K. Pyatkovskiy, “Dynamical polarization, screening, and plasmons in gapped graphene,” *Journal of Physics: Condensed Matter*, vol. 025506, 2009.
- [174] M. R. Ramezanali, M. M. Vazifeh, R. Asgari, M. Polini, and A. H. MacDonald, “Finite-temperature screening and the specific heat of doped graphene sheets,” *Journal of Physics A: Mathematical and Theoretical*, vol. 42, p. 214015, may 2009.
- [175] M. Jablan, H. Buljan, and M. Soljačić, “Plasmonics in graphene at infrared frequencies,” *Physical Review B*, vol. 80, p. 245435, dec 2009.

References

- [176] A. Scholz and J. Schliemann, “Dynamical current-current susceptibility of gapped graphene,” *Physical Review B*, vol. 83, p. 235409, jun 2011.
- [177] A. Scholz, T. Stauber, and J. Schliemann, “Dielectric function, screening, and plasmons of graphene in the presence of spin-orbit interactions,” *Physical Review B*, vol. 86, p. 195424, nov 2012.
- [178] A. Gutiérrez-Rubio, T. Stauber, and F. Guinea, “Transverse current response of graphene at finite temperature: plasmons and absorption,” *Journal of Optics*, vol. 15, p. 114005, nov 2013.
- [179] A. Principi, M. Polini, and G. Vignale, “Linear response of doped graphene sheets to vector potentials,” *Physical Review B*, vol. 80, p. 075418, aug 2009.
- [180] T. Stauber and G. Gómez-Santos, “Dynamical current-current correlation of the hexagonal lattice and graphene,” *Physical Review B*, vol. 82, p. 155412, oct 2010.
- [181] F. M. D. Pellegrino, G. G. N. Angilella, and R. Pucci, “Linear response correlation functions in strained graphene,” *Physical Review B*, vol. 84, p. 195407, 2011.
- [182] M. Polini, R. Asgari, G. Borghi, Y. Barlas, T. Pereg-Barnea, and A. H. MacDonald, “Plasmons and the spectral function of graphene,” *Physical Review B*, vol. 77, p. 081411, feb 2008.
- [183] A. Bostwick, F. Speck, T. Seyller, K. Horn, M. Polini, R. Asgari, A. H. MacDonald, and E. Rotenberg, “Observation of plasmarons in quasi-freestanding doped graphene,” *Science (New York, N.Y.)*, vol. 328, pp. 999–1002, may 2010.
- [184] F. Stern, “Polarizability of a two-dimensional electron gas,” *Physical Review Letters*, vol. 18, no. 14, pp. 546–548, 1967.
- [185] G. Giuliani and G. Vignale, *Quantum Theory of the Electron Liquid*. Cambridge University Press, 2005.

References

- [186] M. Hasegawa and M. Watabe, “Theory of plasmon damping in metals. I. General formulation and application to an electron gas,” *Journal of the Physical Society of Japan*, vol. 77, p. 1393, 1969.
- [187] H. Bruus and K. Flensberg, *Many-Body Quantum Theory in Condensed Matter Physics: An Introduction*. Oxford Graduate Texts, OUP Oxford, 2004.
- [188] D. S. L. Abergel, V. Apalkov, J. Berashevich, K. Ziegler, and T. Chakraborty, “Properties of graphene: a theoretical perspective,” *Advances in Physics*, vol. 59, pp. 261–482, jul 2010.
- [189] J. Hofmann, E. Barnes, and S. Das Sarma, “Why Does Graphene Behave as a Weakly Interacting System?”, *Physical Review Letters*, vol. 113, p. 105502, sep 2014.
- [190] V. N. Kotov, B. Uchoa, V. M. Pereira, F. Guinea, and a. H. Castro Neto, “Electron-Electron Interactions in Graphene: Current Status and Perspectives,” *Reviews of Modern Physics*, vol. 84, pp. 1067–1125, jul 2012.
- [191] A. L. Fetter and J. D. Walecka, *Quantum Theory of Many-Particle Systems*. Dover Books on Physics, Dover Publications, 2012.
- [192] A. Principi, G. Vignale, M. Carrega, and M. Polini, “Intrinsic lifetime of Dirac plasmons in graphene,” *Physical Review B*, vol. 88, p. 195405, nov 2013.
- [193] A. F. Page, F. Ballout, O. Hess, and J. M. Hamm, “Nonequilibrium plasmons with gain in graphene,” *Physical Review B*, vol. 91, p. 75404, feb 2015.
- [194] A. Hill, S. A. Mikhailov, and K. Ziegler, “Dielectric function and plasmons in graphene,” *EPL (Europhysics Letters)*, vol. 87, p. 27005, jul 2009.
- [195] S. Butscher, F. Milde, M. Hirtschulz, E. Malić, and A. Knorr, “Hot electron relaxation and phonon dynamics in graphene,” *Applied Physics Letters*, vol. 91, no. 20, p. 203103, 2007.

References

- [196] F. Rana, P. A. George, J. H. Strait, J. M. Dawlaty, S. Shivaraman, M. Chandrashekhar, and M. G. Spencer, “Carrier recombination and generation rates for intravalley and intervalley phonon scattering in graphene,” *Physical Review B*, vol. 79, p. 115447, mar 2009.
- [197] H. Wang, J. H. Strait, P. A. George, S. Shivaraman, V. B. Shields, M. Chandrashekhar, J. Hwang, F. Rana, M. G. Spencer, C. S. Ruiz-Vargas, and J. Park, “Ultrafast relaxation dynamics of hot optical phonons in graphene,” *Applied Physics Letters*, vol. 96, no. 8, p. 081917, 2010.
- [198] J. González, F. Guinea, and M. A. H. Vozmediano, “Non-Fermi liquid behavior of electrons in the half-filled honeycomb lattice (A renormalization group approach),” *Nuclear Physics B*, vol. 424, no. 3, pp. 595–618, 1994.
- [199] C. Jang, S. Adam, J.-H. Chen, E. D. Williams, S. Das Sarma, and M. S. Fuhrer, “Tuning the Effective Fine Structure Constant in Graphene: Opposing Effects of Dielectric Screening on Short- and Long-Range Potential Scattering,” *Physical Review Letters*, vol. 101, p. 146805, oct 2008.
- [200] S. Winnerl, M. Orlita, P. Plochocka, P. Kossacki, M. Potemski, T. Winzer, E. Malić, A. Knorr, M. Sprinkle, C. Berger, W. A. de Heer, H. Schneider, and M. Helm, “Carrier Relaxation in Epitaxial Graphene Photoexcited Near the Dirac Point,” *Physical Review Letters*, vol. 107, p. 237401, nov 2011.
- [201] M. P. Kesler and E. P. Ippen, “Subpicosecond gain dynamics in GaAlAs laser diodes,” *Applied Physics Letters*, vol. 51, no. 22, p. 1765, 1987.
- [202] H. Haug and S. W. Koch, “Semiconductor laser theory with many-body effects,” *Physical Review A*, vol. 39, no. 4, pp. 1887–1998, 1989.
- [203] S. J. Blundell and K. M. Blundell, *Concepts in Thermal Physics*. OUP Oxford, 2010.
- [204] J. M. Dawlaty, S. Shivaraman, J. H. Strait, P. A. George, M. Chandrashekhar, F. Rana, M. G. Spencer, D. Veksler, and Y. Chen, “Measurement of the optical absorption

References

- spectra of epitaxial graphene from terahertz to visible," *Applied Physics Letters*, vol. 93, no. 13, p. 131905, 2008.
- [205] B. Scharf, V. Perebeinos, J. Fabian, and P. Avouris, "Effects of optical and surface polar phonons on the optical conductivity of doped graphene," *Physical Review B*, vol. 87, p. 035414, jan 2013.
- [206] N. D. Mermin, "Lindhard dielectric function in the relaxation-time approximation," *Physical Review B*, vol. 1, no. 5, p. 2362, 1970.
- [207] J. C. W. Song and L. S. Levitov, "Energy flows in graphene: hot carrier dynamics and cooling," *Journal of Physics: Condensed Matter*, vol. 27, no. 16, p. 164201, 2015.
- [208] F. Rana, "Electron-hole generation and recombination rates for Coulomb scattering in graphene," *Physical Review B*, vol. 76, p. 155431, oct 2007.
- [209] J. M. Hamm, A. F. Page, J. Bravo-Abad, F. J. Garcia-Vidal, and O. Hess, "Nonequilibrium plasmon emission drives ultrafast carrier relaxation dynamics in photoexcited graphene," *Physical Review B*, vol. 93, no. 4, p. 41408(R), 2016.